INVESTIGATIONS INTO UNCONVENTIONAL SUPERCONDUCTORS THROUGH THE USE OF SMALL ANGLE NEUTRON SCATTERING

ALISTAIR CAMERON

A thesis submitted to
The University of Birmingham
for the degree of
DOCTOR OF PHILOSOPHY

School of Physics and Astronomy
University of Birmingham
September 2013

Abstract

Here we present an investigation into the vortex lattice of KFe_2As_2 (KFA), $BaFe_2(As_{1-x}P_x)_2$ (BFAP) an $YBa_2Cu_3O_7$ (YBCO) by small angle neutron scattering (SANS). KFA and BFAP are members of the pnictide group of superconductors which, since the discovery of an iron-based superconductor in 2006 (Kamihara et al., 2006), have become perhaps the most investigated class of superconductor in recent years. As a relatively new class of superconductor there is a great deal of interest in clarifying the fundamental mechanism in these materials which leads to superconductivity. Here, through the study of the magnetic vortex lattice, we search for information about the pairing state of two members of the 122 group of the pnictide superconductors, finding strong evidence for a nodal gap structure in both materials. In contrast, YBCO is a member of the cuprate family of superconductors, discovered in 1987 (Wu et al., 1987) shortly after the discovery of high temperature superconductivity a year earlier (Bednorz and Muller, 1986). The cuprate superconductors, so named for the copper-oxide layers which form their common building block, have been under continuous investigation since their discovery, and here we present the first microscopic study of vortex matter in fields of up to 16.7 T. We observe the continuation of a field dependent vortex lattice structure which was observed in measurements at lower fields (White et al., 2009), and strong indications of a static Debye-Waller effect arising from disorder in the vortex lattice. At high field, vortex lattice melting is observed at a temperature and field which corresponds to a 1st order melting transition observed in heat capacity measurements (Roulin et al., 1998), and above the melting transition no SANS signal from the vortex liquid is observed on the time-scale of our measurements.

For Hilary and Andrew Cameron

Acknowledgements

Firstly I would like to thank my supervisor, Ted Forgan, for giving me the opportunity to undertake a PhD in the Condensed Matter group. Ted is a exceptional physicist to work with, possessing a deep understanding of the subject at hand and a far reaching interest and enjoyment of physics. I have thoroughly enjoyed my time as Ted's student, and am exceptionally grateful for all the opportunities given to me to engage with a worldwide community of people in researching a most fascinating subject.

I would like to thank the Condensed Matter Group at the University of Birmingham for the enjoyable time I have had during my PhD. Particularly I would like to thank Elizabeth Blackburn, with whom I have enjoyed many an experiment and who is always on hand to give insightful advise. A special thanks goes to Alex Holmes for explaining, over the phone, what to do with a quenched magnet that has sprung a leak in the middle of the night. From the devices subgroup, I acknowledge Chris Muirhead and Mark Colclough who also played memorable roles in my undergraduate education here at Birmingham. From my office, I thank Josh, George, Bindu, Louis and Lingjia for the interesting conversations, helpful advice and an enjoyable time as a PhD student. A particular thanks goes out to John White, for showing me the ropes when I got here and teaching me, among other things, the basics of neutron experiments.

I would particularly like to thank Hazuki Kawano-Furukawa, who has been a fantastic collaborator throughout our investigation into the pnictide superconductors. Aside from bringing a multitude of samples with some exceptionally skilled alignment of crystal mosaics, Hazuki has dedicated a great deal of time and effort into helping us all understand what is going on in a complicated set of superconductors. I look forward to future collaborations.

I am also grateful for the many interactions I have had with physicists from around the world during my time at the various neutron scattering institutions where the measurements in this thesis. From the ILL I particularly acknowledge Charles Dewhurst and Bob Cubitt, who have always provided excellent help and advice during their time as our

local contacts, even at untimely hours of the day, night and weekends. From PSI I thank Jorge Gavilano for his fantastic assistance during our time on SANS-I.

I must also thank my super friends and brilliant housemates, whose close friendship has given me a great deal of support over the years and led to more fun and exciting adventures than I dare to mention. They deserve a great deal of commendation in displaying patience during the numerous times when I have brought the conversation into a realm of physics somewhat removed from everyday life. A special mention goes out to the J-Tones, with whom I have enjoyed many hours pretending to be a Saxophonist. To them, I promise that one day I *will* remember what key the next piece is in.

I save the final thanks for my parents, for all the love and support they have given me. If I had to put down a moment where physics became something I found interesting it would have to be sometime around the age of seven, when my father sat me down and explained a very basic model of the atom. Whilst the idea of wavefunctions and condensates were still a far distant concept at that point, something about it grabbed my attention and has yet to let go.

CONTENTS

LIST OF FIGURES

LIST OF TABLES

CHAPTER 1

THEORY

In April of 1911 H. Kamerlingh Onnes (Onnes, 1911) discovered the disappearance of electrical resistance in mercury below a critical temperature, T_c of approximately 4 K. This phenomenon was soon after discovered to exist in a variety of elements, and later a large variety of compounds. It was given the name superconductivity. The two main distinguishing properties of the superconducting phase are seemingly perfect conductivity and, as later discovered by Meissner and Ochsenfeld (Meissner and Ochsenfeld, 1933), perfect diamagnetism. Here, all magnetic field is excluded from the bulk of the superconductor, a phenomenon known as the Meissner effect. Superconductors fall into two main categories, named type-I and type-II, the distinction between them being illustrated by their response to an externally applied magnetic field. Type-I superconductors exhibit the Meissner state until a critical applied field, $\mathbf{H}_c$, is reached and superconductivity is destroyed. Magnetic field is prevented from entering the bulk of the superconductor by screening currents flowing in the surface of the material. The depth to which an applied field penetrates and currents flow is typically, in the case of samples in this thesis, far smaller than the size of the superconductor. Type-II superconductors display a similar behaviour until the applied field surpasses what is known as the lower critical field, $\mathbf{H}_{c1}$, and it becomes energetically favourable for them to allow field to pass in discrete units of the flux quantum, $\frac{h}{2e}$. These are known as flux lines. With increasing field, more of the flux lines enter superconductor until the normal cores begin to overlap and superconductivity is again destroyed, at a point known as the upper critical field, $\mathbf{H}_{c2}$.

1.1 Thermodynamic description of Superconductivity

An important property of the Meissner state, which distinguishes it from perfect conductivity, is that its final state is independent of the path taken to get there. The contrast with a perfect conductor can be seen from the Maxwell equations, where for systems with zero resistivity $d\mathbf{B}/dt = 0$, indicating that a perfect conductor merely preserves the existing field whereas the Meissner state excludes the applied field from the bulk of a superconductor regardless of whether the field existed before or after the material entered the superconducting phase. This shows that the Meissner state is a thermodynamic state, and thus the thermodynamics of the system is a good place to start in any effort to describe superconductivity. Following the treatment of Hook and Hall (Hook and Hall, 1991), the field $\mathbf{B}$ at which the superconducting and normal states are in equilibrium, and thus the transition point between the states, is given by the equality of their Gibbs free energies. Taking the magnetic work term to be $-M \cdot \mathrm{d}\mathbf{B}$ and assuming constant pressure and volume at the transition, the Gibbs free energy per unit volume is given by

$$G = E - TS \tag{1.1}$$

where E and S are the internal energy and entropy per unit volume respectively. To see that the Gibbs free energy is minimised at constant temperature and applied field, we use $\mathrm{d}E = T\mathrm{d}S - M \cdot \mathrm{d}\mathbf{B}$ to calculate

$$dG = \mathrm{d}E - T\mathrm{d}S - S\mathrm{d}T = T\mathrm{d}S - M \cdot \mathrm{d}\mathbf{B} - T\mathrm{d}S - S\mathrm{d}T = -M \cdot \mathrm{d}\mathbf{B} - SdT. \tag{1.2}$$

Considering a long thin cylinder of superconductor parallel to the applied field, the above can be integrated to deduce the resultant free energy change per unit volume from the application of the field.

$$G_s(\mathbf{B},T) = G_s(0,T) - \int_0^{\mathbf{B}} M \cdot \mathrm{d}\mathbf{B} = G_s(0,T) + \frac{\mathbf{B}^2}{2\mu_0} \tag{1.3}$$

Where the property of the Meissner state that $M = -H$ has been used. Here, the $B^2/2\mu_0$ term represents the energy associated with excluding the magnetic field from the superconducting bulk. If we ignore the weak magnetisation of the normal state such that the Gibbs free energy of the normal state is field independent, the equality of the free energies at the superconducting to normal transition gives

$$G_N(0,T) - G_S(0,T) = \frac{\mathbf{B}_c^2}{2\mu_0} \tag{1.4}$$

where $\mathbf{B}_c$ is the thermodynamic critical field of the superconductor. The positive value of this explains why the superconducting state is more stable than its normal counterpart in no applied field, and it is known as the condensation energy of the superconducting state. The thermodynamic critical field of a superconductor is temperature dependent, which is illustrated in fig. 1.1. Taken from work by Helfand and Werthamer (Werthamer et al., 1966), the authors have calculated the upper critical field as a function of temperature and purity, which refers to the number of defects within the superconductor. Their work, which is beyond the scope of this thesis, allows for the calculation of the critical field at zero temperature from the slope of the critical field at T_c, although for calculations of work presented later in this thesis we used the simpler Ginzburg-Landau expression given in equation 1.56 in section 1.8.

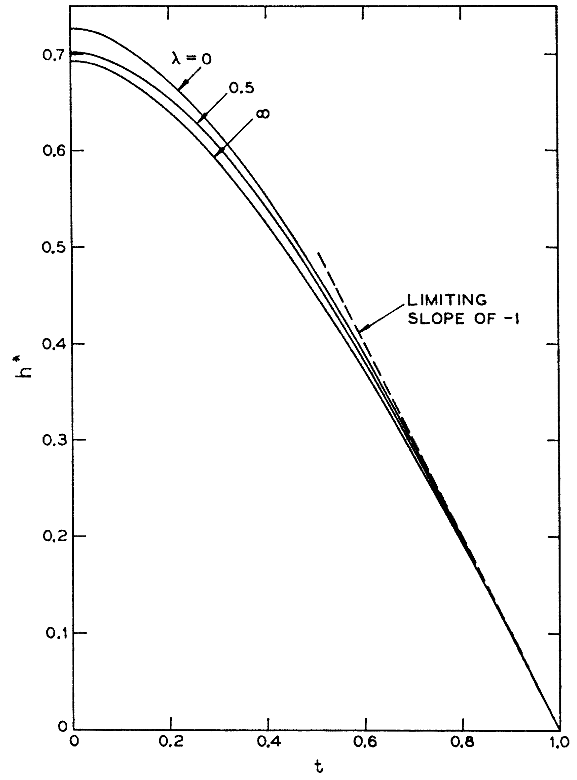

Figure 1.1: Figure illustrating the critical field, reduced to have a slope of -1 at $t = 1$, plotted as a function of reduced temperature and purity, where $\lambda = 0$ is clean and $\lambda = \infty$ is dirty. Figure taken from Helfand and Werthamer (Werthamer et al., 1966).

On a broad scale, superconductors fall into two main categories - type-I and type-II, the difference between them being characterised by their response to an externally applied field. Type-I superconductors exhibit the Meissner effect throughout the superconducting phase, where the applied field is excluded from the bulk of the superconductor except for the region close to the surface of the order of the London penetration depth and the magnetisation is therefore $\mathbf{M} = -\mathbf{H}$. Increasing the applied field past the critical field $\mathbf{H}_c$, and the system undergoes a first order transition to the normal state. Type-II superconductors, however, have two different critical fields - $\mathbf{H}_{c1}$ and $\mathbf{H}_{c2}$, where the critical field in figure 1.1 is the upper critical field, $\mathbf{H}_{c2}$ of a type-II superconductor. Below $\mathbf{H}_{c1}$, the we find the Meissner state, with field excluded from the bulk in the same manner as for a type-I system. Between $\mathbf{H}_{c1}$ and $\mathbf{H}_{c2}$, however, we enter a distinct thermodynamic phase known as the mixed state, where the system permits magnetic flux to enter in discrete units of the flux quantum $\Phi_0 = h/2e$ in the form of magnetic 'flux lines'. This phenomenon was first predicted by Abrikosov (Abrikosov, 1957), where these flux lines are expected under self interaction to form an ordered 2D lattice, known as either the flux line lattice (FLL) or vortex lattice (VL) owing to the vortices of screening currents which flow around them. As the applied field is increased, the magnetisation follows until it passes zero at $\mathbf{H}_{c2}$ and the normal state is recovered. The magnetisation curves for a type-I and type-II superconductor are shown in figure 1.2.

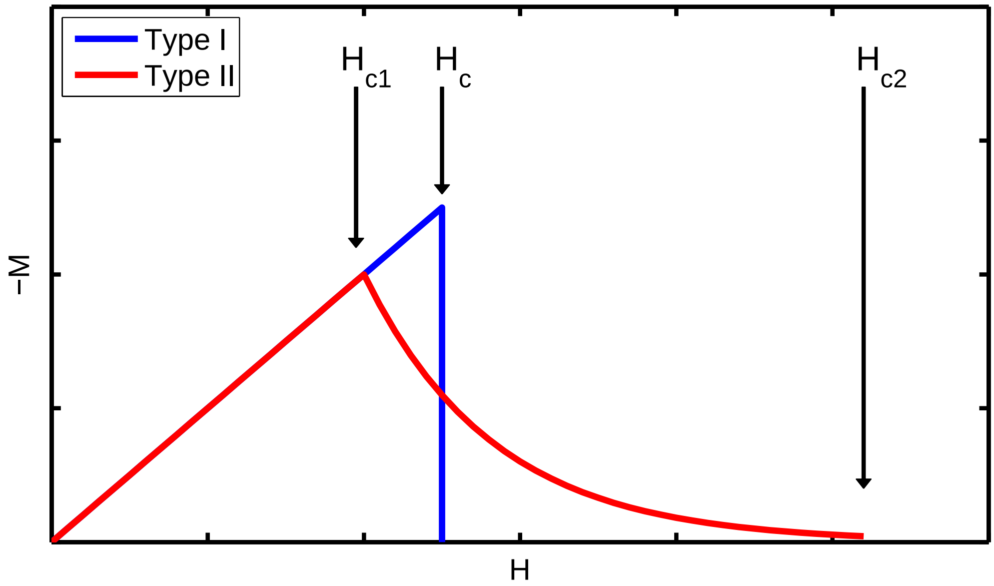

Figure 1.2: Magnetisation curves of both a Type I and Type II superconductor, with the critical field H_c of the type-I superconductor shown alongside the lower critical field H_{c1} and upper critical field H_{c2} of the type-II superconductor.

The boundary between type-I and type-II systems can be clearly seen by the change in response to externally applied fields, where the increasing population of the bulk by flux lines with increasing field allows superconductivity to survive in type-II materials well beyond critical fields of type-I superconductors. It is this spatially varying magnetic field, or vortex lattice, which forms the basis of the experimentation discussed in this thesis. Its behaviour is strongly correlated with the superconducting properties of the material, which allows measurements of the flux lattice to contribute to our understanding of the fundamental physics behind the superconductivity of type-II systems.

1.2 London Theory

In 1935 the brothers Fritz and Heinz London proposed that the basic electrodynamic properties of superconductivity, perfect conductivity (Onnes, 1911) and perfect diamagnetism (Meissner and Ochsenfeld, 1933), could be explained by two equations governing the macroscopic electric and magnetic fields of the system (London and London, 1935). Following Tinkham (Tinkham, 2004), the canonical momentum, $\mathbf{p}$, of a superconducting particle of mass $\hat{m}$, velocity $\mathbf{v}_s$ and electric charge $\hat{e}$ can be written as:

$$\mathbf{p} = \hat{m}\mathbf{v}_s + \hat{e}\mathbf{A} \tag{1.5}$$

where A is the vector potential. Considering this from a quantum mechanical perspective, the momentum $p \Rightarrow -i\hbar\nabla$, such that if we write the wavefunction of the superconducting condensate as $\psi = \sqrt{n_s}exp(i\theta)$ where n_s is the superconducting particle density and θ is the phase of the wavefunction, then our momentum $\mathbf{p} = -i\hbar\nabla\psi$. We adopt the gauge where, with no field applied, the ground state of the particle has zero momentum - $\nabla\psi = 0$. Here, we have $m\mathbf{v}_s = -q\mathbf{A}$ and we may write our supercurrent density as

$$\mathbf{j}_s = n_s\hat{e}\langle\mathbf{v}_s\rangle = -\frac{n_s\hat{e}^2}{\hat{m}}\mathbf{A} \tag{1.6}$$

with $\langle\mathbf{v}_s\rangle$ being the average particle velocity. This equation is only true if we assume that the ground state of the system is stable to the perturbation of a finite applied field, a condition is held by selecting the gauge to be $\nabla.\mathbf{A} = 0$, which is known as the London gauge. Taking the time derivative of equation 1.6, we find the first London equation,

$$\mathbf{E} = \frac{\hat{m}}{n_s\hat{e}^2}\frac{\mathrm{d}\mathbf{j}_s}{\mathrm{d}t} \tag{1.7}$$

which allows for a constant, or persistent, current flow $\mathbf{j}_s$ when there is no electric field i.e. $\mathbf{E}= 0$. We have therefore described the observed phenomena of perfect conductivity. Upon taking the curl of equation 1.6, we produce the second London equation

$$\nabla^2 \mathbf{B} = \frac{1}{\lambda_L^2} \mathbf{B} \tag{1.8}$$

where $\mathbf{B}$ is the internal field, and λ_L denotes the London penetration depth,

$$\lambda_L = \sqrt{\frac{\hat{m}}{\mu_0 n_s \hat{e}^2}} \tag{1.9}$$

To see how this describes the Meissner effect, we can apply a magnetic field $\mathbf{B}$ parallel to the plane of a superconductor. In this situation we can satisfy the second London equation with the following solution:

$$\mathbf{B}(x) = \mathbf{B}_0 \exp\left(\frac{-x}{\lambda}\right) \tag{1.10}$$

This describes an exponentially decaying magnetic field with distance into the superconductor, with the characteristic length scale of the London penetration depth. For situations where the scale of the superconductor is much larger than the London penetration depth, the second London equation successfully describes Meissner state, where the applied field is being excluded from the bulk of the superconductor.

The penetration depth is known to be temperature dependent, and has been empirically been found to follow the relation (Tinkham, 2004)

$$\lambda(T) = \lambda(0)\left(1 - \left(\frac{T}{T_c}\right)^4\right)^{-\frac{1}{2}} \tag{1.11}$$

Which corresponds to n$_s$ in the initial expression for the penetration depth, equation 1.9, decreasing with temperature as $(1 - t^4)$. Here $t = T/T_c$ is known as the reduced temperature, and is a common normalisation for dealing with temperature dependent properties in the superconducting state. This temperature-penetration depth relation is often known as the two-fluid temperature dependence, which is derived from an interpretation by Gorter and Casimir (Gorter G.J., 1934) of the superconducting state as a coexistence of normal and superconducting electron fluids.

1.3 London Theory and the Flux Line Lattice

We have seen that the London equations are capable of describing basic physical properties of the superconductor in the Meissner state. However, useful information regarding the mixed state of a superconducting system, where discrete quanta of flux pass through the bulk, can be derived from the London formalism. Following Ketterson and Song (Ketterson and Song, 1999), we use a two dimensional delta function we can consider a flux line in the superconductor in the following manner:

$$\lambda_L^2 \nabla^2 \mathbf{B} - \mathbf{B} = \Phi_0 \hat{\mathbf{z}} \delta^{(2)}(\mathbf{r}) \tag{1.12}$$

Where we use the two-dimensional delta function $\delta^{(2)}$ to describe the position of the flux line in a plane perpendicular to the unit vector $\hat{\mathbf{z}}$ along which the magnetic field is applied. The solution of this takes the form (Tinkham, 2004)

$$\mathbf{B}_{\hat{\mathbf{z}}}(\mathbf{r}) = \frac{\Phi_0}{2\pi\lambda_L^2} K_0\left(\frac{\mathbf{r}}{\lambda_L}\right) \tag{1.13}$$

which gives the spatial variation of magnetic field as a function of $\mathbf{r}$, the radial distance from the flux line. Here, K_0 is the zeroth order Bessel function, which for small x has the form $K_0(x) \approx -\ln x$, and at large x follows $K_0(x) \approx (\pi/2x)^{1/2} e^{-x}$. Therefore, close to the core of the flux line the London formalism takes the core to be infinitesimally narrow with the field being logarithmically divergent as you approach $\mathbf{r} = 0$. This represents an inherent flaw in London theory, as for a system to support a diverging field increasingly large and similarly divergent supercurrents are required. The divergent field stems from the assumption in London theory that the supercurrent $\mathbf{j}_s$ is dependent only on the vector potential A at that local point. In reality, owing to the finite size of a Cooper pair on a length scale ξ, the supercurrent density and vector potential have a non-local relation, the nature and consequences of which are the topic of a following section. Far form the core, however, the solutions to equation take a form consistent with the second London equation. This is equivalent to the solution obtained from a superconductor in the Meissner state where the field is applied perpendicular to the surface, giving our flux line a $(1/\mathbf{r})^{(1/2)}e^{(-|\mathbf{r}|)}$ decaying field away from the centre in all directions.

A flux line lattice is, however, comprised of a two dimensional array of vortices following the above description. In order to describe this FLL with London theory, we need to extend equation 1.13 to include an array of vortices.

$$\lambda_L^2 \nabla^2 \mathbf{B} - \mathbf{B} = \Phi_0 \hat{\mathbf{z}} \sum_i \delta^{(2)}(\mathbf{r} - \mathbf{r}_i) \tag{1.14}$$

Here, the sum is taken over i flux lines in a periodic vortex lattice, with vortex centres at position $\mathbf{r}_i$. For this description, we are able to expand $\mathbf{B}(\mathbf{r})$ as a Fourier series.

$$\mathbf{B}(\mathbf{r}) = \sum_{\mathbf{G}} \mathbf{B}_{\mathbf{G}} e^{i\mathbf{G}\cdot\mathbf{r}} \tag{1.15}$$

Where $\mathbf{G}$ represents the reciprocal space lattice vector and $\mathbf{B}_{\mathbf{G}}$ the Fourier coefficients of the expansion. Substituting equation 1.15 into equation 1.14 and integrating over the unit cell gives $\mathbf{B}_{\mathbf{G}}$ as

$$\mathbf{B}_{\mathbf{G}} = \frac{\Phi_0 n_L}{1 + \lambda_L^2 \mathbf{G}^2} = \frac{\langle B \rangle}{1 + \lambda_L^2 \mathbf{G}^2} \tag{1.16}$$

Where n_L is the area density of the vortices, which gives the average magnetic induction $\langle \mathbf{B} \rangle$ when multiplied by the flux quantum Φ_0. This Fourier expansion of the spatial variation of the magnetic field in a type-II superconductor in the mixed state is known as the form factor. Not only is it governed by the underlying superconducting properties of the system, which is seen at this stage by the inclusion of the penetration depth in the denominator, but this periodic variation of magnetic field forms the lattice off which neutrons diffract. The relation between the magnetic vortex lattice and the underlying superconducting state is what allows small angle neutron scattering to probe superconductivity in type-II materials, and as such the form factor proves to be one of the most important properties to investigate when using this technique. The London model is applicable to superconductors where $\lambda \gg \xi$, or strongly type-II systems, which are the subject of investigations in this thesis. The above picture in equation 1.16 provides a basic method of describing and interpreting our results, although it requires non-local corrections in order to work properly, which are detailed in the section on non-local corrections to London theory.

A further consequence of the local approximation in London theory is illustrated upon investigation of the London free energy. Following Ketterson and Song (Ketterson and Song, 1999), the free energy of a flux line as a function of radial distance, $\mathbf{r}$, from the centre of the flux line is given as

$$F = \frac{1}{2\mu_0}\int(\mathbf{B}^2 + \lambda^2(\nabla\times\mathbf{B}(\mathbf{r}))^2)d^3\mathbf{r} \tag{1.17}$$

As $\mathbf{r} \rightarrow 0$, this integral becomes logarithmically divergent owing to the solutions of the Bessel function in equation 1.13, which shows that London theory in its present form cannot be used to deduce the free energy of a vortex lattice. It is not until the assumption of locality is corrected that the London model is able to make predictions about the VL free energy, and thus its structure and coordination.

1.4 Anisotropic London Theory

In the discussion of London theory undertaken up to this point, it has been assumed that the superconductor we are studying is isotropic. For such an ideal case, the applied field experiences a uniform penetration depth in all directions and the flux lattice is not affected by rotations of the applied field with respect to the crystal structure. In reality, however, superconductors are not isotropic. Crystal structures of many superconductors are often strongly anisotropic, possessing tetragonal, orthorhombic or lower symmetries which in turn result in anisotropic electronic structures. As will be discussed later in the section on Abrikosov's derivation of a flux lattice in Ginzburg-Landau theory, a flux lattice residing in an isotropic environment assumes a hexagonal coordination, and the resulting diffraction patterns obtained from them in small angle neutron scattering are correspondingly hexagonal. Anisotropic London theory includes the effects of an anisotropic environment on the coordination of the flux lattice. The most simple way of taking these host material anisotropies into account when considering the flux lattice in London theory is to include the effective mass anisotropy in the London free energy. This is a relatively straightforward extension which does not require a significant alteration of the free energy integral, but rather generalises the effective mass term, $\hat{m}$, with a normalised effective mass tensor m_{ij} (Kogan, 1981) thereby by replacing the scalar term $\lambda^2 \nabla \mathbf{B}(\mathbf{r})^2$ with an invariant $\lambda^2 m_{ik} \nabla_i \mathbf{B}(\mathbf{r}) \nabla_k \mathbf{B}(\mathbf{r})$(Thiemann et al., 1989). Equation 1.17 therefore becomes

$$F = \frac{1}{2\mu_0} \int \left[\mathbf{B}^2 + \lambda_L^2 m_{ij} (\nabla_i \times \mathbf{B})(\nabla_j \times \mathbf{B}) \right] d^3\mathbf{r}. \tag{1.18}$$

The effective mass term is replaced by the effective mass tensor normalised to a geometric mean mass, $\bar{m}$, such that $m_{xx} = m_{\mathbf{a}}/\bar{m}$, $m_{yy} = m_{\mathbf{b}}/\bar{m}$, $m_{zz} = m_{\mathbf{c}}/\bar{m}$ and $\bar{m}^3 = m_{\mathbf{a}} m_{\mathbf{b}} m_{\mathbf{c}}$. If the effective mass tensor directions are chosen to lie along the principal axes of the host crystal then m_{ij} is is diagonal for orthorhombic or higher symmetries. Since the effective mass tensor acts as a scaling factor for the penetration depth term, we hereby define the directional penetration depth $\lambda_i \propto \sqrt{m_i^*}$ such that currents along i screen fields along j or k. Resultantly, in situations where for fields parallel to the $\mathbf{c}$ axis and $m_{\mathbf{a}}/m_{\mathbf{b}} \neq 1$, the FLL distorts along the direction of longest penetration depth. The structural distortion is represented by the anisotropy parameter $\gamma_{\mathbf{ab}} = \lambda_{\mathbf{a}}/\lambda_{\mathbf{b}}$, where an anisotropy parameter of one results in the isotropic hexagon with the diffraction spots lying on a circle, and an anisotropy parameter of $\gamma_{\mathbf{ab}} \neq 1$ results in the diffraction spots lying on an ellipse as the flux lattice is distorted. This is a scalar transformation, with the lattice being distorted by $\sqrt{\gamma_{\mathbf{ab}}}^{-1}$ along the **a** axis and by $\sqrt{\gamma_{\mathbf{ab}}}$ along the **b** axis (Thiemann et al., 1989). Whilst this does result in a predicted VL coordination based on a distortion from the isotropic hexagonal lattice, anisotropic London theory does not predict a specific VL orientation relative to the crystal axis. Given that a distorted VL coordination is related to the isotropic hexagonal lattice by a scalar transformation, any VL coordination that relates back to an isotropic lattice through this transform has an equivalent free energy (Campbell et al., 1988). This is true for all aspects of London theory presented so far - that all VL orientations with respect to the crystal axis are degenerate in terms of their free energy. For convenience, however, we have been assuming both that the field is applied parallel to a principal axis of the crystal and again that relation between the supercurrent, $\mathbf{j}_s$ and vector potential $\mathbf{A}$ is local, i.e. point like. For both models where the field is applied at an arbitrary angle to the crystal axis (Campbell et al., 1988) and those where supercurrent density-vector potential relationship is taken to be non-local (Kogan et al., 1996), preferred VL orientations are found.

To describe situations where the field was not applied along a principal crystal axis, this London representation of an anisotropic crystal lattice has been further extended to account for the affect of the field applied at an angle to the crystal axes. Figure 1.3 shows a representation of the field applied at an angle, θ, to the **c** axis. We have a rotation of the reference frame of the field components $\mathbf{B}_{x,y,z}$ onto a set of Cartesian coordinates [**x,y,z**] where the **z-x** plane is rotated by θ in the **b-c** plane of the crystal coordinates. From the perspective of our flux lattice, the field is applied along the **z** direction.

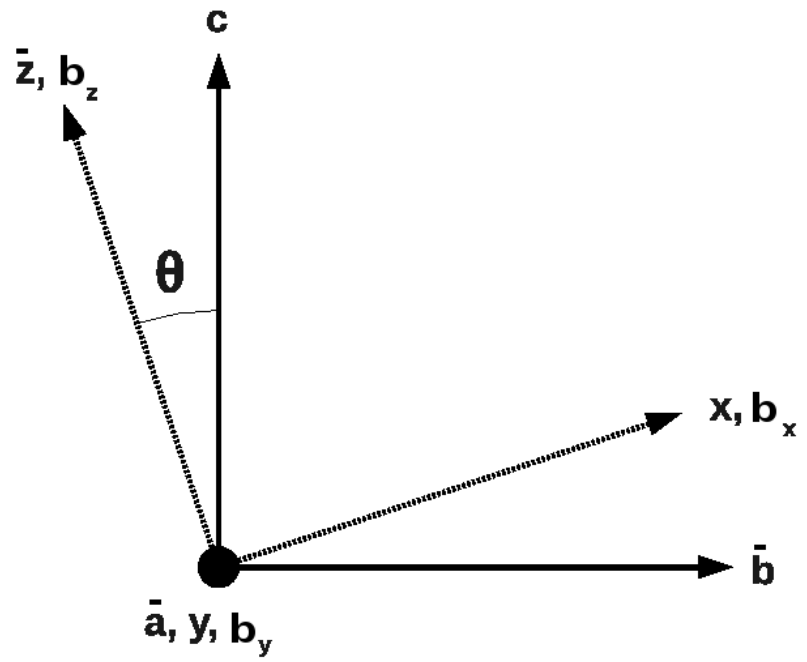

Figure 1.3: Diagram showing the rotation of the coordinate system describing the magnetic field components, $\mathbf{b_{x,y,z}}$ away from the Cartesian basis vectors of the crystal axes by an angle θ. Rotation takes place in the plane described by the **a** vector, meaning that **a** and **y** remain equivalent directions under this transformation.

Whilst initially described by Kogan (Kogan, 1981), here we follow the result of Thiemann *et al* (Thiemann et al., 1989) in describing the spatial modulation of magnetic field in the uniaxial approximation. We have the components, $\mathbf{b}_{x,y,z}$, of the Fourier coefficients of the applied field in the rotated frame of reference:

$$\mathbf{b}_x(\mathbf{q}) = \lambda^2 m_{xz}\mathbf{q}_y^2\mathbf{B}/d \tag{1.19}$$

$$\mathbf{b}_y(\mathbf{q}) = -\lambda^2 m_{xz}\mathbf{q}_x\mathbf{q}_y\mathbf{B}/d \tag{1.20}$$

$$\mathbf{b}_z(\mathbf{q}) = (1 + \lambda^2 m_{zz}\mathbf{q}^2)\mathbf{B}/d \tag{1.21}$$

where $\mathbf{q}_{x,y}$ are the Cartesian components of **G** in the plane perpendicular to **B**, and d is given by:

$$d = (1 + \lambda^2 m_{yy}\mathbf{q}_x^2 + \lambda^2 m_{xx}\mathbf{q}_y^2)(1 + \lambda^2 m_{zz}\mathbf{q}^2) - \lambda^4 m_{xz}^2 \mathbf{q}^2 \mathbf{q}_y^2 \tag{1.22}$$

where $\mathbf{B}$ is the average field, λ is the penetration depth for the average mass, and the components of the effective mass tensor m_{ij} have become

$$m_{xx} = m_{\mathbf{b}} \cos^2\theta + m_{\mathbf{c}} \sin^2\theta \tag{1.23}$$

$$m_{xz} = (m_{\mathbf{b}} - m_{\mathbf{c}}) \sin\theta \cos\theta \tag{1.24}$$

$$m_{zz} = m_{\mathbf{b}} \sin^2\theta + m_{\mathbf{c}} \cos^2\theta \tag{1.25}$$

We can see that with non-zero θ, and $m_{\mathbf{b}} \neq m_{\mathbf{b}}$, there must exist transverse field components $\mathbf{b}_x(\mathbf{q})$ and $\mathbf{b}_y(\mathbf{q})$. The lattice distortion that arises from this has been generalised in terms of the angle, θ and the effective mass anisotropies as:

$$\nu^2 = \left(\frac{\tan\phi}{\tan 30^0}\right)^2 = \left(\gamma_{\mathbf{ab}}^2 \cos^2\theta + \frac{1}{\gamma_{\mathbf{ac}}^2} \sin^2\theta\right)^{-\frac{1}{2}} \tag{1.26}$$

Where $\gamma_{\mathbf{ab}}^2 = m_{\mathbf{a}}/m_{\mathbf{b}}$, $\gamma_{\mathbf{ac}}^2 = m_{\mathbf{c}}/m_{\mathbf{a}}$ and the lattice distortion ν is defined by the ratio of angles between the basis vectors of the observed and isotropic lattice. Such a relation is very useful in neutron scattering, a technique ideally suited to investigating the coordination of the VL, as it allows us to relate the distortion in our diffraction patterns to fundamental properties of the superconductor under investigation.

1.5 Non-Local corrections to London Theory

So far in the discussion of London theory, it has been assumed that the supercurrent density, $\mathbf{j}_s(\mathbf{r})$ is *locally* dependent on $\mathbf{A}(\mathbf{r})$: that the proportionality is point like for any given $\mathbf{r}$. However, the charge carriers in a superconductor have a finite size with a length scale which is large enough with respect to other properties of the system such that a point like approximation is no longer valid. This led Pippard (Pippard, 1953) to suggest that the relationship between $\mathbf{j}_s(\mathbf{r})$ and $\mathbf{A}(\mathbf{r})$ is non-local, where the supercurrent density would depend on the values of $\mathbf{A}(\mathbf{r})$ within a certain volume of space. This non-local generalisation of the London equation would take the form (Tinkham, 2004)

$$\mathbf{j}_s(\mathbf{r}) = \frac{3n_s\hat{e}^2}{4\pi\hat{m}\xi_0}\int\frac{\mathbf{R}(\mathbf{R}\cdot\mathbf{A}(\mathbf{r}'))}{\mathbf{R}^4}e^{-R/\xi_0}\mathrm{d}\mathbf{r}' \tag{1.27}$$

where $\mathbf{R} = \mathbf{r} - \mathbf{r}'$, and the characteristic length scale of this volume, known as the Pippard coherence length, was given the label ξ_0. This was later found to be of the same order as the size of the Cooper pair, the superconducting charge carrier which emerged in the microscopic description of superconductivity (Bardeen et al., 1957). For situations where $\mathbf{A}(\mathbf{r})$ varies over this scale, the supercurrent response would be modified from the value expected from local electrodynamics. In the case of flux lines, this can result in a weakening of the supercurrent response near the core, allowing the field to penetrate over distances greater than λ_L. Non local effects are most important for type-I superconductors ($\lambda_L < \xi_0$) and for weakly type-II ($\lambda_L \approx \xi_0$), as for situations where $\lambda_L < \xi_0$, $\mathbf{A}(\mathbf{r})$ can vary rapidly over distances smaller than ξ_0. As superconductors become more strongly type-II, we head towards the situation where $\lambda_L/\xi_0 \to \infty$, where the local limit is recovered, although non-local effects are still important even for strongly type-II materials (Kogan et al., 1996, 1997). Many strongly type-II materials possess nodes in their superconducting gap as a function of position, which causes a diverging coherence length as the gap approaches zero. Non-local effects must therefore be important in these materials despite their high values of λ_L/ξ_0.

Non-local corrections become important when considering the spatial variation of magnetic field in the flux lattice. Whilst strongly type-II systems are tending towards the local limit, it was seen in the previous section that it is an inherent flaw of the local approximation to predict logarithmically divergent fields at the centre of a flux line (see equation 1.13). Since this situation is obviously unphysical, it is common to correct the London prediction for the VL form factor in equation 1.16 with a non-local term forcing the previously infinitesimally small core to occupy a size related to the coherence length (Ichioka et al., 1996). It is for this reason that it is commonly known as a core correction factor, and takes the form $\exp(-c\mathbf{G}^2\xi_0^2)$, where $\mathbf{G}$ is the reciprocal space lattice vector, ξ_0 is the coherence length which corresponds to the Cooper pair size and c is a scaling factor which commonly takes values around 0.5. The core correction factor transforms equation 1.16 into

$$B_G = \frac{\langle B\rangle \exp(-c\mathbf{G}^2\xi_0^2)}{1+\lambda_L^2\mathbf{G}^2} \tag{1.28}$$

This model for the form factor is a good approximation in situations far from H_{c2}, such as with the cuprate superconductors or pnictides which have a high upper critical field, both of which are subjects of investigation later in this thesis.

London theory with non-local corrections have been used to predict the orientation and structural coordination of the vortex lattice. As detailed in the section of this thesis on the Abrikosov lattice 1.9, the flux lines which permeate a type-II superconductor in the mixed state have a free energy dependant on their coordination, which in an isotropic system is minimised in a hexagonal lattice. However, many superconductors deviate quite significantly from this ideal approximation, with the most classic case being the cuprate family of superconductors which possess neither an isotropic crystal structure or superconducting gap. Theoretical models which have been developed to handle these situations approximate the anisotropy in the system either to be in the superconducting gap or Fermi velocity. The non-local theory of Kogan et al (Kogan and Miranović, 1997; Kogan et al., 1997), which assumes an isotropic superconducting gap in the presence of an anisotropic Fermi velocity, has proven successful in predicting the vortex lattice orientation for a variety of non-trivial superconducting systems. Kogan's non-local theory starts by considering an isotropic superconductor and derives the London equations from the perspective of Eilenberger theory, which provides a quasi-classical description of the microscopic theory to be detailed in section on BCS theory 1.6. Following Kogan's non-local theory, the general form of the London equation in reciprocal space is stated as

$$\mathbf{j}_i = -\frac{\lambda^{-2}}{\mu_0}(m_{ij}^{-1} - \lambda^2 n_{ijlm}\mathbf{G}_l\mathbf{G}_m)\mathbf{a}_j \tag{1.29}$$

where the vector potential is given by $\mathbf{a}_j = \mathbf{A} + \Phi_0\nabla\theta/2\pi$, where θ is the phase of the condensate wavefunction, m_{ij} is the normalised inverse mass tensor, λ is the average penetration depth, $\lambda = (\lambda_{\mathbf{a}}\lambda_{\mathbf{b}}\lambda_{\mathbf{c}})^{1/3}$ and $\mathbf{G}$ describes the vectors of the reciprocal lattice. Here, the tensor n_{ijlm} couples the supercurrents of the VL to the microscopic properties of the Fermi surface as given by

$$n_{ijlm} = \frac{\hbar\langle v_i v_j v_l v_m\rangle\gamma(T,\tau)}{4\Delta_0^2\lambda^2\det\langle v_i v_j\rangle^{1/3}} \tag{1.30}$$

where v_i describes the i^{th} component of the Fermi velocity, γ is temperature dependent parameter arising from impurity scattering and gap size, Δ_0, and $\langle ...\rangle$ indicates an average over the Fermi surface.

To determine the preferred orientation of the VL, the general form of the London equation in reciprocal space (equation 1.29) is used to evaluate the Fourier components of the field distribution for any one particular VL orientation. These components can then be used to calculate the free energy density, which for a VL running parallel to the fourfold axis vector is given by:

$$F = \frac{\mathbf{B}^2}{2\mu_0}\sum_{\mathbf{G}}\frac{1}{1 + \lambda^2\mathbf{G} + \lambda^4(n_2\mathbf{G}^4 + (2n_1 - 6n_2)\mathbf{G}_1^2\mathbf{G}_2^2} \tag{1.31}$$

From the coupling of the VL to the crystal anisotropy through the inverse mass tensor, this free energy density will possess a structure dependent minimum for any applied field. Calculations based on this approach, which in the initial publication are relevant to both fourfold and twofold situations but were later shown to be fourfold applicable only (White et al., 2011), take the shape of the VL in terms of the two basis vectors of the primitive cell separated by the angle β and output the free energy at each field. The shape which minimises this free energy is that which is predicted to arise in experiment. This literature predicts a structural reorientation transition for the fourfold case, and later a stabilisation into a square structure at high field - which is relevant to the YBCO research described later 3. The nearest neighbour directions are aligned along the Fermi velocity minima in this square phase. This theory has been successful in describing the VL of YNi_2B_2C (Paul et al., 1998) and somewhat in V_3Si (Yethiraj et al., 1999).

1.6 BCS

BCS theory, derived by Bardeen Cooper and Schrieffer and published in 1957 (Bardeen et al., 1957), was the first microscopic description of superconductivity. It arises from the idea from Frölich (Fröhlich, 1950) that due to electron-phonon coupling, electrons could sometimes experience an attractive potential. Following this, Cooper (Cooper, 1956) showed that electrons interacting just above a filled Fermi surface could form a bound state, or 'Cooper pair', for an arbitrarily weak potential. In this section, we follow the treatments of Ketterson and Song (Ketterson and Song, 1999) and Tinkham (Tinkham, 2004). Considering the Coulomb interaction between two electrons

$$V(\mathbf{r}) = \frac{1}{4\pi\epsilon_0}\frac{e^2}{\mathbf{r}} \tag{1.32}$$

one can see that this interaction alone gives a repulsive potential, and thus cannot describe superconductivity. Further, accounting for a lattice where the Coulomb potential from the electrons will be screened by the positively charged lattice at large distances does not allow for a attractive interaction. In order for a negative potential to arise it is necessary to consider the motion of the ions within the lattice. In this situation, where the lattice is no longer assumed to be rigid, it is envisaged that the first electron polarises the lattice by attracting the positively charged ions, creating a region of positive charge density, which will be attractive to a second electron. It is clear that this lattice-based interaction must therefore be phonon mediated, and from momentum conservation it can be seen that if an electron is scattered from $\mathbf{k}$ to $\mathbf{k}'$, a virtual phonon must therefore carry the momentum $\mathbf{q} = \mathbf{k} - \mathbf{k}'$. It is expected that the lowest energy state for the two particle wavefunction describing this system to have zero total momentum, meaning the electrons forming a Cooper pair must have equal and opposite momenta. The wavefunction of a Cooper pair will take the form

$$\psi(\mathbf{r}_1, \mathbf{r}_2) = \phi_{\mathbf{q}}(\rho) e^{i\mathbf{q}\cdot\mathbf{R}} \chi(\sigma_1, \sigma_2) \tag{1.33}$$

where, $\rho = |\mathbf{r}_1 - \mathbf{r}_2|$, $\mathbf{R}$ is the centre of mass coordinate and σ_1, σ_2 are the electron spins. The $\phi_{\mathbf{q}}(\rho)$ term represents the spatial component of the wavefunction, whilst $\chi(\sigma_1, \sigma_2)$ contains the spin component. It can be seen that the charge carriers in superconductors, Cooper pairs, must have mass $2m_e$ and charge $2e$, which in previous sections have been denoted by $\hat{m}$ and $\hat{e}$ respectively. Conservation of Fermionic antisymmetry of the wavefunction with respect to particle interchange suggests a spin singlet wavefunction.

$$\chi(\sigma_1, \sigma_2) = \frac{1}{\sqrt{2}}(|\uparrow\downarrow\rangle - |\downarrow\uparrow\rangle) \tag{1.34}$$

This wavefunction describes two particles of equal and opposite momenta with opposite spin. Since this gives the particle no angular momentum, $\ell = 0$, this is an s-wave state. Showing that the Fermi sea is unstable against the formation of a Cooper pair in the presence of an attractive potential, it is expected that pairs will condense until some equilibrium is reached. BCS used a single coherent wavefunction to describe all of the condensed pairs in the system, taking a ground state wavefunction of the form:

$$|\psi_{\mathbf{G}}\rangle = \prod_{\mathbf{k}=\mathbf{k}_1,\ldots,\mathbf{k}_M} (u_{\mathbf{k}} + v_{\mathbf{k}} c^*_{\mathbf{k}\uparrow} c^*_{-\mathbf{k}\downarrow}) |\phi_0\rangle \tag{1.35}$$

Where c^*_x is the creation operator for a particle in the state x, such that $c^*_{\mathbf{k}\uparrow} c^*_{-\mathbf{k}\downarrow}$ is the creation operator for a pair of electrons of zero momentum and opposite spin. The functions $u_{\mathbf{k}}$ and $v_{\mathbf{k}}$ give the probability that a pair state is occupied or unoccupied respectively, such that $|u_{\mathbf{k}}|^2 + |v_{\mathbf{k}}|^2 = 1$, and $|\phi_0\rangle$ is the vacuum state upon which the operators are acting. This wavefunction can then be used to minimise the energy of the BCS Hamiltonian

$$\hat{H} = \sum_{\mathbf{k},\sigma} \left(\frac{\hbar^2 \mathbf{k}^2}{2m} - \mu \right) c^*_{\mathbf{k}\sigma} c_{-\mathbf{k}\sigma} + \sum_{\mathbf{k}\mathbf{k}'} V_{\mathbf{k}\mathbf{k}'} c^*_{\mathbf{k}\uparrow} c^*_{-\mathbf{k}\downarrow} c_{\mathbf{k}'\uparrow} c_{-\mathbf{k}'\downarrow} \tag{1.36}$$

where $V_{\mathbf{k}\mathbf{k}'}$ is the matrix element describing the two particle interaction and μ is the chemical potential. Minimisation by treating $|u_{\mathbf{k}}|$ and $|v_{\mathbf{k}}|$ as variational parameters and seeking to minimise the energy yields

$$E_{\mathbf{k}} = \sqrt{\left(\frac{\hbar^2 \mathbf{k}^2}{2m} - \mu \right)^2 + |\Delta_{\mathbf{k}}|^2} \tag{1.37}$$

where $\Delta_{\mathbf{k}}$ is the superconducting gap function, an energy gap of magnitude Δ across the Fermi surface. Here, the system has been considered isotropic such that $\Delta_{\mathbf{k}}$ is independent of $\mathbf{k}$. Below energies of Δ, single particle states are inaccessible.

The triumph of BCS theory was to encapsulate the condensation of electrons into a set of bound states, or the Cooper sea, which is described by a single coherent wavefunction. The condensation of Cooper pairs is related to the formation of an energy gap across the whole Fermi surface. This gap was shown by Gor'kov (Gor'Kov, 1958) to be directly analogous to the Ginzburg-Landau wavefunction, ψ, which represents the wavefunction of the centre of mass of the Cooper pair, which will be discussed in a later section 1.8. BCS theory also shows that single particle states are unavailable for excitation energies below Δ, but appear for those greater than the BCS energy gap with varied electron or hole like character dependent on the respective values of $|v_{\mathbf{k}}|$ and $|u_{\mathbf{k}}|$ (Ketterson and Song, 1999). These single particle states, or quasiparticles, have been shown to emerge at the centre of a flux line, forming the 'normal' core (Caroli and Matricon, 1964; Bardeen et al., 1969). In summary, BCS provides a theory to explain macroscopically observable phenomena from microscopic physics.

1.7 Unconventional Superconductivity

For conventional superconductivity, the discussion of BCS theory in the previous section describes a system where the system was assumed isotropic such that the superconducting gap $\Delta_{\mathbf{k}}$ possessed spherical symmetry. Here, the Cooper pairs form a singlet pairing state with $\ell = 0$ and thus it is often referred to as an s-wave state. However, for situations where the system is no longer isotropic, it is expected that $\Delta_{\mathbf{k}}$ will also be anisotropic, and have $\mathbf{k}$ dependence with the same symmetry as the underlying crystal. The variation of $\Delta_{\mathbf{k}}$ with $\mathbf{k}$ does not have to be simple, but for conventional superconductivity cannot have symmetry lower than that of the underlying crystal. Unconventional pairing, and thus unconventional superconductivity, refers to the situation where the symmetry of the superconducting gap is lower than that of the parent crystal. Here, pairing states exist where $\ell \neq 0$ and Cooper pairs may posses angular momentum.

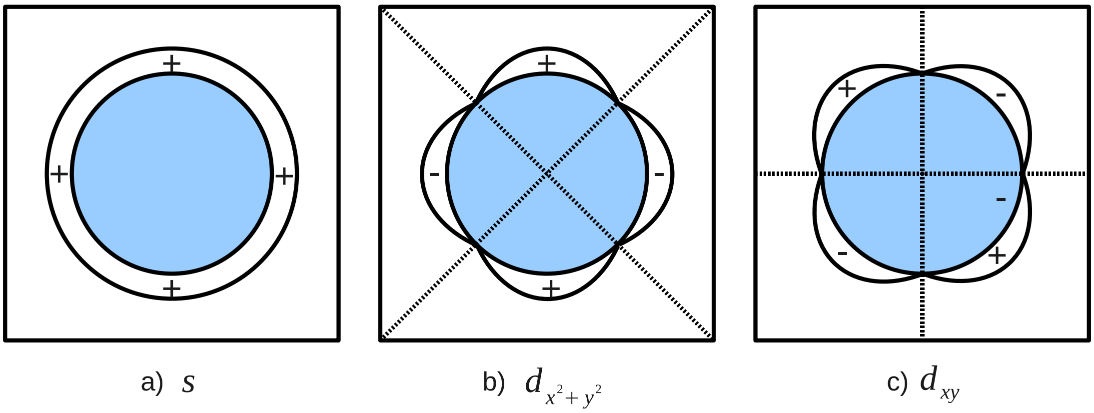

a) s b) $d_{x^2+y^2}$ c) d_{xy}

Figure 1.4: a) An s-wave superconducting gap, b) a $d_{x^2-y^2}$ gap and c) a d_{xy} gap. The + and − refer to the phase of the order parameter, where the dashed lines represent planes of broken symmetry.

Figure 1.4 gives representations of s, $d_{x^2-y^2}$ and d_{xy} wave gap functions over a two dimensional representation of the Fermi surface. It can be seen that, whilst the isotropic s-wave gap posses spherical symmetry, the unconventional pairing states do not. The cuprate superconductors, a member of which is the subject of investigations presented in this thesis, known to have the $d_{x^2-y^2}$ gap shown in figure 1.4. This gap posses lower symmetry than the often tetragonal unit cell of many cuprates, being odd under a 90° rotation and about the mirror reflections along the dotted lines. These gap functions have the same symmetry properties as atomic orbital functions, with the s-wave state having $\ell = 0$ and the d-wave states having $\ell = 2$.

The nodes present in the d-wave gap function provide an important experimental distinction between the conventional s-wave superconductors and their unconventional d-wave counterparts, or indeed any superconductor with a nodal order parameter. Nodes in the gap function allow quasiparticle excitations to exist for arbitrary values of $k_B T$, indeed down to zero temperature, whereas the superfluid in a fully gapped superconductor will saturate at a temperature T for which $\Delta_0 = k_B T$. According to equation 1.9 , the superfluid density governs the London penetration depth, which is an experimentally accessible quantity. It is, however, not always possible to distinguish between different types of nodes by measurements of the London penetration depth alone (Kawano-Furukawa et al., 2011).

As new families of superconductors continue to be discovered, we see continued departure from the s-wave phonon mediated pairing interaction used to describe the classical superconductors. A variety of unconventional pairing states have been suggested for the recently discovered iron based superconductors, or pnictides. The proximity and possible co-existence of superconductivity and magnetism coupled with a complex family of underlying crystal structures has led to experimental evidence pointing towards several different pairing states. So far, the $s\pm$ pairing state seems to be the most robust proposal, which the majority of the superconducting community and experimental evidence seems to support. Like its conventional counterpart, the $s\pm$ state possesses the same symmetry as its parent lattice. However, unlike the phonon mediated interaction found in the s-wave state, superconductivity relies on a spin fluctuation mediated interaction between electron and hole sheets of the Fermi surface, which possess opposite gap signs.

The effect on the VL of the underlying superconducting state forms the focus of study within this thesis, and has been the subject of detailed study for many years. The first description of the effect of a d-wave order parameter on a flux line was carried out by Soininen et al. (Soininen et al., 1994), who solved the Bogoliubov-de Gennes equations for the quasiparticles as a function of distance from the centre of the flux line. Three regions in a shell like arrangement were predicted, with distinctly different behaviour. In the centre of the flux line the order parameter was expected to fall to zero, with bound Fermionic states occupying this region which is known as the inner core. Around this, at a further distance from the centre, is the outer core. Here, both s- and d wave order parameters exist, mainly with a non-zero relative phase. Quasiparticle excitations here are gapped, except in the regions where the two order parameters interfere destructively and thus for nodes. Around this, and extending across the bulk of the superconductor, is the pure d-wave superconductor. This detailed structure is expected to influence the inter-vortex interactions.

1.8 Ginzburg-Landau Theory

Ginzburg-Landau (GL) theory (Ginzburg and Landau, 1950) is a phenomenological description of the superconducting state based on Landau's theory of phase transitions. Whilst it chronologically precedes BCS theory (Bardeen et al., 1957), it was shown by Gor'kov that the gap function in BCS directly relates to the order parameter used in GL theory (Gor'Kov, 1958). Here we follow the treatment of Ketterson and Song (Ketterson and Song, 1999). The theory considers the ordering process occurring in many phase transitions, and defines an order parameter associated with this: in the case of superconductivity, n_s, the Cooper pair density, formerly referred to as the superconducting particle density before the introduction of Cooper pairs. Landau introduced the idea that this order parameter can be externally constrained, in which case the free energy density would therefore take some function $F(n_s)$ of the constraint. Upon removal of the constraint, the system will settle at the absolute minimum of $F(n_s)$.

To consider situations where n_s was not constant throughout the superconductor, Ginzburg and Landau used a complex order parameter, ψ. Since the free energy density should be real, an expansion for small ψ was taken in powers of $|\psi|^2$, where $|\psi|^2 = n_s$.

$$F = F_0 + \alpha|\psi|^2 + \frac{\beta}{2}|\psi|^4 \tag{1.38}$$

F_0 is therefore the free energy density of the normal state, as when $|\psi|$ is zero this is the only remaining term. In an unconstrained situation, the free energy will come to rest at its minimum, where

$$\frac{dF}{d|\psi|^2} = \alpha + \beta|\psi|^2 = 0. \tag{1.39}$$

In the simplest case, this is minimised by taking β to be constant and giving α a linear temperature dependence, changing sign as it passes through T_c. We can therefore say that

$$|\psi|^2 = -\frac{\alpha}{\beta} \tag{1.40}$$

so

$$F_n - F_s = \frac{\alpha^2}{2\beta} \tag{1.41}$$

and thus, substituting in for the condensation energy,

$$B_c(T) = \alpha\sqrt{\frac{\mu_0}{\beta}} \tag{1.42}$$

Which constrains β to be positive. In situations where α is positive, the minimum of the free energy lies at $|\psi| = 0$, which describes the normal state. For negative alpha, the minimum lies below this and the superconducting state is energetically favourable. This, however, only describes a superconductor in the absence of a magnetic field. For situations with an applied field, both a magnetic energy density term and a gradient term (for spatial variations in the order parameter) need to be added. The gradient term is directly analogous to the kinetic energy term of a Hamiltonian for a charged particle in an electromagnetic field, taking the form

$$\frac{\hbar^2}{4m}|\nabla\psi(r)|^2 \Rightarrow \frac{\hbar^2}{4m}\left|\left(\nabla - \frac{2ieA}{\hbar}\right)\psi(r)\right|^2 \tag{1.43}$$

where m and e describe the electron mass and charge respectively and A is the vector potential. Here, the mass and charge of the Cooper pair has been included, having been introduced in the previous section on the microscopic BCS theory of superconductivity 1.6. It should be noted, however, that since the Ginzburg-Landau description of superconductivity pre-dates BCS this correction would not have been in the original theory. Including these in the term for free energy density gives

$$F = F_0 + \frac{B^2}{2\mu_0} + \alpha|\psi|^2 + \frac{\hbar^2}{4m}\left|\left(\nabla - \frac{2ieA}{\hbar}\right)\psi(r)\right|^2 + \frac{\beta}{2}|\psi|^4 \tag{1.44}$$

Minimising this with respect to $\psi(r)$ and $\psi^*(r)$ yields the first GL equation

$$\frac{\hbar^2}{4m}(\nabla - \frac{2ieA}{\hbar})^2\psi(r) + \alpha(T)\psi(r) + \beta|\psi(r)|^2\psi(r) = 0. \tag{1.45}$$

Whilst performing the same minimisation but this time with respect to the vector potential, A, gives the second GL equation

$$j_s = \frac{ie\hbar}{2m}(\psi^*(r)\nabla\psi(r) - \psi(r)\nabla\psi^*(r)) - \frac{2e^2}{m}|\psi(r)|^2 A. \tag{1.46}$$

These can then be used to define the Ginzburg-Landau length scales. Solving the first GL equation, in the absence of an electromagnetic field, gives the GL coherence length

$$\xi(T) = \sqrt{\frac{\hbar^2}{4m|\alpha(T)|}}. \tag{1.47}$$

This defines the length scale over which the GL order parameter can vary from the bulk value to zero. The GL penetration depth λ is found by considering the second GL equation under the expectation that the ground state of the superconducting particles have zero momentum, where $\nabla\psi = 0$, such that the first two terms on the right hand side do not contribute.

$$j_s = \frac{e^2}{m}|\psi(r)|^2 A = -\frac{n_s e^2}{m} A \tag{1.48}$$

Which is equivalent to the London relation, Where we can see $n_s = |\psi|^2$, which gives the GL penetration depth as

$$\lambda(T) = \sqrt{\frac{m\beta}{2\mu_0 e^2 \alpha(T)}} \tag{1.49}$$

These two length scales define differing regimes for a superconductor when considering the superconducting to normal interface at the upper critical field, H_{c2}. In one case, we can consider $\lambda \gg \xi$, where the field varies slowly in comparison to the sharp change in the order parameter. In contrast, for $\xi \gg \lambda$, we have a rapid variation in field and a slow variation in the order parameter. It was shown by de Gennes (de Gennes, 1989) when considering the superconducting to normal interface that the surface energy for the latter limit is positive, and so the boundary between the superconducting and normal states attempts to minimise its area. For the first limit, however, the surface energy is negative and so it is energetically favourable for the boundary to maximise its area. This case was not considered possible until the predictions by Abrikosov, discussed in the next section, describing the flux line lattice which can exist in a type-II superconductor. The GL penetration depth and coherence length can be used to define a dimensionless ratio, κ,

$$\kappa = \frac{\lambda(T)}{\xi(T)} \tag{1.50}$$

which is temperature independent within GL theory, i.e. close to T_c. The parameter κ gives the boundary between type-I and type-II superconductivity at

$$\kappa = \frac{1}{\sqrt{2}}. \tag{1.51}$$

1.9 The Abrikosov Lattice

For a type-II superconductor in an applied field, where H_{app} is close to H_{c2}, the GL order parameter, ψ, can be considered small as the number of cooper pairs in the material shrinks to zero at the transition point. In this limit of ψ being small, we can drop the cubic $|\psi(r)|^2\psi(r)$ term from the first GL equation and linearise it, taking the form

$$-\frac{\hbar^2}{4m}\big(\nabla - \frac{2ie}{\hbar}\mathbf{A}\big)^2\psi(r) + \alpha\psi(r) = 0. \tag{1.52}$$

Here, we choose the Landau gauge $\mathbf{A} = (0, Bx, 0)$, which equates to a field $\mathbf{B} = (0, 0, B)$, the first GL equation can now be written as

$$\left(-\frac{\hbar^2}{4m}\nabla^2 + i\hbar\omega_c x\frac{\partial}{\partial y} + m\omega_c^2 x^2\right)\psi(r) = -\alpha\psi(r) \tag{1.53}$$

where ω_c is the cyclotron frequency $\omega_c = eB/m$. This has the same form as the Schrodinger equation for a charged particle in a uniform field with energy eigenvalue α. Using a trial function of the form $\psi(r) = exp(i(k_y y + k_z z))f(x)$, for plane wave solutions along y and z and an unknown function in x, the linearised first GL equation takes the form

$$-\frac{\hbar^2}{4m}\frac{\mathrm{d}^2 f}{\mathrm{d}x^2} + m\omega_c\left(x - \frac{\hbar k_y}{2m\omega_c}\right)^2 f = \left(\mid\alpha\mid - \frac{\hbar^2 k_z^2}{4m}\right)f \tag{1.54}$$

Which has the form of the Schrodinger equation for a simple harmonic oscillator, having energy eigenvalues

$$\mid\alpha\mid = \big(n + \frac{1}{2}\big)\hbar\omega_c + \frac{\hbar^2 k_z^2}{4m}. \tag{1.55}$$

The lowest Landau level solution to this will have $n = 0$ and $k_z = 0$. Substituting this back into the cyclotron frequency, we obtain an expression for the upper critical field

$$B_{c2} = \frac{\phi_0}{2\pi\xi^2(T)}. \tag{1.56}$$

This expression implies that under an applied field there exists one flux quantum per unit area $2\pi\xi^2(T)$. However, further from H_{c2}, one can no longer consider the cubic $|\psi(r)|^2\psi(r)$ term to be small, and the solutions to the first GL equation become more difficult to find. Investigation of this non-linear equation were first carried out by Abrikosov (Abrikosov, 1957). Expecting the solutions to the non linear equation to resemble the SHO form of the solutions to the linearised equation, and that only the lowest Landau level solutions would be significant, the trial function becomes

$$\psi(\mathbf{r}) = Ce^{ik_y y}e^{-(x-x_0)^2/\xi^2(T)} \tag{1.57}$$

where C is a normalisation constant which vanishes for $\mathbf{H} = \mathbf{H}_{c2}$. This solution is of Gaussian form, with with of order of the GL coherence length. However, this allows for any number of k_y values, for as long as x_0 lies within the superconductor, giving us a highly degenerate solution. To circumvent this, Abrikosov found solutions periodic in y such that k_y values were limited to $k_y = 2\pi n/l_y$ for integer n. The trial function now takes the form

$$\psi(\mathbf{r}) = \sum_{n=-\infty}^{n=\infty} Ce^{i(2\pi ny/l_y)}e^{-(x-x_n)^2/\xi^2(T)} \tag{1.58}$$

where C is now a common normalisation constant and $x_n = n\xi^2 k_y$. Periodicity in x is defined by $l_x = n'\Phi_0/Bl_y$ for integer n'. These periodicity conditions describe the formation of the flux lattice, the periodic penetration of the superconducting bulk by lines of magnetic field, with a single flux quantum per unit cell.

Abrikosov used the above trial wavefunction to solve the first GL equation for a square VL, with the free energy density resulting from this having the form

$$F = F_0 + \frac{1}{2\mu_0}\left(B^2 - \frac{(B-\mu_0 H_{c2})^2}{1+\beta_A(2\kappa^2-1)}\right) \tag{1.59}$$

where the value of the Abrikosov parameter β_A was calculated to be 1.18 for a square lattice in Abrikosov's original paper (Abrikosov, 1957). Later, Kleiner et al (Kleiner et al.,

1964) discovered that for the hexagonal lattice this parameter would take the value 1.16, giving the hexagonal lattice a lower free energy that the square by around $\approx 2\%$. This small difference means that the VL is very sensitive to anisotropies in the system, which can therefore express themselves as a VL coordination other than the isotropic hexagon.

1.10 Small angle neutron scattering

1.11 Magnetic scattering of neutrons from a periodic potential

Small angle neutron scattering (SANS) is a bulk measurement, in which the VL is observed through scattering of incident neutrons from the spatially varying periodic field that makes up the lattice. This lattice is a 2D system consisting of flux lines containing one flux quantum per unit cell, with spacing between lines given by

$$d = \sqrt{\frac{\sigma\Phi_0}{B}} \tag{1.60}$$

where σ is 1 for a square lattice and $2/\sqrt{3}$ for a triangular one. For an applied field of 1 T, this equates to a d spacing of around 40 nm, a distance which is larger than the atomic spacing of the host crystal.

Neutrons, possessing a magnetic moment of $\mu_n = 9.66 \times 10^{-27}$ J T^{-1}, experiences V($\mathbf{r}$), a varying potential when passing through the array of flux lines in a vortex lattice. The potential for a neutron in an applied field is

$$V(\mathbf{r}) = -\mu \cdot B. \tag{1.61}$$

This potential is much less than the kinetic energy of a cold neutron, which for our experiments posses an average wavelength of around 7 Å, and therefore a kinetic energy of $\approx 2.67 \times 10^{-22}$ J. Following Schiff (Schiff, 1968) and Squires (Squires, 1996), we consider the potential arising from the VL to be a perturbation. Considering the plane wave representation of an incident neutron scattering off the potential $V(\mathbf{r})$, with incoming wavevector $\mathbf{k}$ and outgoing wavevector $\mathbf{k}'$, we can use Fermi's golden rule to calculate the differential scattering cross section, which gives the probability of a neutron to be scattered into the solid angle dΩ,

$$\frac{d\sigma}{d\Omega} = \left(\frac{m_n}{2\pi\hbar^2}\right)^2 \left| \int e^{-i\mathbf{k}'.\mathbf{r}} V(\mathbf{r}) e^{i\mathbf{k}.\mathbf{r}} d\mathbf{r} \right|^2 \tag{1.62}$$

where m_n is the mass of the neutron. The differential scattering cross section gives the number of scattered neutrons per unit time, normalised with respect to the incident flux. As the neutrons are undergoing elastic scattering, no change to the system occurs and we consider only the change to the neutron wavefunction.

For N scattering centres, placed at positions $\mathbf{R}_i$ and each with the same potential, we write

$$V(r) = \sum_i^N V(\mathbf{r} - \mathbf{R}_i). \tag{1.63}$$

The differential cross section can now be written as

$$\frac{d\sigma}{d\Omega} = \left(\frac{m_n}{2\pi\hbar^2}\right)^2 \left| \int V(\mathbf{r}') e^{i\mathbf{q}.\mathbf{r}} d\mathbf{r} \sum_i^N e^{i\mathbf{q}.\mathbf{R}_i} \right|^2 \tag{1.64}$$

where $\mathbf{q} = \mathbf{k} - \mathbf{k}'$, the scattering vector and $\mathbf{r}' = \mathbf{r} - \mathbf{R}_i$. This is constructed from two parts, a structure factor

$$S(\mathbf{q}) = \left| \sum_i^N e^{i\mathbf{q}.\mathbf{R}_i} \right| \tag{1.65}$$

which describes the ordering of the lattice, and a form factor

$$F(\mathbf{q}) = \int V(\mathbf{r}') e^{i\mathbf{q}.\mathbf{r}} \tag{1.66}$$

which is the Fourier transform of a single scattering potential. For parallel fields there is no spin-flip of the neutron, so the spin component of the neutron wavefunction need not be considered. The scattering potential is then given by

$$V(\mathbf{r}) = \mu_{\mathbf{n}} \gamma B(\mathbf{r}) \tag{1.67}$$

where $\gamma = 1.9$, the neutron gyromagnetic ratio and $B(\mathbf{r})$ describes the local field as a function of the radial distance $\mathbf{r}$ from the potential centre. The differential scattering cross section for this is therefore

$$\frac{d\sigma}{d\Omega} = \left(\frac{m_n}{2\pi\hbar^2}\right)^2 \gamma^2 \mu_N^2 \frac{1}{\Phi_0} \left| \int B(r) e^{i\mathbf{q}.\mathbf{r}} dr \right|^2. \tag{1.68}$$

Assuming a VL structure where the vortices are constructed of rigid ideal rods, the structure factor exhibits δ functions at the flux line positions, such that

$$S(\mathbf{q}) \propto \sum \delta(\mathbf{q} - \mathbf{G}) \tag{1.69}$$

which enforces the Bragg condition that scattering only occurs when the scattering vector $\mathbf{q}$ is equal to the reciprocal lattice vector $\mathbf{G}$. We now express the form factor as $F_{\mathbf{G}}$, and accounting for the form of the structure factor for a large sample the differential cross section now becomes

$$\frac{d\sigma}{d\Omega}(\mathbf{q}) = \left(\frac{\gamma}{4}\right)^2 \sum_{\mathbf{G}} |F_{\mathbf{G}}| \delta(\mathbf{q} - \mathbf{G}). \tag{1.70}$$

In SANS, the rigid delta functions expressed above are spread out over a range of conditions due to resolution effects and imperfections in the VL such that the system exhibits a spread in the Bragg condition. Instead of measuring a differential scattering cross section, we measure the integrated intensity of the diffracted neutrons as the sample is rotated through the angular range that fulfils this angular range. The relation between the integrated intensity, $I_{\mathbf{h}\ \mathbf{k}}$, and the form factor, $F_{\mathbf{G}}$ is given by Christen *et al* (Christen et al., 1977)

$$I_{\mathbf{h}\ \mathbf{k}} = 2\pi\phi V \left(\frac{\mu}{4}\right)^2 \frac{\lambda_n^2}{\Phi_0 G_{\mathbf{h}\ \mathbf{k}}} |F_{\mathbf{G}}|^2. \tag{1.71}$$

Here, V is the sample volume, ϕ is the neutron flux, λ_n is the neutron wavefunction and Φ_0 is the flux quantum. This form factor, $F_{\mathbf{G}}$, is the $B_{\mathbf{G}}$ given in equation 1.28, and allows us to relate our observations of the magnetic scattering potential experienced by the neutrons to superconducting properties of the system.

1.12 The Ewald Sphere

The Ewald sphere is a useful geometric interpretation of elastic scattering, which can illustrate some important consequences of the methods employed in SANS. It is defined in reciprocal space as the sphere on which all possible incoming and elastically scattered wave vectors ($\mathbf{k}$ and $\mathbf{k}\prime$) lie. This is illustrated in figure 1.5. In elastic scattering, incoming and outgoing wave vectors have the same length, thus defining the surface on which they can lie as a sphere. The Bragg condition is only satisfied where the sphere intersects the reciprocal lattice, which for a 2D system like a VL is ideally a plane. In the situation where the incoming wave vector is perpendicular to the plane of the reciprocal lattice, the only intersection point is in the centre of the lattice, and so no scattering is observed. As the reciprocal lattice plane is rotated, it intersects the Ewald sphere in an expanding circle, from which scattering can occur, as observed in figure 1.5. As all points on the circle satisfy the Bragg condition simultaneously, multiple diffraction spots can occur at the same rocking angle, a tactic often employed in SANS.

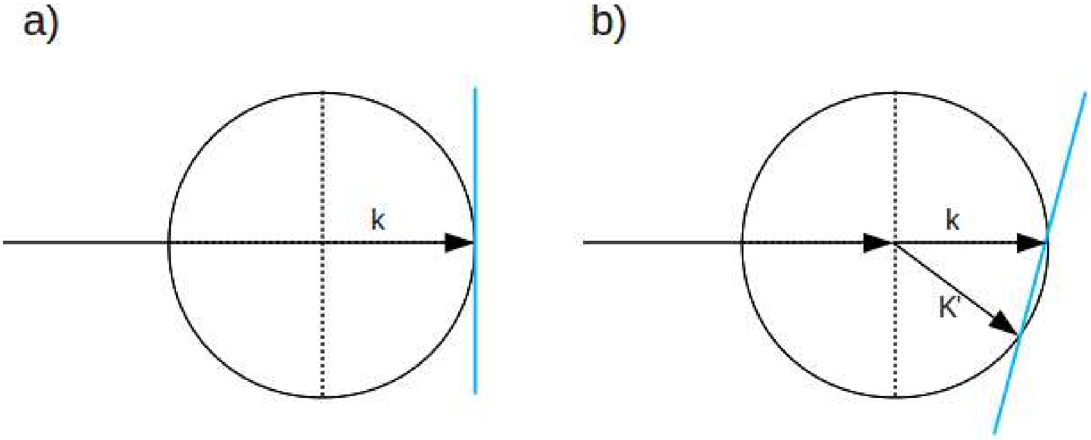

Figure 1.5: a) With the reciprocal lattice plane perpendicular to the incoming beam, the Ewald sphere intersects only with the origin of the reciprocal lattice plane. b) As the reciprocal lattice plane is rotated, the Ewald sphere intersects the reciprocal lattice to satisfy the Bragg condition for the scattering vector $\mathbf{k}'$.

The spread in Bragg conditions discussed in the previous section results in the Ewald sphere cutting a range of Bragg conditions rather than a single point on the reciprocal lattice. This leads to a SANS instrument having a ‘resolution’ which, in the case of a flux lattice experiment, is a result of both instrumental conditions and imperfections in the vortex lattice, which will be discussed in a later section.

1.13 Instrumental

Small Angle Neutron Scattering (SANS) is a technique employed in a multitude of scientific fields, ranging from biological studies in the area of soft condensed matter to the imaging of flux lattices in superconductors as utilised here. As discussed in section 1.11, neutrons passing through a flux lattice can undergo Bragg scattering, and so by applying a field to a type II superconductor in the mixed state and rotating (or rocking) the sample (with field) through the varying Bragg conditions from the multitude of flux line planes present in the sample, it is possible to build up a picture of the flux lattice. The resultant image is a Fourier transform of the real space object. In the case of the image of a flux lattice, the real space lattice may be envisaged simply by rotating the image through 90°.

In order to perform SANS, a neutron source is required, either a nuclear reactor such as the one at the Institut Laue-Langevin (ILL), or a spallation source as used in the Paul Scherrer Institute (PSI). Sources such as these produce fast, or hot, neutrons which are then moderated to produce cold neutrons. A schematic diagram of a small angle scattering instrument is shown in fig. 1.6. Neutron guides transport neutrons from the cold source to the instrument, passing through a velocity selector which passes only neutrons of the required wavelength, to within an accuracy of $\approx 10\%$. After velocity selection, the neutrons must pass through a monitor detector. This is a very low efficiency detector, which detects on the order of 10^{-6} of the neutrons which pass through it. This allows for normalisation of the final signal to a known quantity which is directly proportional to the number of neutrons incident on the sample. The beam is then collimated, to reduce beam divergence, before passing through the sample, after which the diffracted beam is incident on a position sensitive detector. The distance of a SANS detector from the sample is usually variable, as a variety of diffraction angles is experienced with SANS which would make a stationary detector infeasible. The remaining un-diffracted beam is absorbed by a beam stop placed before the detector, which is usually required to prevent detector overload. Beam size at the sample is limited by an aperture, to prevent illumination of unwanted material. All materials that the neutrons pass through, including any air present

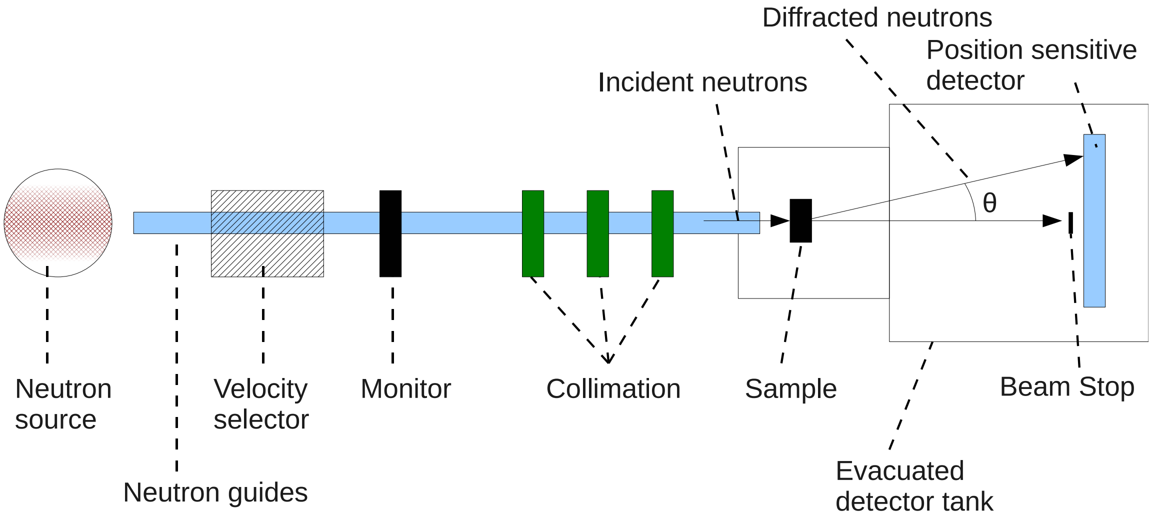

Figure 1.6: Schematic of a SANS instrument. Velocity selected neutrons are sent through a series of collimation apertures to limit divergence, then are diffracted from the sample before being incident on a detector.

in the beam path, cause unwanted scattering, which appears as background signal on the detector. Furthermore, material illuminated by neutrons may become radioactive, usually for short periods, which is an unwanted side effect of neutron experiments, and shielding equipment minimises this. Background signal must be measured, in the absence of any experimental signal, so it can be subtracted from these measurements to leave only the scattering as a result of the flux lattice. Background scattering is often angle dependent, and can also change if objects in the beam path move as a result of magnetic fields and temperature changes, so it is necessary to take foreground and background measurements under as similar conditions as possible. Since either temperature or applied field must be changed between foreground and background measurements, it is advisable to investigate which one produces the least shift. Experimental apparatus in the cryostat is also prone to contraction dependent on cryogen levels, which naturally change over time due to boil off, which must be taken into consideration.

1.14 Resolution of the instrument

As previously stated, the velocity selector provides a spread of neutron wavelengths. Since the velocity selector works by removing neutrons of unwanted wavelength, the spread is necessary as a monochromatic beam produced by this technique would contain no neutrons. The neutron beam is collimated to limit the range of input angles of neutrons incident on the sample, which may be small but remains non-zero. In addition to this, no flux lattice will ever be perfectly formed, and the defects will lead to both a variety of inter-vortex spacings, $\mathbf{D}$, and vortices meandering along their length, or a 'mosaic spread'. Thus, in order to find the total diffracted intensity of a spot one must rock the sample through the full range of angles at which it appears. The resultant "rocking curve" will be a convolution of the resolution effects of both the beam and the sample (Cubitt et al., 1992). This results in a spread of intensity which must be integrated over, rather than all the Bragg scattering occurring at a single angle. Whilst it is perfectly possible to analyse this data by using the integrated intensity across the rocking curve, it is worth noting that the limiting factors which govern the shape of this curve can change with the experimental conditions, and the width of the rocking curve and size of Bragg reflections can provide important information about the behaviour of the VL under investigation. To this end, Cubitt et al (Cubitt et al., 1992) derived expressions for the rocking curve width and spread in Bragg reflection from an imperfect lattice. The angular contributions are illustrated in fig. 1.7, where the line AA$'$ represents the perfect lattice, with a perfectly collimated beam diffracting at a Bragg angle θ. However, the imperfect collimation results in an input ray coming in at an angle ϕ_1 to the ideal, which encounters a mosaic block of the imperfect lattice at an angle η resulting in overall diffraction of the ray at an angle ϕ_2 to the ideal. Further, the spread in neutron wavelength, $\Delta\lambda/\lambda$, and the spread in inter-vortex spacing, $\Delta\mathbf{D}/\mathbf{D}$, both contribute to a spread in the diffraction angle θ, and the effects of these are indistinguishable.

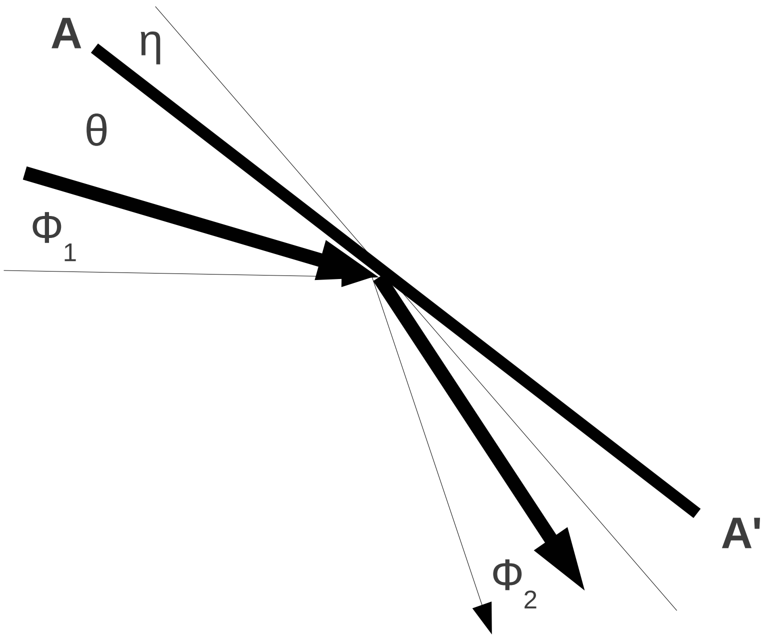

Figure 1.7: Figure describing the effect of instrument conditions and vortex lattice perfection on diffraction. The line AA′ represents a perfect lattice with the bold line at an angle theta demonstrating diffraction from a perfectly collimated beam. However, in reality the collimation of the beam may contribute an angle ϕ_1 to the diffraction added to an imperfect lattice described by the angle η results in diffraction at an angle ϕ_2.

Cubitt *et al* expressed these contributions to the spread in diffraction angle as Gaussian functions, and for the full width at half maximum (FWHM) of a rocking curve, W_w, they find

$$W_w^2 \cos^2(\alpha) = a^2 + b^2 + c^2 \tag{1.72}$$

where a is the FWHM of the direct beam collimation angle, b is the FWHM of mosaic spread due to vortices meandering along their length and $cos(\alpha)$ is the Lorentz factor for a Bragg reflection at an angle to the direction of rocking. The value c is given by the expression

$$\left(\frac{c}{\theta}\right)^2 = \left(\frac{\Delta\lambda}{\lambda}\right)^2 + \left(\frac{\Delta D}{D}\right)^2 \tag{1.73}$$

where θ is the Bragg angle, $\Delta\lambda/\lambda$ is the spread in wavelength of the neutrons and $\Delta D/D$

is the spread in vortex spacing. These two are equivalent in effect on Bragg diffraction from the lattice, and so are inseparable in the overall expression for the FWHM of the rocking curve. By assuming a perfect lattice, such that b and $\Delta D/D$ drop out, the resolution width of the instrument can be calculated, from which is is possible by comparison to judge the perfection of the lattice. Whilst it is not possible to gain quantitative information directly due to inseparability of spread in neutron wavelength and spread in vortex spacing, qualitative comparison as a function of temperature and field provides useful information about the evolution of the lattice under changing conditions.

1.15 Cryostats

To achieve the kinds of temperatures required for superconductivity to exist, the sample is situated within a cryostat - a device designed to maintain the necessary temperature within the Kelvin or even milli-Kelvin range. For neutron scattering off flux lattices, accessibility to the neutron beam and an applied field are also required. Both external normal state magnets and internal superconducting magnets can be used to provide the field, with the former normally consigned to low field experiments due to power and heat dissipation limitations. In either case, it is necessary to keep the material in the path of the neutron beam to a minimum, to avoid excess absorption and scattering, both of which have the potential to obscure the experimental signal from the sample. As such, equipment such as magnets are always kept out of the beam, and material in the path of the neutron beam is usually kept as high purity aluminium, or in the case of specific cryostat 'windows', sapphire and silicon.

Keeping the sample at low temperatures in a background environment of 300 K is usually achieved by the use of cryogens in conjunction with vacuum insulation. Whilst 'cryogen free' systems, which operate off a pumped thermodynamic cycle to provide cooling power, are available for research, only cryogen filled systems were used in the experiments presented here. Often, several cryogen stages will be used in the cooling process. An outer layer cooled by liquid nitrogen may be used to shield the liquid helium cooled apparatus from room temperature. The liquid helium stage will itself be used to shield the sample environment. Pressure release valves are necessary when dealing with enclosed cryogen baths in case the gas return systems fail. The cryostat will contain finer temperature control methods such as a 1 K pot for experiments below 4 K, or a dilution refrigerator stage to reach the milli-Kelvin region. A schematic of a basic overview of a cryostat with a 1 K pot and heat exchanger setup is shown in figure 1.8. It is not always convenient to try to access the Kelvin range whilst running a dilution refrigerator, and so separate set-ups may be required if both regimes are to be investigated. Samples are placed on a sample holder, which takes the form either of a sample stick (see fig. 1.8) or horizontally removable holder, depending on the cryostat geometry.

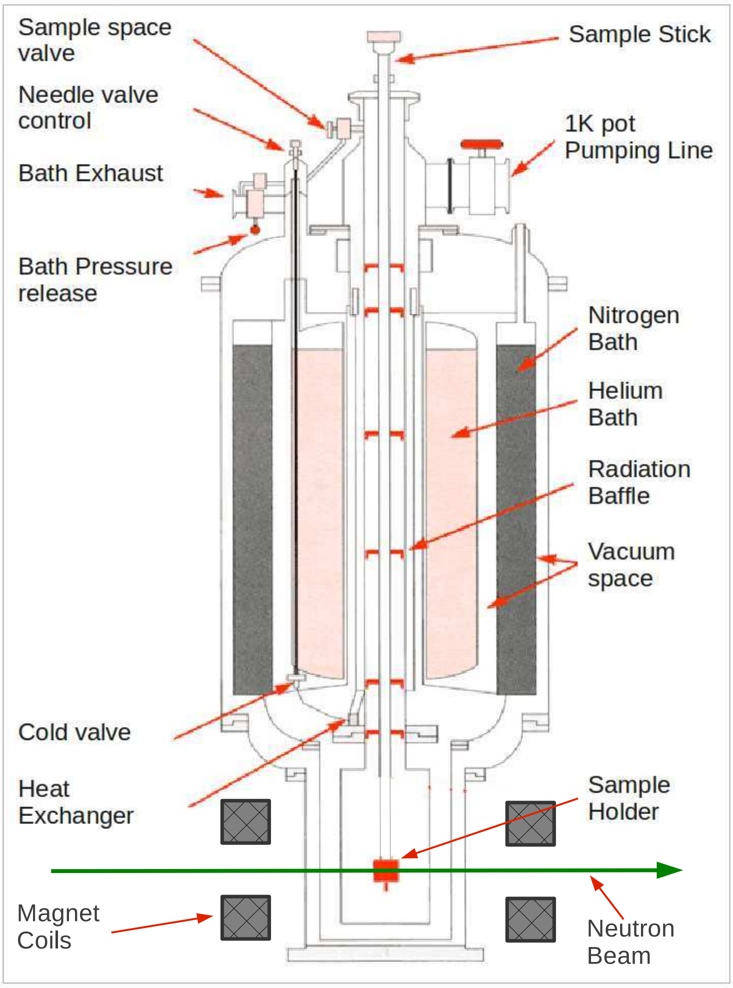

Figure 1.8: Figure showing a basic schematic of a cryostat, based on a design from the AS Scientific Products online catalogue (Scientific). Features common to most cryostats are labelled, although precise geometry will vary depending on design. Since this cryostat does not include an internal magnet, an external one is shown.

The cryostat will either contain a superconducting magnet of its own, or if not may utilise an external magnet. To produce a uniform field across the sample volume, either a split pair of coils is used or a solenoid geometry, with the sample being placed in the centre of the magnet in either case. The former geometry usually possesses the advantage of a greater angular range of access, and will usually be loaded with the sample stick set-up shown in figure 1.8 which is both easy to use and has a rapid turnaround time in the event of sample change. Using a solenoid magnet, however, gives access to a higher field maximum. Both geometries were used in the experiments presented in this thesis. The full cryostat and magnet system will be placed on a goniometer and rotation stage, in order to be able to rotate the flux lattice being investigated through the required Bragg angles.

Temperature control in the sample space is usually done by providing a constant source of cooling power and then using heating systems to give precise temperature control. Whilst cooling below the required temperature and then heating the sample may seem counter productive when we already exist in a ready made background of ∼300 K, temperature control on a heated system with feedback provided by a local thermometer is far easier, more precise and more successful than trying to control the cooling power to produce the required temperature. For ^{4}He cryostats, the cooling power in the sample space is provided by a 1 K pot, which is part of the heat exchanger seen in fig 1.8, which is simply a space for small amounts of liquid helium to evaporate with the assistance of a pumping system in order to produce cooling power. Typically, a constant pumping pressure is provided by an external unit (VTI pump in figure 1.8), and cooling power is regulated by constraining the rate at which liquid helium is brought in to the 1 K pot through a needle valve attached to the main helium bath. Whilst, as its name suggests, this type of system should be able to provide temperatures as low as 1 K it is common for the minimum sample temperature available to this kind of set-up to be between 1.5 and 2 K. When investigating superconductors such as the high T_c cuprates, where 2 K is a small fraction of their critical temperature, this kind of system is an ideal balance of ease of use compared to operating difficulty since lower temperatures are not required to access new physics. If investigating low T_c superconductors, however, 2 K may be a noticeable fraction of T_c. Here, lower temperatures are required and this is usually achieved using a dilution refrigerator.

The dilution refrigerator was initially proposed by Heinz London in 1951 (London, 1951), although not successfully produced until 1964 (Das et al., 1964). It provides cooling power through the latent heat of mixing of two isotopes of helium: ^{4}He and ^{3}He. When a mixture of these two isotopes is cooled below ~870 mK, it undergoes a spontaneous phase separation into a helium 3 rich phase and a ^{3}He reduced phase, known as the concentrated and dilute phases respectively. At very low temperatures, the concentrated phase is almost pure ^{3}He, whilst the the dilute phase resides at around 6.6% ^{3}He and 93.4 % ^{4}He. It is the ^{3}He that is circulated around the system to provide cooling power. A schematic diagram of this is shown in figure 1.9. ^{3}He enters the fridge at around a few hundred millibar, passing through several cooling stages until reaching a stage coupled with a ^{4}He 1 K pot, which liquefies the ^{3}He. The liquid helium is drawn though a high flow impedance capillary system, past a heat exchanger coupled to the still cooling it to around 500 - 700 mK. A secondary capillary system with a lower flow impedance then draws the liquid helium 3 into the mixing chamber, passing through one side of a counterflow cooling system with the ^{3}He leaving the mixing chamber providing the cooling power as it passes through the other side of the counterflow. Within the mixing chamber lie the phase separated dilute and concentrated phase. ^{3}He is drawn across this phase boundary and diluted in the dilute phase, which is an endothermic process and thus provides the cooling power of a dilution fridge. The ^{3}He returns to the beginning of the process by passing through the counterflow heat exchanger in the dilute phase into the still, and then back out as a gas. The still is maintained at around 500-700 mK by use of a still heater, where ^{3}He has a much higher vapour pressure than ^{4}He, and as such the low pressure gas in the still, which is pumped back to the return of the cycle, is almost pure ^{3}He. The preferential removal of ^{3}He lowers the concentration and creates an osmotic pressure in the mixing chamber, which is what draws the ^{3}He from the concentrated to dilute phases.

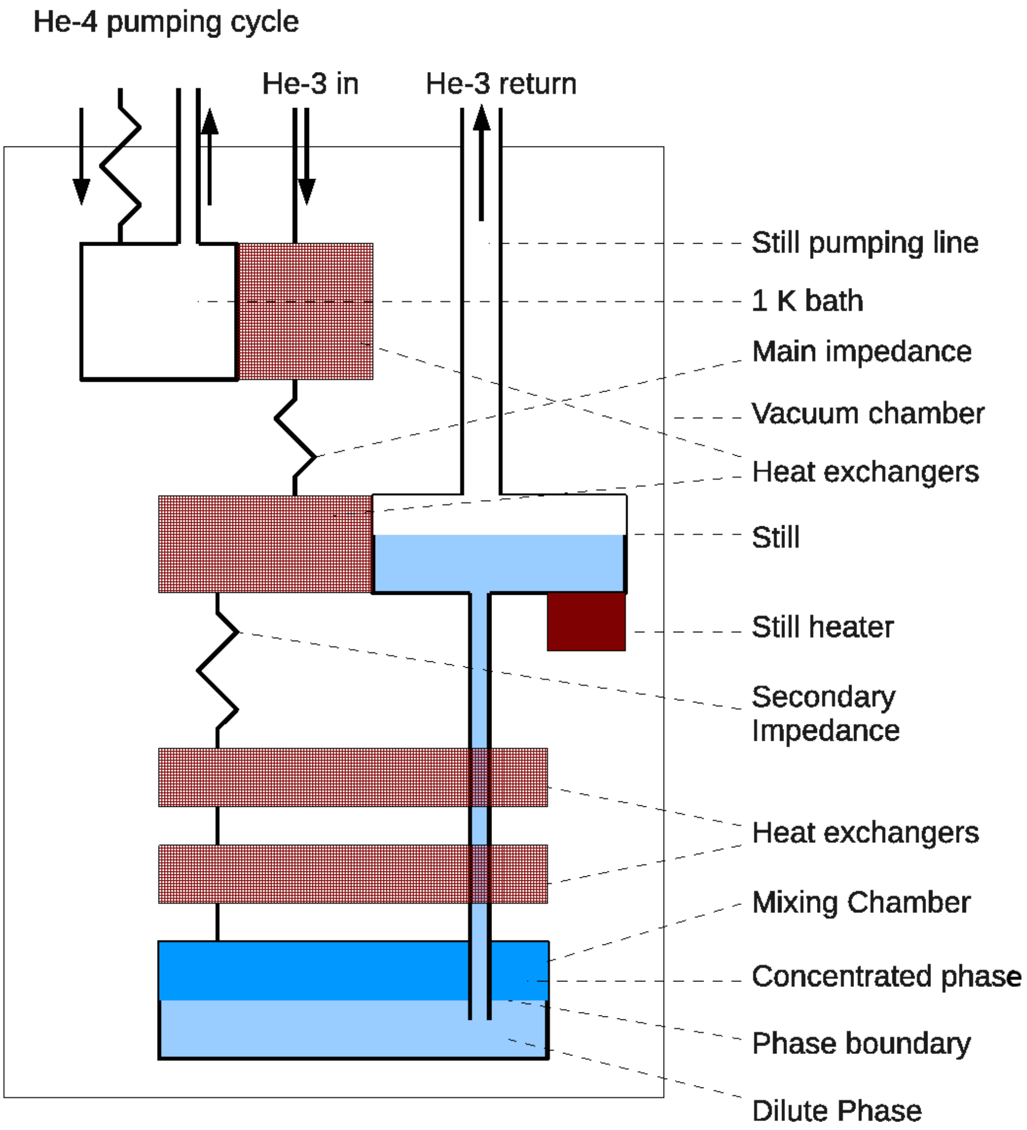

Figure 1.9: Figure showing a basic schematic of a dilution refrigerator. The diagram shows the area contained within the inner vacuum chamber, around which will exist the standard cryostat set-up. The inner vacuum chamber is thermally connected to a low temperature reservoir, such as a ^{4}He bath, to provide thermal radiation shielding against the warmer background of the cryostat.

1.16 'Grasp' Data Analysis

The majority of the data published in this thesis, with the exception of some sample characterisation measurements, are SANS measurements. For monochromatic SANS data of the type in these experiments, data is taken by counting the number of incident neutrons at their respective pixel on the position sensitive detector for a specified time or monitor value. The resultant data is a two dimensional array with a single entry in the array corresponding to a single pixel on the detector. In addition to this, the data file also records a variety of instrument conditions such as neutron wavelength and sample temperature. In order to analyse the data, a program called GRASP has been used. GRASP is a Matlab script application written by Charles Dewhurst of the ILL, and provides a graphical interface for the handling, analysis and reduction of SANS data from a variety of neutron sources (Dewhurst).

CHAPTER 2

THE PNICTIDES

2.1 Literature Review

Superconductivity was discovered in the iron-based superconductor LaFePO in 2006 (Kamihara et al., 2006) at 4 K, and became known as a class of superconductors with the discovery of La($O_{1-x}F_x$)FeAs (Kamihara et al., 2008), with a critical temperature of 26 K. Soon afterwards, the pnictides, so called because of the common unit of an iron-pnictogen layer, RFeAs($O_{1-x}F_x$) (R = Ce, Pr, Sm, Nd etc.) were found to have critical temperatures in the region of 50 K (X. H. Chen and Fang, 2008) (Xu et al., 2008), thus making the pnictide superconductors second only to the cuprates in terms of T_c. This, coupled with the presence of superconductivity in a system capable of possessing magnetic order has made the pnictide superconductors of great interest to the condensed matter community. Since the structure and behaviour of the vortex lattice is governed by the electronic and physical structure of the crystal lattice, SANS investigations into the pnictides can provide an important contribution towards understanding these materials and the superconductivity they exhibit.

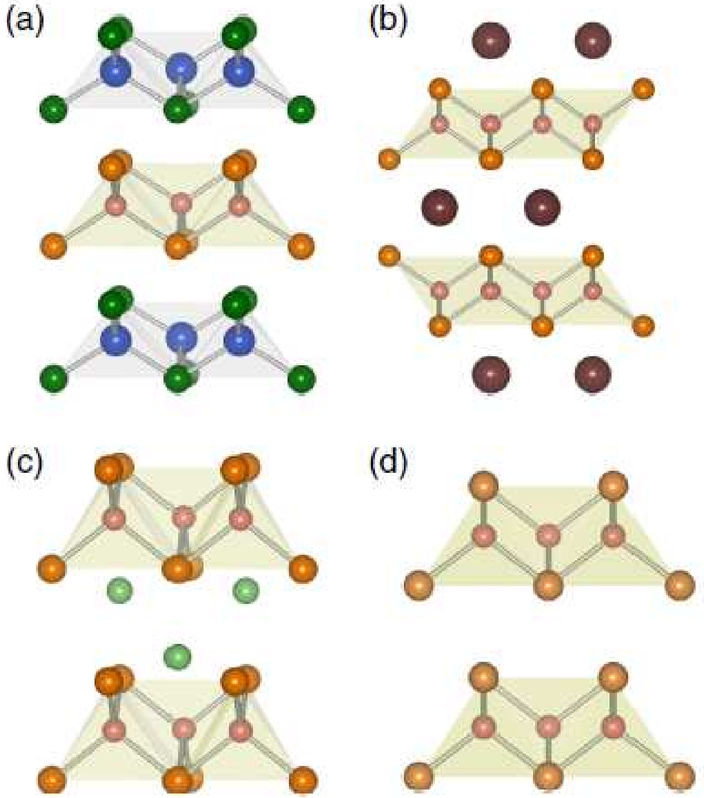

Figure 2.1: Crystal structures of four groups of iron-based superconductors a) LaFeAsO "1111", b) $BaFe_2As_2$ "122", c) LiFeAs "111" and d) FeSe "11". Figure from Ishida *et al* (Ishida et al., 2009).

Figure 2.1, replicated here from work by Ishida *et al* (Ishida et al., 2009) presents four structure groups prevalent in the iron-based superconductors, with example chemical compositions and the various numerical structure labels included in the caption. It is the (122) structure group which is of specific interest in this thesis, as the pnictides under investigation are KFe_2As_2 and $BaFe_2(As_xP_{1-x})_2$, both 122 materials. This structure has been seen in previous superconductors, such as the heavy fermion compounds since their discovery with $CeCu_2Si_2$ (Steglich et al., 1979).

The parent compound for both pnictides studied in this thesis is the antiferromagnet $BaFe_2As_2$. For an AFe_2As_2 system, where the A = Ba,Sr or Ca, the system can become superconducting through electron doping of the Fe site with cobalt or nickel (Sefat et al., 2008) (Wadati et al., 2010), or through hole doping of the A site with a monovalent B^+

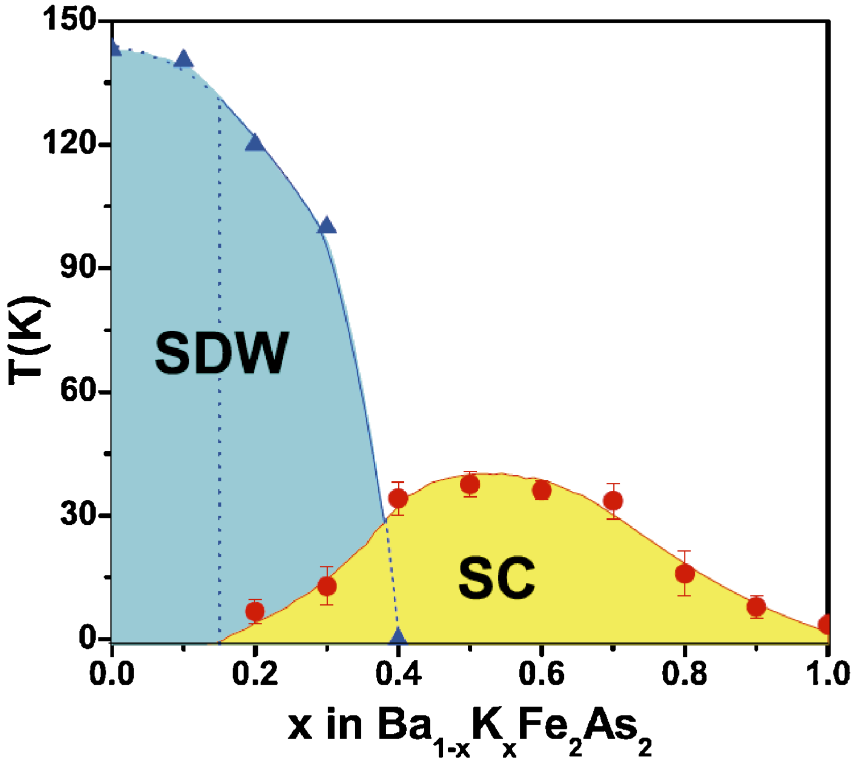

Figure 2.2: The temperature - doping phase diagram for pnictide systems, with superconducting (SC) and antiferromagnetic (SDW) states shown. Picture reprinted from work by Chen *et al* (Chen, 2009).

atom, where B = K, Cs, Na - a group 1 metal (Rotter et al., 2008; Sasmal et al., 2008). The temperature-doping phase diagram of this system can be seen in figure 2.2. Here, the existence of a superconducting phase is shown in conjunction with an antiferromagnetic phase, labelled as spin density wave or SDW. A perhaps surprising phenomenon in the pnictides, however, is the emergence of superconductivity out of magnetic order as a result of isovalent doping on the arsenic site, which is the case for $BaFe_2(As_xP_{1-x})_2$. Possessing a similar phase diagram to fig. 2.2, a spin density wave AFM phase gives way to a superconducting state with increasing doping.

Understanding the electronic structure of the pnictides provides the basis for explaining superconductivity in these materials. Density functional theory (DFT) calculations have provided a good starting point for both theoretical models and contextualising experimental results. The common features in pnictides are two or more hole-like Fermi sheets around the centre of the Brillouin zone and two electron-like sheets at the corners (Mazin and Schmalian, 2009), separated by a (π, π) wavevector. Fermi surfaces of the un-doped 1111 compounds tend to be quasi 2D, with the 122 compound sheets possessing more 3D character, which may explain why the magnetism in 122 systems tends to be stronger than its 1111 counterparts due to interlayer coupling. Upon doping, however, the Fermi surfaces tend to lose their dimensionality and become quasi 2D, suggesting that long range magnetic order is destroyed by a reduction in interlayer coupling when charge carriers are added to the system. Quantum oscillation measurements (Sebastian et al., 2008; Analytis et al., 2009) have shown that un-doped 122 systems are Fermi liquids, although a sizeable region of their Fermi surface disappears upon gaining of magnetic order due to gap formation. The frequencies of the magneto-oscillations point to an ordered magnetic state having small Fermi pockets, which is consistent with the formation of a spin density wave (Mazin and Schmalian, 2009). The parent compound for pnictides has antiferromagnetic order, with Fe spins being parallel and antiparallel in the orthogonal directions of the Fe-As plane. Neutron scattering has given an ordered iron moment of $0.9\mu_B$ for $BaFe_2As_2$ (Huang et al., 2008). This AFM state is known to be metallic, with a noticeable Drude conductivity (Hu et al., 2008), and shows Fermi surfaces appropriate for a partially-gapped antiferromagnet (Hsieh et al.).

The pairing interaction and gap structure in the pnictides is still under debate, although the predominant explanation is for the superconducting interaction to be magnetic in nature (Mazin et al., 2008), and that in optimally-doped materials this leads to a repulsive interaction between holes on Fermi surface sheets at the centre of the Brillouin zone and electrons on sheets at the corners. The pairing interaction here relies on the idea that even if the excitation under exchange produces a repulsive interaction, that interaction can be attractive if the exchange is taken between parts of the Fermi surface possessing opposite signs of the order parameter. This can be seen in fig. 2.3, where $\Delta_{\mathbf{k}} = -\Delta_{\mathbf{k}+\mathbf{Q}}$, where a repulsive interaction with wavevector $\mathbf{Q}$ is attractive due to sign reversal of the gap. With the Fermi surfaces under question separated by a (π, π) wavevector, spin fluc-

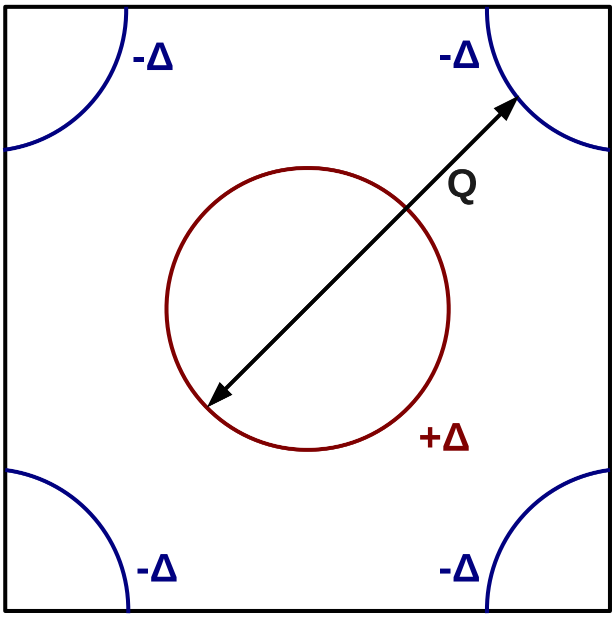

Figure 2.3: Simplified diagram of the proposed Brillouin zone for the pnictides undergoing $s_{\pm}$ pairing. The hole sheet is shone in red at the centre of the zone with the gap $+\Delta$ and the electron sheets are shown in blue at the corners of the zone with the gap $-\Delta$. The proposed interaction for $s_{\pm}$ pairing is shown by the vector Q, with the spin density wave vector spanning the hole and electron pockets.

tuations were proposed as the exchange excitation (Mazin et al., 2008), and the resulting angular momentum of $L = 0$ and opposing gap signs this has led to the name $s_{\pm}$ for this pairing state. Other pairing states have been proposed, such as the s_{++} state proposed by Kontani *et al* (Kontani and Onari, 2010) and Yanagi *et al* (Yanagi et al., 2010), which is mediated by orbital fluctuations. Theoretical predictions by Fernandes *et al* (Fernandes and Schmalian, 2010) have argued against this, since their model for magnetism and superconductivity, where the electrons leading to superconductivity are also those whose spins order, gives a sign changing $s_{\pm}$ state.

Phonon-mediated superconductivity was ruled out at an early stage as it is too weak to account for the critical temperatures of most pnictides (Osborn et al., 2009). However, an isotope effect has been seen in some materials. Liu *et al* (Liu R.H., 2009) noted an isotope effect in $SmFeAsO_{0.85}F_{0.15}$ and $Ba_{0.6}K_{0.4}Fe_2As2$, but only for isotope substitutions of iron. This suggests that whilst phonons may have an influence on superconductivity in the pnictides, it may only be by affecting the magnetic fluctuations through a magnetoelastic effect. This is not certain, however, with Shirage *et al* reporting both an absence of and an inverse isotope effect in their experiments (Shirage et al., 2010, 2009).

The proximity, and perhaps co-existence, of magnetism and superconductivity in the pnictides, as well as strong evidence against conventional pairing mechanisms has led to most proposals for the superconducting interaction to be magnetic in nature, with the predominant explanation that a repulsive interaction can be attractive under a sign-changing gap being necessary for these to work. Furthermore, inelastic neutron scattering has shown a link between the onset of superconductivity and a spin fluctuation resonance peak (Christainson A.D., 2008). This, as well as a vast array of other evidence, has led the $s_{\pm}$ spin fluctuation mediated superconductivity to become the dominant explanation for superconductivity in the pnictides.

Previous to the work done on KFe_2As_2 and $BaFe_2(As_xP_{1-x})_2$ detailed in this chapter, work on pnictides through SANS had produced limited results at best. The necessity for fractional doping parameters in order to achieve superconductivity in most pnictides resulted in plenty of structural defects and thus vortex pinning sites in the samples. This led to disorder in the vortex lattice, resulting in ring-like diffraction patterns with wide rocking curves that limited the information which could be extracted from these results. An example, taken from the work by Inosov *et al* (Inosov et al., 2010) on LiFeAs is shown in fig. 2.4 - the author participated in this work, but it will not be detailed in this thesis.

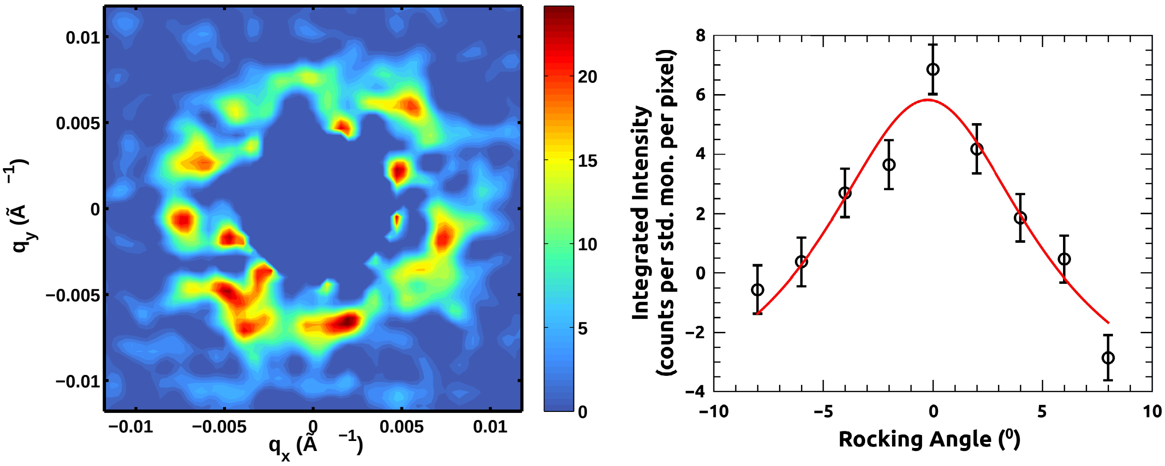

Figure 2.4: Left: Diffraction pattern from the vortex lattice of LiFeAs at 0.25 T, showing a strongly disordered lattice. Right: Rocking curve at the same field, showing a wide FWHM indicative of vortex pinning leading to deviations along the length of the vortices. Both images are from data published by Inosov *et al* (Inosov et al., 2010).

2.2 KFe_2As_2

For the investigation presented here, our crystals are fully over-doped KFe_2As_2, here denoted KFA, from the $(Ba_{1-x}K_x)Fe_2As_2$ system with a doping parameter, x, of 1. As can be seen in figure 2.2, this somewhat limits the critical temperature and field of our system. However, doped pnictides have shown strong vortex pinning, probably as a result of nanoscale inhomogeneities in the crystal structure which have arisen as a result of doping. It was hoped that using stoichiometric crystals would avoid this pinning seen previously in the pnictides, providing clear SANS results.

As a member of the 122 family of pnictides KFA possess tetragonal symmetry, as seen in fig. 2.1 (b), with the crystallographic **a** and **b** axes being equivalent directions in the iron-pnictogen plane running parallel to the nearest neighbour iron-iron directions, and the **c** direction running perpendicular to this plane. Barium is a group-II metal possessing two electrons in its outer 6s shell, whilst Potassium is a group-I metal with one electron in its outer 4s shell. As previously stated, this results in hole doping with one additional hole added to the system per substitution. The Fermi surface shown in figure 2.3 posses hole sheets in the centre of the Brillouin zone and electron sheets at the corners. Since this is for the parent compound $BaFe_2As_2$, the volume of the hole and electron sections will change with doping as we move towards the fully over-doped system, although the basic structure of the Fermi surface, where the center is populated by hole sheets and the corners by electron sheets, remains similar with moderate doping (Singh, 2008). However, for situations where x in $(Ba_{1-x}K_x)Fe_2As_2$ is equal to 1, it has been seen in Angle Resolved Photoemission Spectroscopy (ARPES) (Sato et al., 2009) and de Haas-van Alphen effect (dHvA) (Terashima et al., 2010) measurements that *all* Fermi surface sheets, including those at the corners, are hole sheets. From the single valence of potassium, we can deduce that a single hole is contributed to the system from a KFe_2As_2 unit.

2.2.1 KFe_2As_2 sample

Our sample was formed of a poly-crystal mosaic of approximately 100 mg for the experiments at ILL, and of 250 mg for those at PSI. Single crystals of KFe_2As_2 were grown from a precursor of FeAs, heated to 900 C in an evacuated atmosphere for $\sim$ 10 hours and then mixed with K and As in the ratio K:As:FeAs $= 3 : 2 : 2$. The mixture was maintained at 900 C for a further 10h in an Al_20_3 crucible inside a sealed stainless steel tube, after which it was cooled to 650 C at a rate of 1 Khr^{-1} and then quenched (Kawano-Furukawa et al., 2010). Each single crystal had a typical size of around $7 \times 7 \times 0.5$ mm^3 and was aligned with the c axis perpendicular to the mounting plate with the [100] direction in the horizontal plane of the SANS configuration. The sample was found to have a T_c of 3.6 K with a transition width of 0.2 K from 10-90%, and a residual resistance ratio of $\sim$ 400. Large hysteresis was seen in the magnetisation data in fig. 2.5, showing that vortex pinning is active at the low field of 1 mT despite crystal stoichiometry. The single crystals of KFA were mounted on aluminium plates using hydrogen free Cytop glue, with the **c**-axis perpendicular to the surface of the plate. Crystals were co-aligned such that one of the tetragonal [100] axes was horizontal, and an example of typical sample plates can be seen in figure 2.6. The cryostats used, as well as the collimation of the neutron beam, provided a physical limitation on the width of the sample plates, so where necessary

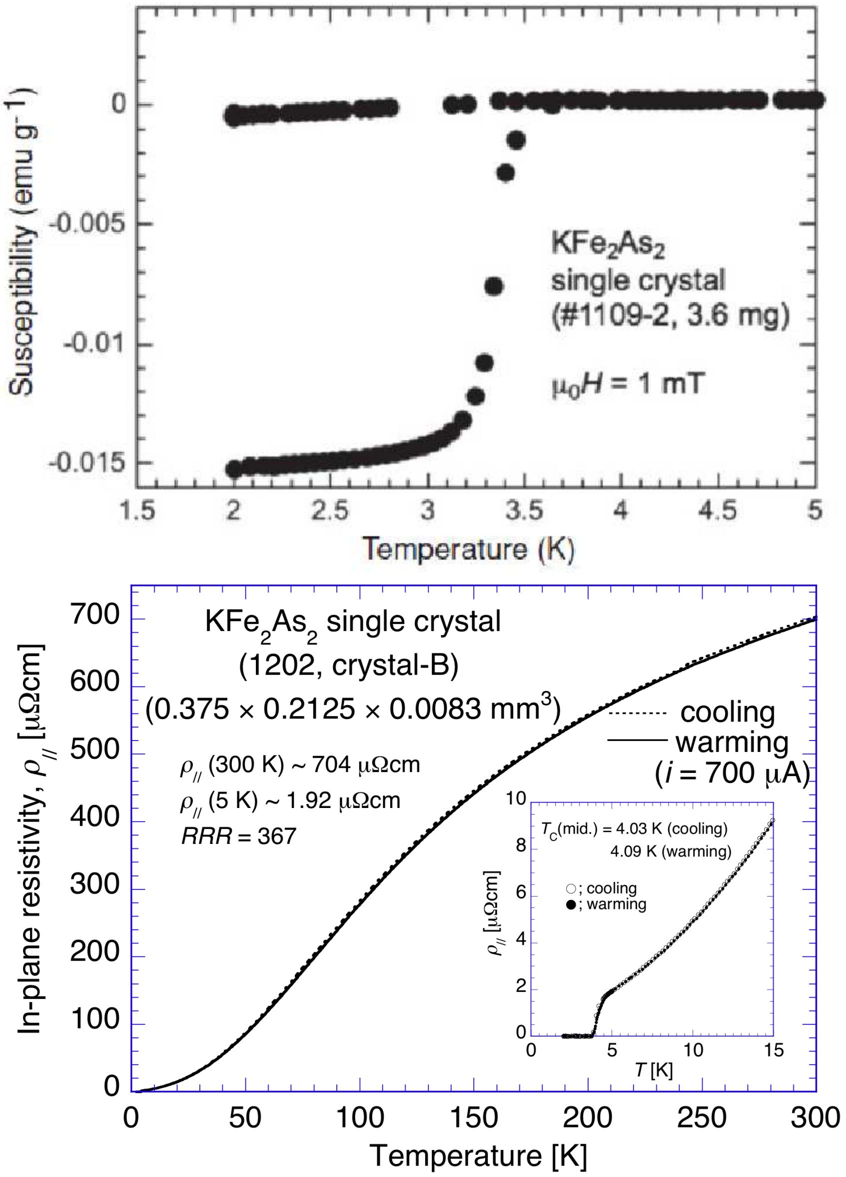

Figure 2.5: Sample characterisation measurements for KFA crystals. Top: Magnetisation data taken in an applied field of 1 mT. Data shows a T_c of 3.6 K with a 10-90 % transition width of 0.2 K. Bottom: In-plane resistivity measurements, showing a residual resistivity ratio of $\sim$ 400. Inset: enlarged region of the resistivity-temperature graph showing the area around the superconducting transition. Figures reproduced from work by Furukawa *et al* (Kawano-Furukawa et al., 2011).

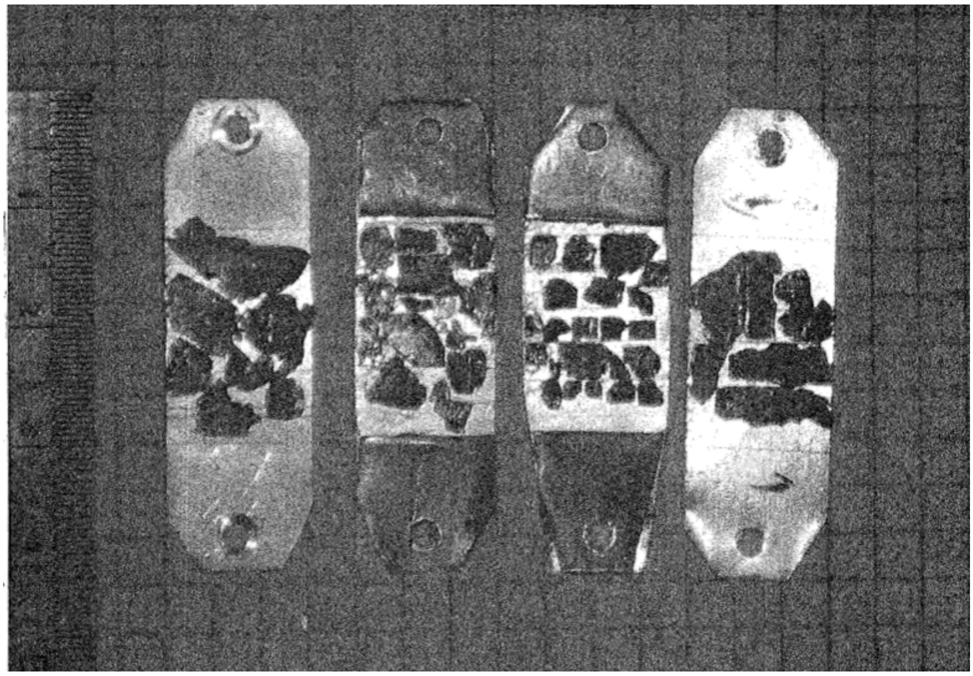

Figure 2.6: Example of a KFA sample, comprising a series of single crystals co-aligned and mounted on four aluminium plates.

multiple sample plates were used and stacked along the direction of incident neutrons.

2.2.2 Experimental details

Neutron scattering experiments were performed on D11 and D22 at the ILL in Grenoble, France and on SANS-1 at PSI in Villigen, Switzerland. Both ^{4}He cryostats and dilution refrigerators were used in order to access temperatures either down to 1.5 K or 50 mK respectively. Results were taken between 0.1 and 1.2 T applied both parallel to and at angles up to 75° to the **c**-axis. Incident neutrons of a mean wavelength of $\lambda_n = 10$ Å were used with a wavelength spread of 10%, with the position sensitive detector set to between 15 m and 18 m depending on the applied field.

Despite the noted hysteresis in the magnetisation data during sample characterisation (fig. 2.5) the sample was found to have weak flux line pinning in the field range we were investigating, and as such it was possible to form a vortex lattice by simply applying a field at the desired temperature rather than cooling the sample in field, as is required with higher pinning systems. It was found that the VL order could be further improved by oscillating the field value before measuring. Here, a a small (~ 0.1)% oscillation about the required field is performed, allowing flux lines that are stuck in weak pinning potentials to escape and form a more uniform flux lattice. The success of this technique is very sample-specific: in some situations the oscillation gives flux lines the freedom to explore pinning sites which they would not otherwise have had access to, which can further deform the lattice or give the flux lines some curvature along their length. In this case, however, the improved signal from the VL after field oscillation suggested that the technique had an ordering effect, bringing the VL closer to its equilibrium position, and so the technique was used.

2.2.3 Structure of the vortex lattice

The structure of the VL and its relative orientation to the host crystal can provide a great deal of information regarding the superconducting state. For all results where B was applied parallel to **c**, a hexagonal lattice of the kind seen in figure 2.7 was observed. The **a** and **b** directions in KFe_2As_2 are equal, giving the **ab** plane square symmetry. Therefore, the two orientations of the vortex lattice which are aligned with the **a** and **b** directions have the same orientational free energy, resulting in a degeneracy of the two orientations and an equal population of flux lines in each domain. A single domain extends within the sample on a much larger length scale than the spacing between the flux lines, leading each domain to undergo Bragg diffraction. A diffraction pattern from an applied field of 0.2 T at 1.5 K demonstrating two degenerate hexagonal domains is shown in figure 2.7, with an two overlayed hexagons on the diffraction pattern indicating which Bragg reflections result from each domain. Confirmation of this explanation is seen in results where the applied field is tilted away from the **c**-axis of the material. At small angles, the underlying superconducting state experienced by the vortex lattice remains relatively unchanged, however the **a** and **b** axes are no longer degenerate, since one orientation of the VL now has a lower free energy than the other and so we observe only a single domain of the VL. Diffraction patterns such as those in Figure 2.7 were obtained from the combination of 4 separate images, each one having been rocked onto the Bragg condition, at constant temperature, for each one of the sets of three spots. Since spot positions can be dependent on diffraction angle as the spots are rocked through, only data from the peak of the rocking curve was used to determine the position of the spots. Figure 2.7 shows the full range of conditions over which the flux lattice of KFA was investigated. A slightly distorted hexagonal lattice was observed throughout, with no distinct first order type transitions to a square phase found in fields up to $\sim 0.5B_{c2}$. These structure scans were done between 0.2 T and 0.9 T, providing information about the structure of the VL as a function of field. This information is expressed in terms of VL opening angle, shown in figure 2.8, showing a systematic change in the VL distortion as a function of field. Whilst the VL structure does vary with field, the absence of structure transitions, such as to a rhombic lattice or a re-orientation transition, indicates that the superconducting properties of KFA as a function of angle about the **c**-axis of the material are fairly isotropic, or at least does not poses strong structure. It is expected from observations with the cuprate superconductors that strong fourfold symmetry in the order parameter, i.e *d*-wave superconductivity, would result in first order transitions to a square or rhombic lattice before reaching a major fraction of B_{c2} (White et al., 2009; Ichioka et al., 1999). However, we have investigated up to half of the superconducting critical field and found no distinct transitions. The systematic increase in lattice distortion does, however, show that the electronic and superconducting properties of the system cannot be completely isotropic in the **ab** plane, as this would result in a regular hexagonal lattice at all observed fields. Calculations from both non-local London theory (Kogan et al., 1996; Kogan and Miranović, 1997; Kogan et al., 1997) and Eilenberger theory (Suzuki et al., 2010) have shown that Fermi surface and order parameter anisotropy result in structure changes as a function of field. Whilst these calculations were not intended as a study of pnictide superconductors, their main focus being on the cuprate systems and explaining the transition rich phase diagram of many unconventional superconductors, we can note

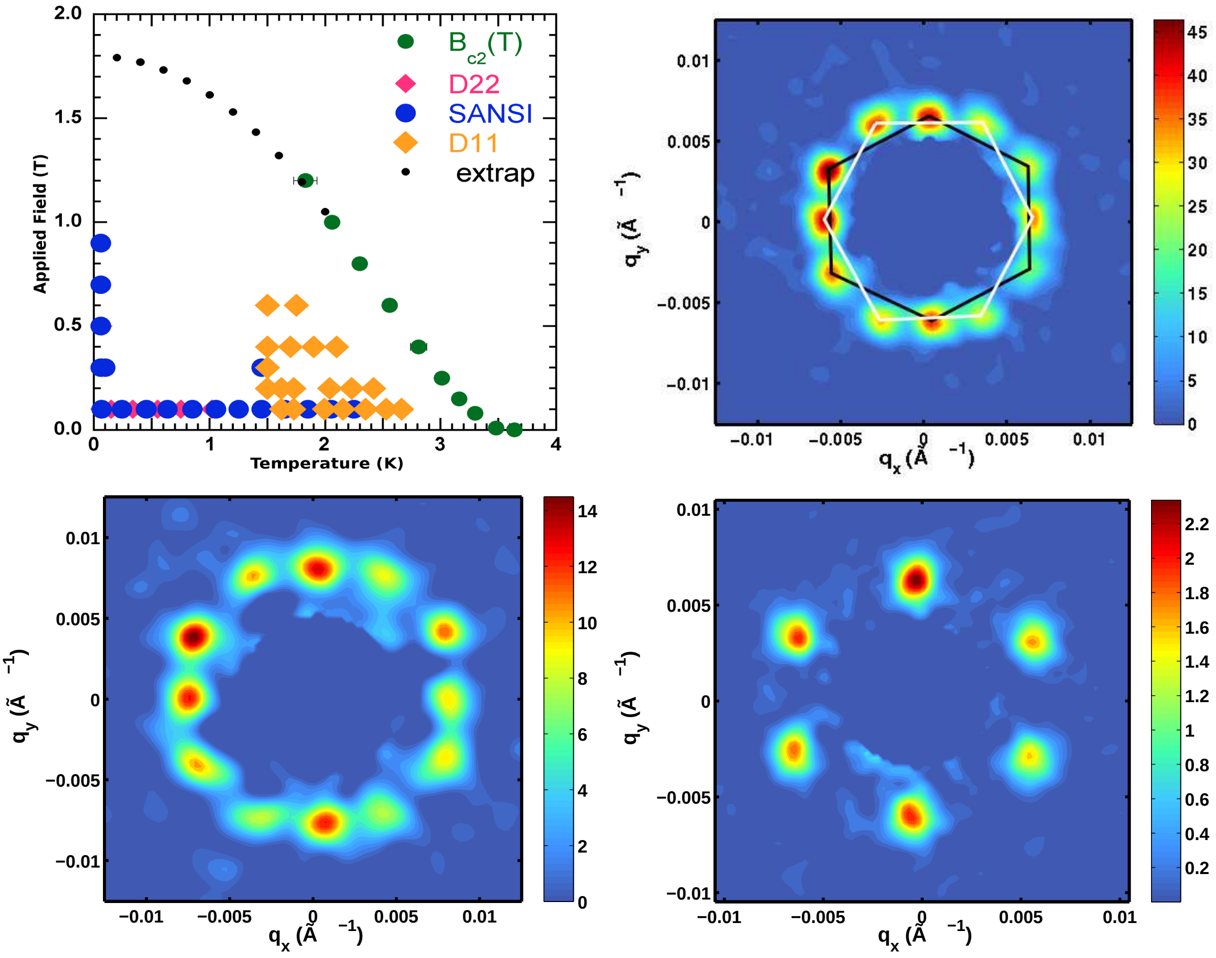

Figure 2.7: Top left: phase diagram showing the location of SANS measurements taken on KFA with the field applied parallel to the **c** axis of the crystal. We indicate measured values of the upper critical field, B_{c2}, with an extrapolated value above our measurement range shown under *extrap*. Measurements of the flux lattice are indicated, with data taken at either D22 or D11 of the ILL, or on SANSI at PSI. Top right: diffraction pattern at 1.5 K in an applied field of 0.3 T, showing two degenerate domains of slightly distorted hexagonal lattice, highlighted in white and black respectively. Bottom left: Figure showing the diffraction pattern at 0.3 T at a temperature of 1.5 K, again showing two degenerate domains of slightly distorted hexagonal lattice. Bottom right: diffraction pattern at 0.2 T, 1.5 K with the applied field at an angle of 10° to the **c** axis of KFe_2As_2 (following the geometry indicated in fig. 1.3), showing a single domain slightly distorted hexagonal lattice.

the general observation that anisotropies in the electronic structure lead to a field-driven change in vortex lattice structure as a function of field. We therefore deduce that while the electronic structure in the **ab** plane of KFA cannot be completely isotropic, due to the field-driven variation in structure, it must be reasonably so to avoid the structure transitions observed in other unconventional superconductors.

The vortex lattice structure was also relatively invariant with temperature, shown in figure 2.8, where the opening angle of the vortex lattice remains at approximately 58 degrees across the full temperature range of superconductivity in an applied field of 0.1 T. This further suggests that the superconducting order parameter must be reasonably isotropic in the **ab** plane, since anisotropy may express itself in changes in the vortex lattice structure as a function of temperature (Bianchi et al., 2008). It has been seen in the cuprates that vortex nearest neighbour directions have a tendency to align with the nodal directions of the order parameter (White et al., 2009) at high field. With increasing temperature, however, nodes become smeared with respect to the excitation spectrum of the system, as quasiparticles are able to be excited across expanding regions of the gap as $k_B T$ increases. This may lead vortex nearest neighbour directions to no longer be governed by node topology. However, nodal structures in the **ab** plane do not always manifest themselves in vortex lattice structure transitions with temperature, such as those in $\mathrm{YBa_2Cu_3O}$ which are invariant with temperature and are only driven by changes in field (White et al., 2011). In YBCO, however, the structure of the vortex lattice in YBCO does show a systematic variation with temperature, which is discussed in a later section 3.3.1, which can be attributed to reduced influence of the nodes at higher temperatures. The absence of structure transitions or significant variation in these temperature dependent data on KFA can only therefore *suggest*, not determine, that the superconducting properties as a function of angle about the **c** axis are reasonably isotropic.

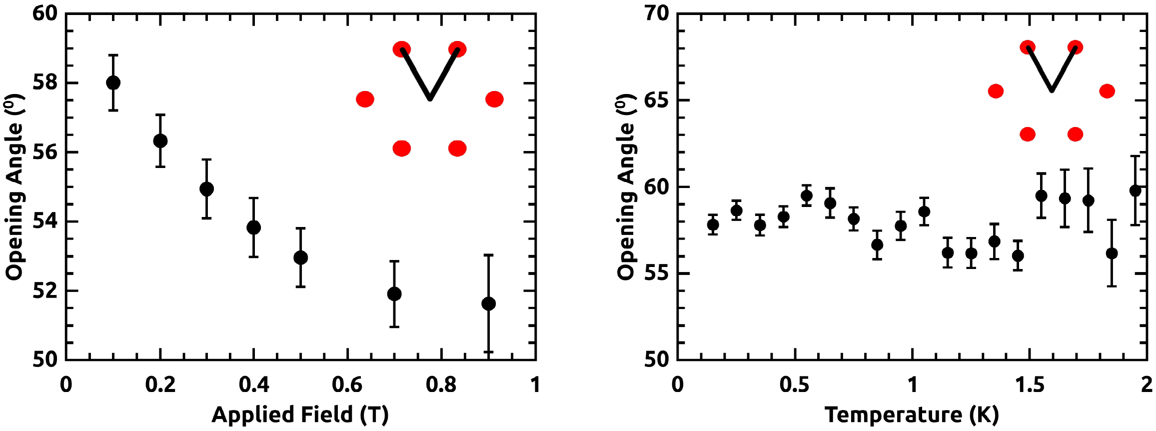

Figure 2.8: Left: Opening angle of the VL, θ, as a function of applied field at a temperature of 50 mK. Right: Opening angle of the VL as a function of temperature at an applied field of 0.1 T. Relevant opening angle with respect to an example hexagonal lattice is shown inset.

The structure of the vortex lattice may also be determined by the scattering vector of the diffraction spots. The packing structure of a lattice determines the inter vortex spacing, and therefore the spacing of Bragg planes. For square or hexagonal lattices, the vortex spacing is identical for all nearest neighbours. However, for a distorted lattice such as those observed in KFA, the spacing between vortices depends on which neighbour is being chosen. This, shown in figure 2.9, results in two different $\mathbf{q}$-vectors which define the lattice which allow the anisotropy of the lattice to be expressed either in an anisotropy parameter, $\nu = |\mathbf{q}_1|/|\mathbf{q}_2|$ or as a lattice opening angle θ. Given that all rocking done in these experiments was along either the horizontal or vertical axis of the reciprocal lattice plane we can define two distinct spot types with respect to this experimental method. On-axis spots are those that align with either the horizontal or vertical rocking directions, labelled in red in figure 2.9, and therefore are also aligned along either the $\mathbf{a}^*$ or $\mathbf{b}^*$ reciprocal lattice directions. Off-axis spots are those at an angle to these rocking directions, whose reciprocal lattice planes are also at an angle to the $\mathbf{a}^*$ and $\mathbf{b}^*$ directions and are labelled in blue in figure 2.9. When the vortex lattice in the **ab** plane of KFA distorts away from an isotropic hexagon it does so along the **a** or **b** axis, depending on which domain we are investigating, and therefore the on axis and off axis spots sit at different scattering vectors, which are labelled in figure 2.9 as $\mathbf{q}_1$ and $\mathbf{q}_2$.

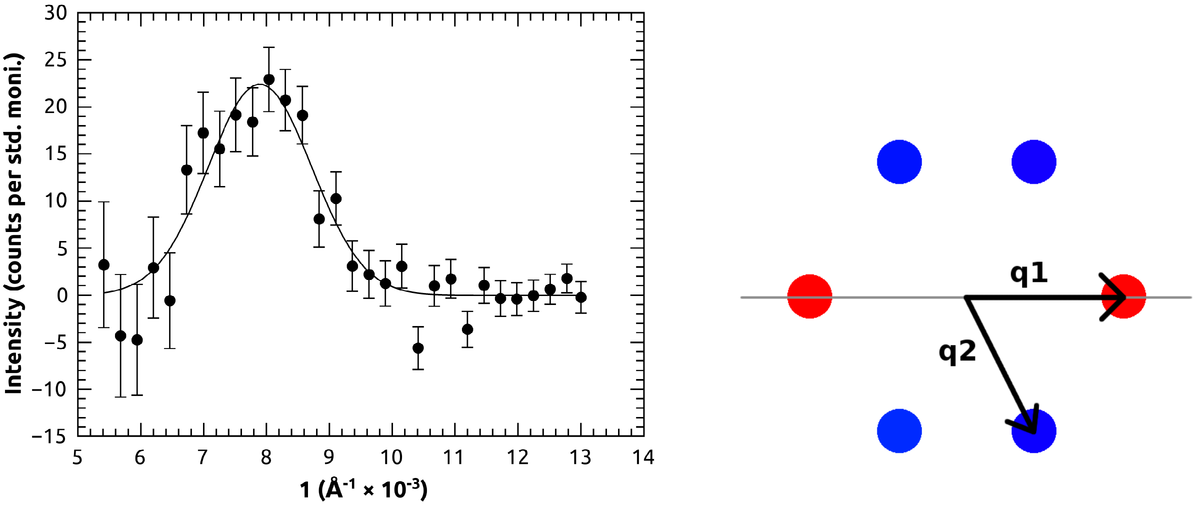

Figure 2.9: Left: A typical plot of diffracted intensity as a function of scattering vector, q, for a single Bragg reflection in an applied field of 0.3 T at 50 mK. Q-vector shown here is q_1 in the right hand diagram of this figure. Right: Schematic diagram of a diffraction pattern for an arbitrary hexagonal lattice. The two scattering vectors, $\mathbf{q}_1$ and $\mathbf{q}_2$ are labelled with spots at common $\mathbf{q}$ values sharing colours. A hypothetical rocking direction is shown in grey, hereby defining on axis spots as those intersecting this axis of rock (red spots) and off axis spots as those at an angle away from this axis of rock (blue spots).

2.2.4 Field dependence of the vortex lattice form factor

Making use of the Christen formula (equation 1.71) the vortex lattice form factor was investigated as a function of field. We replace the reciprocal space lattice vector, **G**, with the experimentally determined scattering vector **q**, giving us the following expression for the form factor,

$$I_{\mathbf{q}} = 2\pi\phi V\left(\frac{\mu}{4}\right)^2 \frac{\lambda_n^2}{\Phi_0 \mathbf{q}}|F_{\mathbf{q}}|^2 \tag{2.1}$$

where all symbols retain their former meaning. The integrated intensity, I_q, is obtained from a scan of intensity in a Bragg reflection as a function of rocking angle, shown in figure 2.10, and averaged over the number of Bragg spots. The **q**-vector is obtained from the radial plot of intensity as a function of scattering vector as seen in figure 2.9 and is Bragg-spot-specific in a distorted lattice such as the one under investigation in KFA. The incident neutron flux, ϕ, is taken from a measurement of the incident neutron beam. This is done separately to a standard measurement by removing the beamstop on the detector whilst attenuating the neutron beam by a known amount to discover the number of incident neutrons per normalisation factor, usually a set count on the monitor.

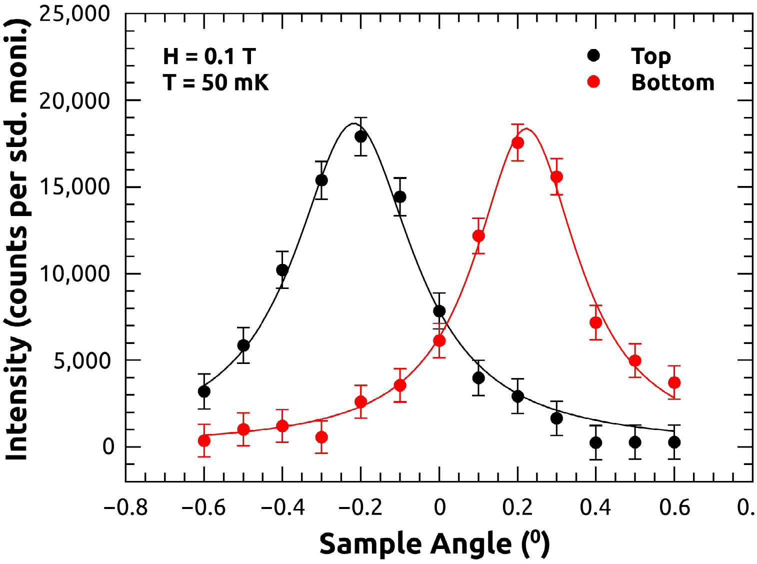

Figure 2.10: An example of a typical rocking curve from the on axis spots ($\mathbf{q}_1$ in fig. 2.9) in an applied field of 0.1 T at 50 mK. Rocking curves were fitted to a Lorentzian, shown as a solid line, in order to determine the integrated intensity.

Figure 2.11 shows the form factor variation with field at a temperature of 50 mK for the on-axis spots - those spots which were rocked through directly rather than being off the axis of the rock. These were fitted to the London model with core/non-local corrections (equation 1.28), which provides a good model of the data. The core cut-off parameter, c, was expected to be ~ 0.5, as theoretical work has suggested that this is an appropriate value for this parameter (Ichioka et al., 1997). It can be seen that the form factor decreases with field, which is expected as the vortex cores begin to overlap with reduced spacing at higher fields. At 50 mK, using $\xi = 13.5$ nm (taken from a B_{c2} of 1.3 T), the fit returned values of $\lambda = 203$ nm and $c = 0.52$. At 1.5 K, with $\xi = 15.9$ nm, the fit gave values of $\lambda = 240$ nm and $c = 0.55$. This fit suggests a conventional field dependence for KFA, with no multi-gap effects (Cubitt et al., 2003), and allows us to extrapolate to the zero field penetration depth.

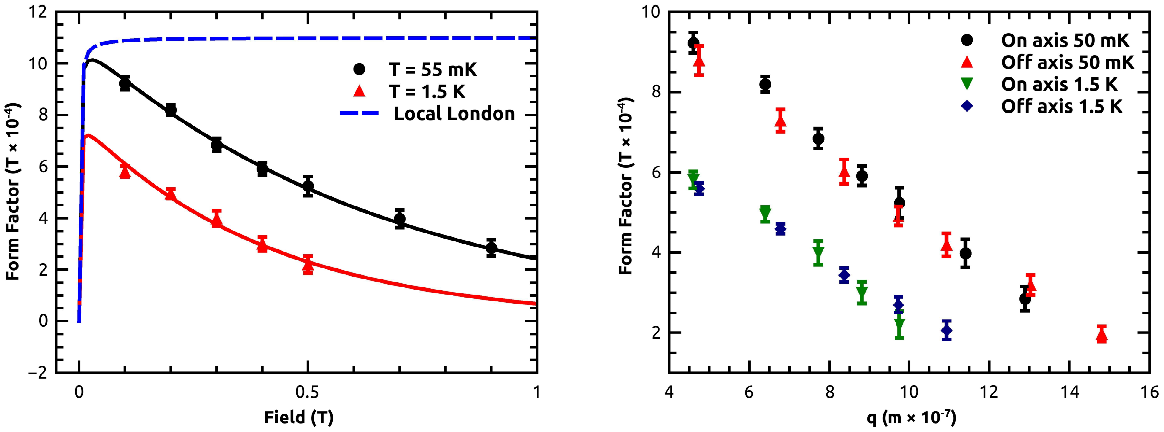

Figure 2.11: Left: Form factor of the vortex lattice for the on axis spots ($\mathbf{q}_1$ in fig. 2.9) as a function of applied field at both 50 mK and 1.5 K. Data was fitted to the London model (equation 1.28) with core/non-local corrections, shown as solid lines. At 50 mK, using $\xi = 13.5$ nm, the fit returned values of $\lambda = 203$ nm and $c = 0.52$. At 1.5 K, with $\xi = 15.9$ nm, the fit gave values of $\lambda = 240$ nm and $c = 0.55$. For comparison, the local London model with no core corrections is shown as a dashed line. Right: Form factor as a function of scattering vector $\mathbf{q}$ for all diffractions spots.

The data fitted to the London model in figure 2.11 is for the on axis spots only, since the off axis spots have a different Form factor at equivalent fields owing to the different lattice spacings. However, when plotting these data against their $\mathbf{q}$-vector we can see that both the on axis and off axis spots follow the same behaviour, confirming the basal-plane isotropy of the pairing.

The temperature dependence of the VL form factor and field dependence of the VL structure can provide strong indications as to the gap structure of the material under investigation. However, it is important to ascertain if the material is a clean superconductor, such that the gap is not strongly affected by impurities and our observations are therefore of intrinsic behaviour. Using the information we have obtained on the London penetration depth, it is possible to make an estimate of the ratio of the electron mean free path to coherence length (ℓ/ξ_0), which should be greater than 1 for a clean material. In the case of a electronically 2D material such as KFA, where the London penetration depth is predominantly determined by the supercurrents flowing in the basal plane, we can relate λ_L to the electronic properties by

$$\frac{1}{\lambda_L^2} = \sum_i \frac{n_i e^2 \mu_0}{m_i^*}. \tag{2.2}$$

This represents the added the contributions of each approximately cylindrical piece of Fermi surface, with number density n_i carriers of effective mass m_i^*. ARPES, dHvA and band structure calculations (Hashimoto et al., 2010b; Sato et al., 2009; Terashima et al., 2010) have given all FS sheets present in KFA to be hole sheets, and from the single valence of potassium we take an addition of one hole per KFe_2As_2 unit. Therefore,

$$n = \sum_i n_i \approx 9.7 \times 10^{27} m^{-3} \tag{2.3}$$

From a penetration depth of $\lambda = 203$ nm and a band weighted average inverse effective mass

$$\left\langle \frac{1}{m_i^*} \right\rangle = \frac{1}{ne^2 \mu_0 \lambda^2} \tag{2.4}$$

we can deduce the effective mass of the electrons in the lattice as 1.3×10^{-29} kg, or around ≈ 14 m_e. This is within the range of 6 to 18m_e found by dHvA measurements (Terashima et al., 2010). Using the following expression for the conductivity σ in the basal plane

$$\sigma = \sum_i \frac{\mu_0 e^2 \tau_i}{m_i^*}. \tag{2.5}$$

The band averaged impurity scattering time can be calculated using our data on the penetration depth and the in-plane resistivity of KFA. This is given by

$$\tau = \mu_0 \lambda^2 \sigma. \tag{2.6}$$

From the residual resistivity ratio in our sample of ≈ 400, and the room temperature in plane resistivity of $\rho = 4.8 \times 10^{-6} \Omega$ m (Terashima et al., 2009) we find a low temperature value of $\tau = 4.3 \times 10^{-12} s$. For a 2D material, the ratio of electron mean free path to the coherence length is $\approx 3.5\ k_B T_c/(\hbar/\tau)$. With a $T_c = 3.6$ K, we find the ratio $\ell/\xi_0 \approx 7.1$. This indicates a clean material, therefore one in which the gap structure is not affected by impurities and our observations are of intrinsic properties.

2.2.5 Temperature dependence of the vortex lattice form factor

The temperature dependence of the scattered intensity at the Bragg peak is another useful measure of the superconducting properties of a material, since scattering from the lattice has a dependence on the superfluid density. Since thermal energy splits Cooper pairs, leading to the destruction of superconductivity at T_c, it is evident that the number of superconducting pairs will decrease monotonically as $T \to T_c$. This behaviour, however, is not identical for all superconductors, as the temperature dependence of quasi-particle excitations in the material is governed by its gap structure. As such, the temperature dependence of scattered intensity can provide insights into the gap structure of the material being studied. For the simple BCS gap, the superfluid density saturates as k_bT passes below the gap of 2Δ, which results in a flattening of the temperature dependence at lower temperatures. For KFA, our results are shown in figure 2.12 . The results here are published in the respective paper by Furukawa *et al* (Kawano-Furukawa et al., 2011).

Here, I follow the method of fitting the temperature dependence presented in the paper on these results by Furukawa *et al* (Kawano-Furukawa et al., 2011). To fit the temperature dependence, the behaviour of the VL was approximated to the London limit, as we were at a small fraction of H$_c$, giving us a Form Factor

$$F = \frac{B}{1+\mathbf{q}^2\lambda^2} \simeq \frac{B}{\mathbf{q}^2\lambda^2}\,\alpha\,\frac{1}{\lambda^2} \propto \rho_s \tag{2.7}$$

where ρ_s is the superfluid density normalised to its value at $T = 0$, $\mathbf{q}$ is the reciprocal lattice vector and λ is the penetration depth as discussed earlier. The temperature dependence of the superfluid density was calculated in the local limit, taking into account the fourfold rotational symmetry about the $\mathbf{c}$ axis, with (Prozorov and Giannetta, 2006)

$$\rho_s(T) = 1 - \frac{1}{4\pi k_B T}\int_0^{2\pi}\int_0^{\infty}\cosh^{-2}\left(\frac{\sqrt{\varepsilon^2+\Delta^2_{\mathbf{k}}(T,\phi)}}{2k_BT}\right)\mathrm{d}\phi\mathrm{d}\varepsilon \tag{2.8}$$

where T is the reduced temperature, T/T_c, ϕ is the azimuthal angle about the Fermi

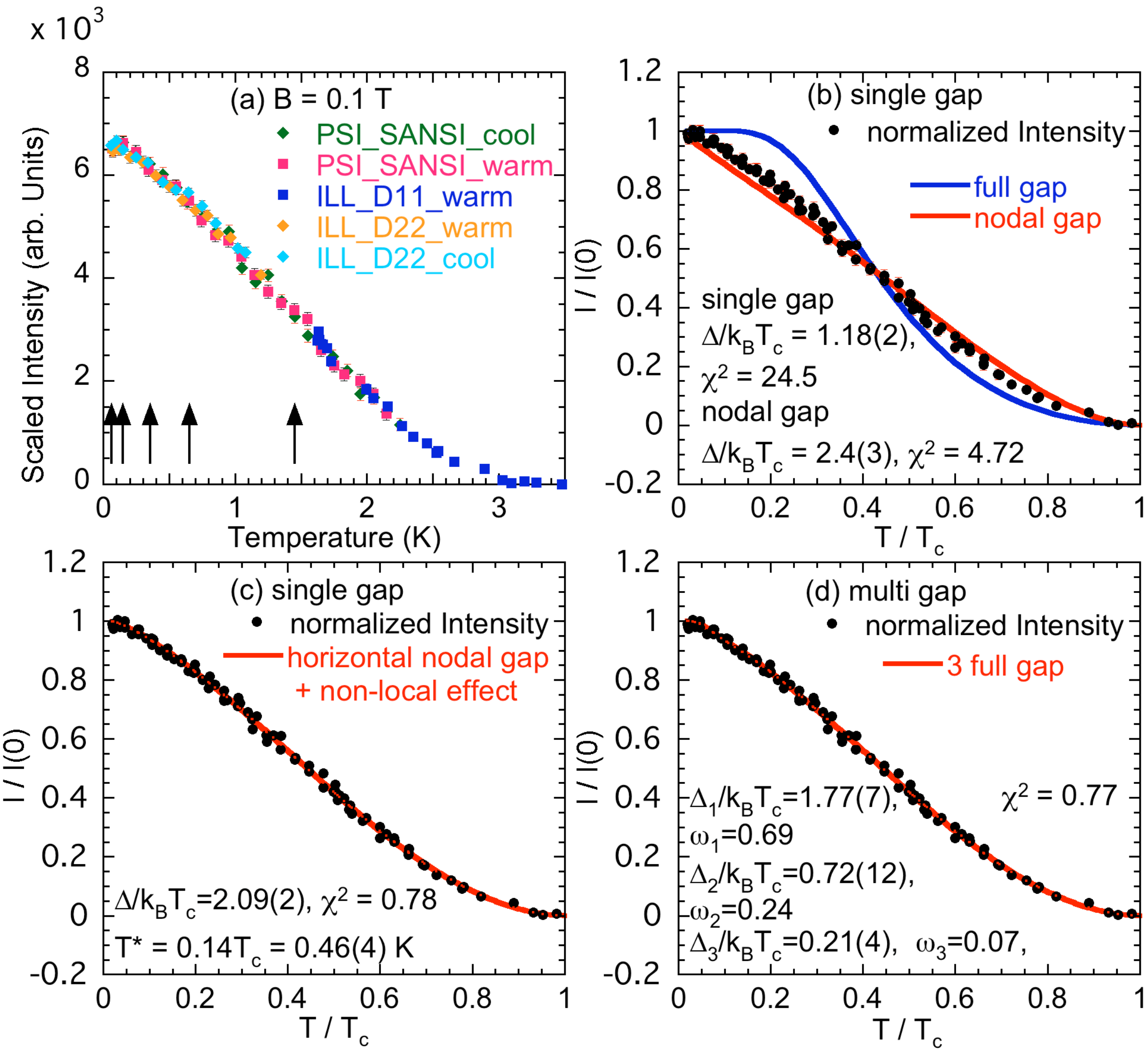

Figure 2.12: Temperature scan of scattered intensity in arbitrary units, with several model fits, reproduced from Furukawa *et al* (Kawano-Furukawa et al., 2010). a) Shows the raw data from all experiments scaled to the same intensity. b) Single gap models, both full and nodal gap. c) A single gap with horizontal line node and non-local effects included. d) A multi gap model with three full gaps. Gap magnitudes and other parameters are shown inset.

surface and $\sqrt{\varepsilon^2 + \Delta_{\mathbf{k}}^2(T,\phi)}$ gives the excitation energy spectrum. The gap function was assumed to be separable into temperature and momentum dependent factors such that $\Delta_{\mathbf{k}}(T,\phi) = \Delta_{\mathbf{k}}(\phi)\Delta_0(T)$, where $\Delta_{\mathbf{k}}(\phi)$ describes the momentum dependent gap as a function of angle around the Fermi surface. In the weak coupling limit, $\Delta_0(T)$ can be approximated by

$$\Delta_0(T) = \Delta_0(0)\tanh\left(1.78\sqrt{\frac{T_c}{T} - 1}\right), \tag{2.9}$$

where Δ_0 is the magnitude of the gap at zero temperature. The Δ_k gap functions considered are as follows. For a single full gap across the entire Fermi surface, $\Delta_{\mathbf{k}}$ was taken as being equal to 1. For the nodal gaps, both the angular variation due to a d-wave pairing state, $\Delta_k(\phi) = \cos(2\phi)$ and a horizontal node gap, $\Delta_k(k_z) = \Delta_0\cos(\mathbf{k}_z\mathbf{c}/2)$ were considered. These give the same ρ_s, as the temperature dependence can give an indication of the presence of nodes, but does not distinguish between various types. To deduce node geometry, it is necessary to investigate VL structure, which will be discussed later.

Kostin and Legget (Kosztin and Leggett, 1997) showed that, for nodal gap functions, non-local corrections to λ will result in the approximately T-linear dependence of ρ_s to cross over to a T^2 behaviour below a certain temperature $T^* \approx \Delta_0/k_B\kappa$ where κ is the GL parameter (Amin et al., 2000, 1998). This behaviour may be approximated by the following expression

$$n_s(T) = 1 - (1 - n_s(T))\left(\frac{T_c + T^*}{T_c}\right)\left(\frac{T}{T + T^*}\right) \tag{2.10}$$

where n_s is the superfluid density, as calculated above in the local limit.

The final gap model to be considered was a multigap model, where the contributions to the superfluid density from each gap were considered to be both separate and additive (Carrington and Manzano, 2003). The three gap model used here was given by

$$\rho_{tot}(T) = \omega_1\rho_1(T) + \omega_2\rho_2(T) + (1 - \omega_1 - \omega_2)\rho_3(T) \tag{2.11}$$

where ρ_{tot} is the total superfluid density from all gaps, ρ_n describes the superfluid density due to gap Δ_n, and ω_n is a fitted parameter ≤ 1, and is given no temperature dependence.

It can be seen that the scattered intensity from KFA continues to increase down to a very small fraction of T_c, with perhaps only the last data point breaking this trend (at ~ 70 mK). This suggests that quasi-particles are still being excited at low temperatures, indicating either nodes in the gap structure, in which case excitations may continue down to 0 K, or a range of gap values on the Fermi surface, at least one of which must be small. Since the Fermi surface of KFA, like other pnictides, possesses multiple Fermi surface sheets it is possible that the superconducting gap that forms on each sheet has either a different magnitude, or is of a different type as is possible for BFAP, which is discussed later in section 2.4. These possibilities can be seen in the model fits, as as a single full gap does not fit the data, whereas a nodal gap including non-local effects and multi-gap models are in much better agreement. It is interesting to note that a nodal gap ignoring non-local effects does not fit well. Given that the field-dependent form factor suggests an absence of multi gap effects (Cubitt et al., 2003), this leaves the nodal gap functions as the most likely candidates for KFA. As previously stated, the absence of vortex lattice structure transitions indicate that the superconducting properties as a function of angle around the **c** axis must be fairly isotropic. Therefore a gap function with nodal lines circulating around the Fermi surface sheets, seen in figure 2.13 would seem to fit the data.

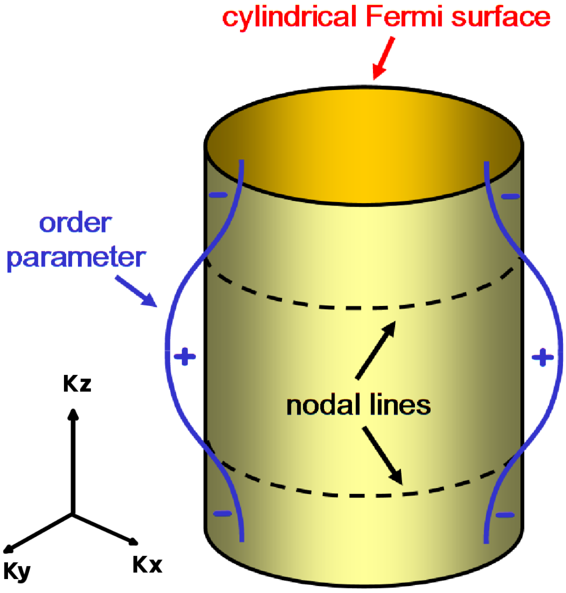

Figure 2.13: A sketch of the $\mathbf{k}_z$ dependence for the order parameter proposed for KFA. The Fermi surface of KFA is approximated as cylindrical, with the proposed superconducting order parameter shown in blue. This is only given k_z dependence, switching sign along k_z leaving two circular line nodes around the Fermi surface. Image from (Kawano-Furukawa et al., 2011).

These results fall into slight conflict with other published data, with a general consensus of a nodal gap structure (Fukazawa et al., 2009; Dong et al., 2010; Hashimoto et al., 2010a), but with reports of *d*-wave and other exotic structures present (Thomale et al., 2011; Maiti et al., 2011; Okazaki et al., 2012). We note that the absence of any distinct structural transition to a square lattice, in contrast with those consistently seen in the confirmed *d*-wave cuprate systems, our data strongly indicates that this system *cannot* be *d*-wave in nature. High resolution laser ARPES results have produced an octet line node structure as a function of angle around the **c** axis in KFA (Okazaki et al., 2012). Whilst this is not the horizontal line node structure proposed here, we can note that a vortex lattice, whose highest possible symmetry is sixfold, is unable to satisfy any eightfold symmetric free energy minima conditions. It is possible that the continued variation of VL structure with field observed in fig. 2.8 is a result of frustration between the two symmetries.

2.3 Study of the anisotropic vortex lattice where the field is no longer applied in the basal plane

The structure of the vortex lattice has been fairly isotropic for all conditions studied with B parallel to **c**, a result of the superconducting properties of KFA being reasonably isotropic in the **ab** plane. However, due to its tetragonal structure, strong anisotropy between the **ab** plane and the **c** axis is expected. In order to investigate this anisotropy and its consequences for the vortex lattice, the experimental geometry of the field applied parallel to the **c** axis was altered by rotating the applied field away from the **c** axis [1]. The structure of the VL is determined by the interactions between the vortices, which is affected by anisotropies in the carrier mass, m*, superconducting gap and Fermi velocity as a function of angle around the plane perpendicular to the vortex. Rotating the angle between the **c** axis and the applied field allows us to use the vortex lattice as an effective probe of these anisotropies, and for both rotations in the [100] and [110] direction, we designate the angle between the applied field and the **c** axis as α. Rotations were done towards both the [100] crystal lattice direction and the [110] direction in an applied field of 0.2 T. At such a low field, where the inter-vortex spacing ($\approx$ 100 nm) is much greater than the coherence length ($\approx$ 15 nm), we expect the structure of the lattice to be dominated by the anisotropy of the penetration depth in the plane perpendicular to the applied field. The simplest method to describe the effect of an anisotropic penetration depth is the anisotropic London model, discussed in section 1.4. With the penetration depth in the London model being given by $\lambda^2 = ne^2\mu_0/m^*$, anisotropic London theory expresses an anisotropic penetration depth by re-writing the carrier mass, m*, as $\mathrm{m}^*_{\mathbf{ik}}$ where **i** an **j** are components of the effective mass tensor. With this being a 2nd-rank tensor, we can expect a vortex lattice with an elliptical cross section whose axial ratio is being determined by λ_x/λ_y.

---

[1] The work presented here forms part of a larger study on the vortex lattice of KFA with the field applied at an angle to the **c** axis, submitted to PRB for review (Morisaki-Ishii et al., 2013) .

2.3.1 Structure of the vortex lattice with B tilted from the c axis

Figure 2.14 shows the vortex lattice diffraction patterns as a function of α for rotations in the [100] and [110] directions at temperatures below 350 mK. An immediate consequence of rotating the applied field away from the **c** axis along either the [100] or [010] direction is the breaking of the degeneracy between the **x** and **y** axes in the vortex lattice plane. With the superconducting properties of either the **a** or **b** axes now being mixed with the **c** axis, the plane in which the vortex lattice sits no longer appears as square symmetric. Therefore, one of the vortex lattice domains in the superconductor will have a lower free energy than its sister orientation, and random nucleation of flux lines will populate one domain in preference to the other. With the degeneracy broken, we have a single hexagonal lattice for rotations in the [100] direction, rather than a mix of two domains as seen previously in figure 2.7 and shown in figure 2.14. For rotations in the [110] direction however, the mixing of the superconducting properties of the **c** axis occurs equally with the **a** and **b** axis, so despite anisotropy of the **xy** plane of the vortex lattice, the system remains degenerate and we maintain the two domains of the VL as the field is rotated away from the **c** axis, seen in figure 2.14.

We parametrise the VL distortion as a function of α in terms of either the angle between the VL basis vectors or the angle of offset between the two domains. For the [100] rotation, with a single VL domain of lower free energy, we define the β as the angle between the two basis vectors of the primitive cell, indicated in fig. 2.14. This distortion as a function of α is displayed in fig. 2.15, showing a continuous change as the applied field is rotated towards the basal plane. The evolution of the [110] rotation, however, is quantified by the misalignment angle, η, between the two degenerate domains of VL as indicated in fig. 2.14. Here we can see that the rotation in the [110] direction also undergoes a smooth distortion as the field is rotated towards the [110] domain to the highest imaged rotation angle of $\alpha = 80°$. This is in contrast with data taken at higher temperatures (Kawano-Furukawa et al., 2013), where the rotation towards the [110] direction gave a

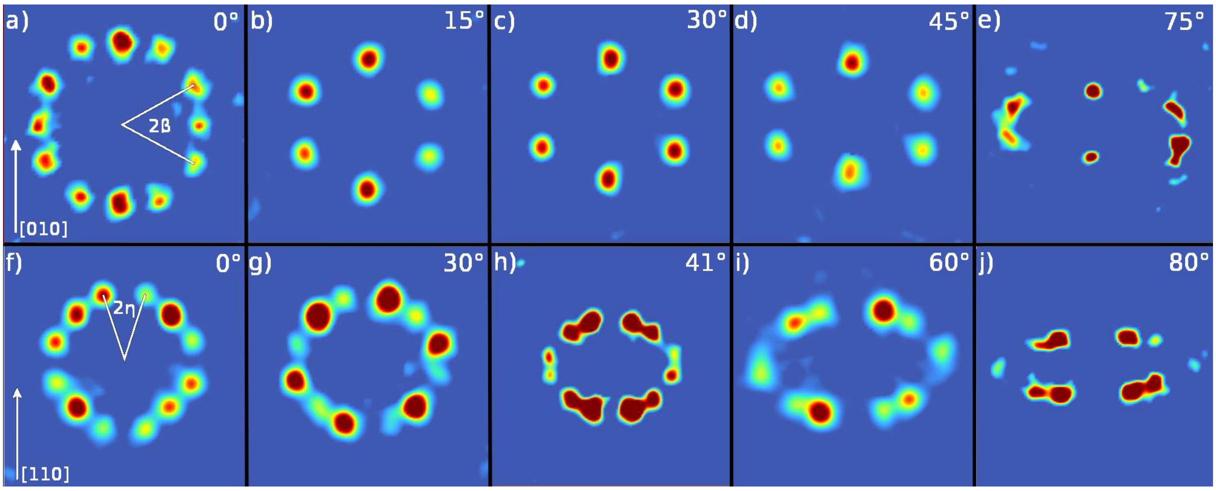

Figure 2.14: Vortex lattice diffraction patterns for the rotations about both the [010] and [110] directions. Panels (a)-(e) correspond to the rotations about [010], whilst panels (f)-(j) correspond to rotations about [110], with rotation angle α indicated in the panel. We define two vortex lattice opening angles, β and η in panels a and f respectively.

first order structure transition around $\alpha = 45°$. Here, the two degenerate VL domains gave way to a single domain aligned along the [110] direction.

The fourfold anisotropy which we observe in these results shows a strong dependence on the direction of applied field. No sign of a transition to a rhombic phase was seen throughout the measurements with the field applied in the basal plane, however when the field is rotated away from this direction we find contrasting results for rotation towards the [100] and [110] directions. Local London theory is unable to account for the fourfold anisotropies displayed in these results, however non-local corrections to London theory which couple the vortex lattice free energy with anisotropies in the Fermi velocity and superconducting gap have proven successful in providing a VL free energy minima in the presence of such anisotropies (Kogan et al., 1996; Nakai et al., 2002). The difference in VL structure as a function of temperature for rotations along the [110] direction noted in (Kawano-Furukawa et al., 2013) could be attributed to the varying importance of non-local effects with temperature. We can note, therefore, that the behaviour we observe indicate that a simple model of a cylindrically-symmetric Fermi surface with horizontal line nodes, which proved able to explain the temperature dependence of the vortex

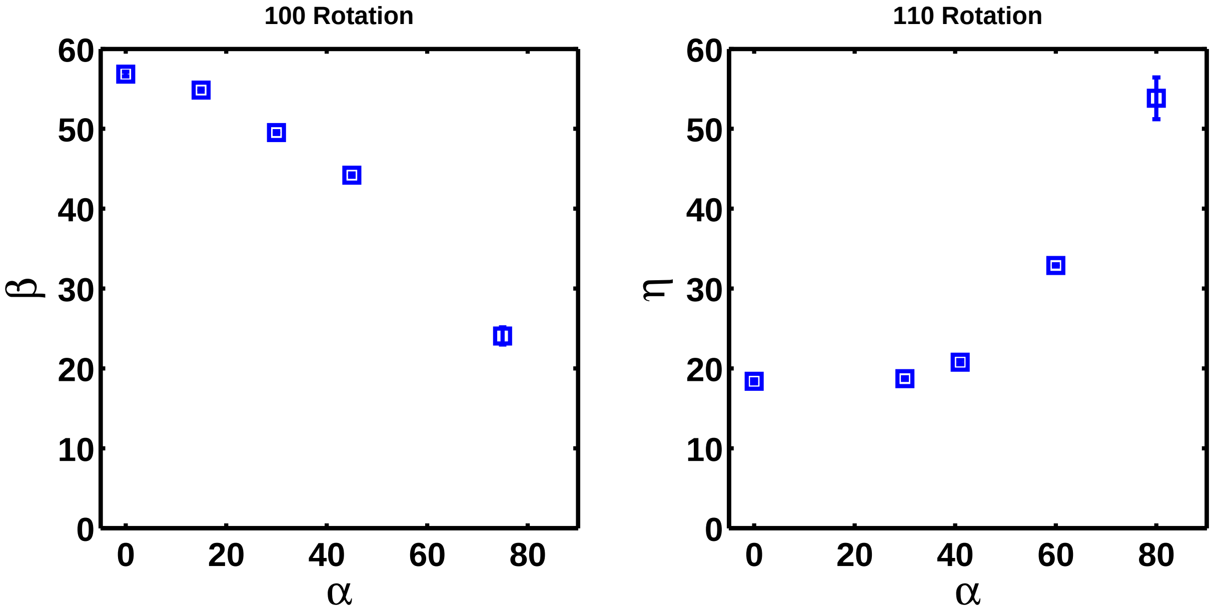

Figure 2.15: Graph showing the VL distortion, defined by either the parameter β or ν in fig. 2.14, as a function of rotation angle α.

lattice form factor in section 2.2.5, is insufficient to describe KFA. ARPES results and band structure calculations have shown the Fermi surface and gap structure to be more complicated than this simplified model.

Following the method described in the section on anisotropic London theory 1.4, we have calculated the anisotropy factor $\gamma(\alpha) = \lambda_{\mathbf{a}}/\lambda_{\mathbf{b}}$ as a function of rotation angle, α for rotation in the [100] direction. The parameter $\gamma(\alpha)$ is determined experimentally by the axial ratio of the ellipse on which the diffraction spots reside. This anisotropy factor is expressed in anisotropic London theory as

$$\gamma(\alpha) = \gamma_{\mathbf{ab}} \left(\frac{1}{\gamma_{\mathbf{ac}}^2} \sin^2 \alpha + \cos^2 \alpha \right)^{-\frac{1}{2}} \tag{2.12}$$

where $\gamma_{\mathbf{ij}}$ is defined by the effective mass ratio $\gamma_{\mathbf{ij}} = \sqrt{m_{\mathbf{ii}}/m_{\mathbf{jj}}}$ (Campbell et al., 1988). Whilst for a tetragonal crystal we may expect $\gamma_{\mathbf{ab}} = 1$, results parallel to the **c** axis gave a slightly distorted lattice, such that $\gamma_{\mathbf{ab}} = 1.06 \pm 0.012$. Figure 2.16 shows the axial ratio for rotation in the [100] direction in an applied field of 0.2 T at a temperature $T \leq 35$ mK fitted to the anisotropic London model, and gives an out of plane anisotropy of $\gamma_{\mathbf{ac}} = 3.4 \pm 0.086$. Whilst this is smaller than the anisotropy of the upper critical field obtained by heat capacity measurements (Abdel-Hafiez et al., 2012), where $\gamma = H_{c2}^{\mathbf{ab}}/H_{c2}^{\mathbf{c}} = 4.5$ which were extrapolated to $T = 0$, it is in much better agreement with $\gamma = 3.52$ at $T = 0$ from resistivity measurements (Terashima et al., 2009). We note that this model, based upon the anisotropy of the system being expressed in terms of the effective mass, is not necessarily appropriate for KFA. The anisotropic London model assumes an approximation of an isotropic gap and ellipsoidal Fermi surface, which our discussion on the fourfold anisotropy of the lattice distortion as a function of rotation direction indicated was too simple to accurately describe KFA. However, we can draw the conclusion that our value of $\gamma \approx 3.4$ indicates the Fermi surface of KFA to posses a reasonably two-dimensional character.

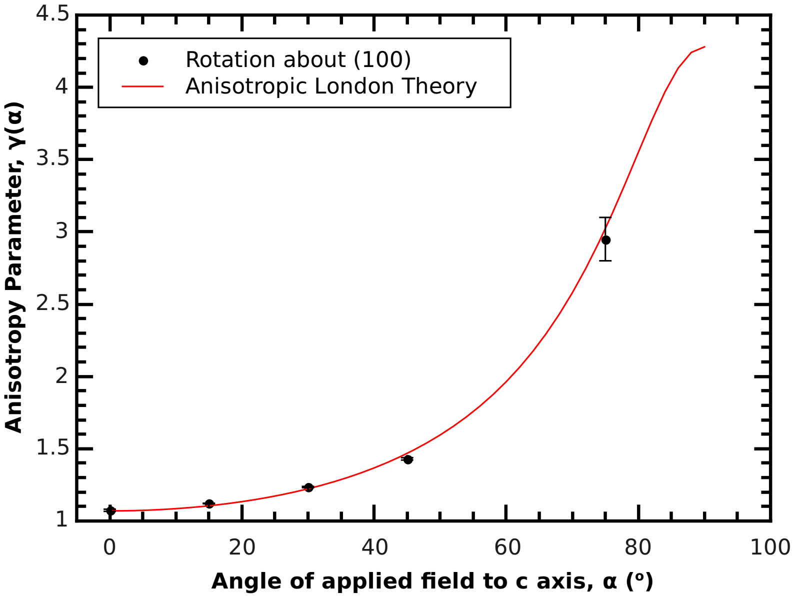

Figure 2.16: Lattice anisotropy parameter as a function of angle of applied field to the **c** axis. Data for rotation about both the (100) direction is shown, alongside a model fit from anisotropic London theory given by equation 2.12, with $\gamma_{ab} = 1.06 \pm 0.012$ and $\gamma_{ac} = 3.4 \pm 0.086$.

2.3.2 Angle dependence of the vortex lattice form factor

The effect of uniaxial crystal anisotropy on the spatial variation of the magnetic field in the mixed state was initially described by Kogan (Kogan, 1981), and is detailed in section 1.4. The theory predicts the effect on the components of the VL form factor in the presence of an effective mass anisotropy, and has been extended to account for an arbitrary field rotation with respect to the crystal frame for SANS results on the vortex lattice (Kealey et al., 2001), and may be further extended to account for anisotropic core effects as in ref. (White et al., 2011). We here apply the theory to the form factor obtained for rotation in the [100] direction from the data shown in fig. 2.14, where the VL form factor is calculated in the same manner as with the field applied parallel to the **c** axis. We see in these results that the top and bottom spots in the diffraction pattern appear stronger with increasing angle α, whilst the left and right spots decrease in intensity. The results in figure 2.17 indicate that this effect is real, and that the form factor becomes increasingly anisotropic as the applied field is rotated towards the basal plane. We note that collection and analysis of this data is more limited than for calculating the VL anisotropy. As the top and bottom spots are drawn closer to the center of the detector with increasing angle α, the background noise increases rapidly, whilst for the left and right spots the signal decreases with increasing α, due to their decreasing form factor shown in figure 2.17. Both of these lead to a rapidly deteriorating signal to noise ratio as the rotation angle α is increased. We can account for this in terms of both the effect of rotation on the London penetration depth and on the core overlap effects. The longer penetration depth for currents in the **c** direction causes the reduction of the form factor for the left and right spots in figure 2.14, whilst the top and bottom spots are mainly governed at small angles by currents in the basal plane and do not experience the reduction for small angles. The core overlap effects, which have the same effect on all the diffraction spots, are governed by the in-vortex-plane B_{c2}. As B_{c2} increases as the field is rotated towards the basal plane, the constant applied field results in a smaller B / B_{c2} fraction with should work to increase the VL form factor. The net result of these at small angles is the increase of the form factor for the top and bottom spots and a reduction in form factor for the left and right spots. The form factor in figure 2.17 was matched to the theoretical curve using the same anisotropy parameters as found in the study of the vortex lattice structure from the same data.

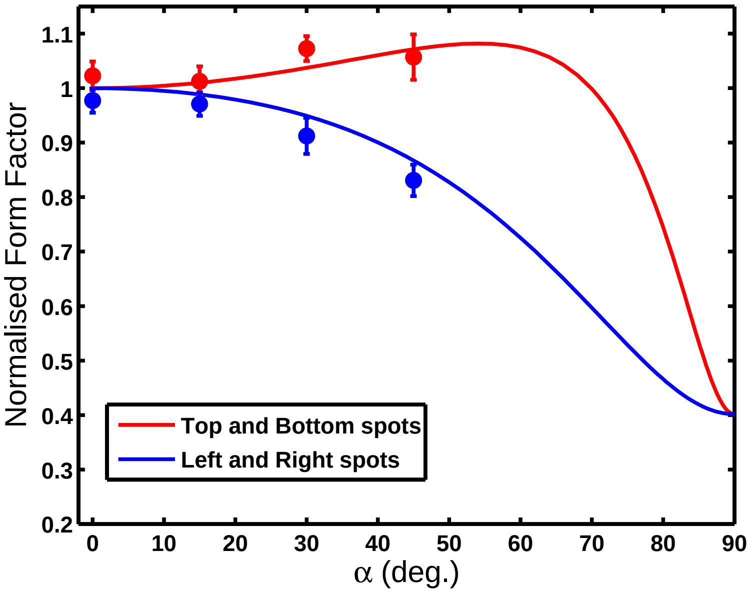

Figure 2.17: Graph showing the vortex lattice form factor for both the on and off axis diffraction spots as a function of angle between the **c** axis and applied field, with rotation along the [100] direction. Data was taken in an applied field of 0.2 T at a temperature $T \leq 350$ mK, corresponding to the diffraction patterns shown in figure 2.14.

2.3.3 Conclusions

The results outlined here gave the first SANS measurements on a pnictide superconductor from an ordered vortex lattice, owing to the strong vortex pinning found in most pnictide samples which led to a disordered vortex lattice upon investigation (Inosov et al., 2010). As such, they provide an important contribution to the ongoing investigation into this class of superconductors. The temperature and field dependencies of the vortex lattice form factor investigated for B applied parallel to **c** provide some interesting insights into the electronic structure of KFA. Firstly, the largely isotropic hexagonal lattice observed throughout the experiment suggests any anisotropy of the superconducting properties in the **ab** plane of the crystal must be small, and we can rule out *d*-wave symmetry in the order parameter from the absence of any transition of the vortex lattice to a square or rhombic structure. Secondly, the variation of the VL form factor with applied field suggest an absence of multi-band effects in the material. Finally, the presence of quasiparticle excitations down to a small fraction of T_c suggests either nodes in the Fermi surface, or a range of gap values at least one of which must be small. This leads us to propose the most likely candidate for the gap structure of KFA to be a nodal gap, with non-local effects being important, where the nodes take the form of line nodes circulating around the $\mathbf{k}_z$ direction of the Fermi surface sheet. The behaviour of the vortex lattice when the field is applied at an angle to the **c**-axis demonstrates the difference between the superconducting properties of the material in the basal plane when compared to those running along the **c**-axis, finding an anisotropy factor for the effective mass ratio in anisotropic London theory of around 3.5. This suggests that the Fermi surface possesses a reasonably two-dimensional character.

2.3.4 Further Work

Whilst it seems unlikely that we would find any structure transitions of the VL in KFA in the remaining field range, there is still much of the VL phase diagram left to explore. Given the low H_{c2} of KFA, we are presented with a rare opportunity to map out the complete VL phase diagram with SANS, something which is not possible with other pnictides or the cuprate superconductors owing to technological limitations of magnets for use on neutron scattering instruments. We also note that the temperature dependence of the VL form factor has only been investigated at low fields, and it would be useful to look for a field dependence to its behaviour.

It was noted that the structural variation of the vortex lattice as a function of rotation angle in the (110) direction detailed here at low temperatures, and the high temperature results presented alongside it in the work by Furukawa *et al* (Kawano-Furukawa et al.,

2013) show a significant difference in the VL structure as a function of angle. It is interesting to note that geometrical arguments, discussed in a paper by Laver *et al* (Laver and Forgan, 2010), *demand* singularities in the vortex structure as the crystal lattice and applied field are rotated. Here, it seems, we have an interesting interplay between the demands of a universal geometric phenomenon which is forcing the VL to undergo a structural transition and the local physics in KFA which seem able to determine its precise location. It would be interesting to map out the behaviour of this structural change as a function of temperature and rotation, which may bring out further information regarding the anisotropic electronic structure of KFA.

2.4 $\mathbf{BaFe_2(As_{1-x}P_x)_2}$

$BaFe_2(As_{1-x}P_x)_2$ (BFAP) is a member of the 122 family of iron pnictide superconductors. Superconductivity is induced by doping the arsenic site of the parent compound, $BaFe_2As_2$, with phosphorous. Arsenic and phosphorous are group 7 elements, both possessing 3 electrons in their outer p shell. This system thus stands apart from cuprate superconductors and many pnictides in that the dopant has the same outer electronic structure as the element it replaces. Superconductivity is found for doping levels of x between ≈ 0.2 and ≈ 0.7 (Jiang et al., 2009), with an optimum T_c of 30 K at $x = 0.32$.

The crystals used in these experiments were doped for optimum T_c. As a second member of the same family, BFAP represented a logical step in a systematic investigation of the iron based superconductors. With conflicting reports of nodal and fully gapped structures and pairing states (Zhang et al., 2012; Shimojima et al., 2011), measurements of the vortex lattice, with its sensitivity to underlying superconducting symmetries, has the potential to elicit important contributions to the ongoing debate.

2.4.1 Literature review for $BaFe_2(As_{1-x}P_x)_2$

Superconductivity in BFAP is induced from the isovalent doping of phosphorus for arsenic. As such, the addition of phosphorus would not be considered to introduce charge carriers into the system, or alter the occupation of the Fe 3d band, which is considered to be responsible for superconductivity in the pnictides. Its phase diagram, however, is remarkably similar to the heterodoped pnictides such as $Ba_{1-x}K_xFe_2As_2$, where charge carriers are introduced into the Fe-As planes by substitution of atoms in the lattice for those with different outer electron shell occupancy, in a similar manner to the cuprates. In the pnictides, superconductivity can evolve out of a magnetic order for both hetrovalent and isovalent doping, which is not immediately expected given our experience with the cuprates that it is the addition of charge carriers to the system that leads to superconductivity. As with heterodoped pnictides, the parent compound BFA exhibits a spin density wave (SDW) transition. This transition temperature is dependent on doping, with Ye *et al* (Ye et al., 2012) showing samples of $x = 0$, 0.15 and 0.2 having SDW transitions at 137, 100 and 65 K respectively, which leads to complete suppression of magnetic order somewhere within the superconducting phase.

The Brillouin zone of BFAP is known to possess five Fermi surface sheets, consisting of two electron sheets at the corners of the zone and three hole sheets at the centre (Zhang et al., 2012; Ye et al., 2012). Near the centre, or Γ point, of the Fermi surface, two of the hole sheets (α and β) are attributed to the Fe d_{xz} and d_{yz} orbitals with a further sheet (γ) attributed to the Fe d_{xy} band. As with other pnictides, there are electron sheets situated around the corners of the zone (δ and η).

The superconducting gap structure of BFAP is a subject still under debate. Recent ARPES results have suggested that the electron sheets of the Fermi surface are fully gapped, with circular line nodes circulating around one of the hole sheets near the Z point of the Brillouin zone (Zhang et al., 2012). This is in contrast to earlier results, which found a fully gapped Fermi surface throughout their investigation (Shimojima et al., 2011), which was limited to small k_z and may not have been able to access the nodes. Evidence for nodes have been found by a variety of experimental techniques, such as in the penetration depth (Hashimoto et al., 2010b), and thermal conductivity measurements, with results being most consistent with closed nodal loops in the electron pockets of the Fermi surface (Yamashita et al., 2011). NMR results show the existence of a residual density of states at low temperatures in a sample of $BaFe_2(As_{0.67}P_{0.33})_2$, indicating nodes in the gap structure (Nakai et al., 2010). A consistent feature of publications proponent of nodal gap structures is the requirement for a small area of sign reversal on the Fermi sheet possessing nodes, as indicated by inelastic neutron scattering measurements (Ishikado et al., 2011), in order for the system to maintain a high T_c in comparison to other nodal pnictides such as KFe_2As_2. Theoretical calculations have also lent weight to the emergence of a nodal gap structure in BFAP (Graser et al., 2010; Suzuki et al., 2011)

The conflicting picture, so far, of both nodal and anodal systems may be reconciled by the idea that the pnictogen height may act as a switching parameter between pairing states. Calculations suggest that sensitivity of the height of bands which form the γ Fermi surface to the distance between the pnictogen and Fe plane causes a change between high temperature nodeless superconductivity and low temperature nodal states in a variety of pnictides (Kuroki et al., 2009), and the effect of lattice parameter on superconductivity in the the iron based superconductors has been documented experimentally (Mizuguchi et al., 2010). The phosphorus anion is smaller than its arsenic counterpart, introducing a strain into the system upon doping, or chemical pressure (Ye et al., 2012) by varying the pnictogen height in the unit cell of the system. The superconducting transition temperature can be correlated both with the As-Fe-As bond angle (Lee et al., 2008), where it is found in many pnictides that optimum T_c corresponds to the $FeAs_4$ unit forming a regular tetrahedron, and the pnictogen-iron distance (Mizuguchi et al., 2010). For data on the pnictogen height, T_c is optimal at 1.38 Å for a range of pnictides, with a symmetrical fall off in transition temperature either side of this optimal distance. This was seen for both ambient pressure systems, where chemical composition determines the lattice parameter, and data taken under applied pressure. The change of lattice parameters is predicted to change both the band structure and Fermi surface topology of the system (Vildosola et al., 2008; Kuroki et al., 2009; Usui et al., 2012). It has been seen (Ye et al., 2012) that both the hole and electron pockets of the Fermi surface expand upon P doping, with maximum charge carrier density corresponding to optimal doping, indicating that holes and electrons have been introduced into the system. This is, given that phosphorous doping is isovalent, an unexpected observation which may explain the similarities of phase diagrams between isovalently and hetrovalently doped pnictides. One explanation is that the lattice distortions upon doping, caused by the differing Fe-As and Fe-P bond lengths cause localisation of electrons, introducing holes into the system (Wadati et al., 2010; Ye et al., 2012). In contrast, it is also possible that, given doped systems are not stoichiometric, vacancies in the lattice introduced on doping could bring charge carriers into the system (Ye et al., 2012). Ye *et al* note in their work, however, that the low residual resistivity ratio of their samples suggest minimal disorder, lending doubt to this idea. It has also been noted in this system that both isovalent doping and physical pressure produces the same phase diagram (Klintberg et al., 2010).

2.4.2 Sample and Experimental Considerations

SANS experiments were performed on the D11 and D33 instruments at the ILL, the SANS-I instrument at PSI and the CG2 instrument at the Oak Ridge National Laboratory in the USA. Neutrons of a mean wavelength between 5 and 9 Åwere used with a $\delta\lambda/\lambda$ of between 10 and 15 %, depending on the source. Diffraction patterns were imaged in fields of up to 14 T for fields applied perpendicular to the **ab** plane.

Two sample mosaics were used for these experiments on single crystal optimally doped BFAP, with a T_c of around 30 K. The (100) axes of the crystals were co-aligned by eye, under a microscope, along the horizontal and vertical axes of plates of high purity aluminium on which they were mounted using hydrogen-free glue. These plates were stacked, where necessary, along the axis of the beam in the same fashion as with KFA. The larger of the mosaics consisted of about 200 crystals with a total mass of 280 mg,

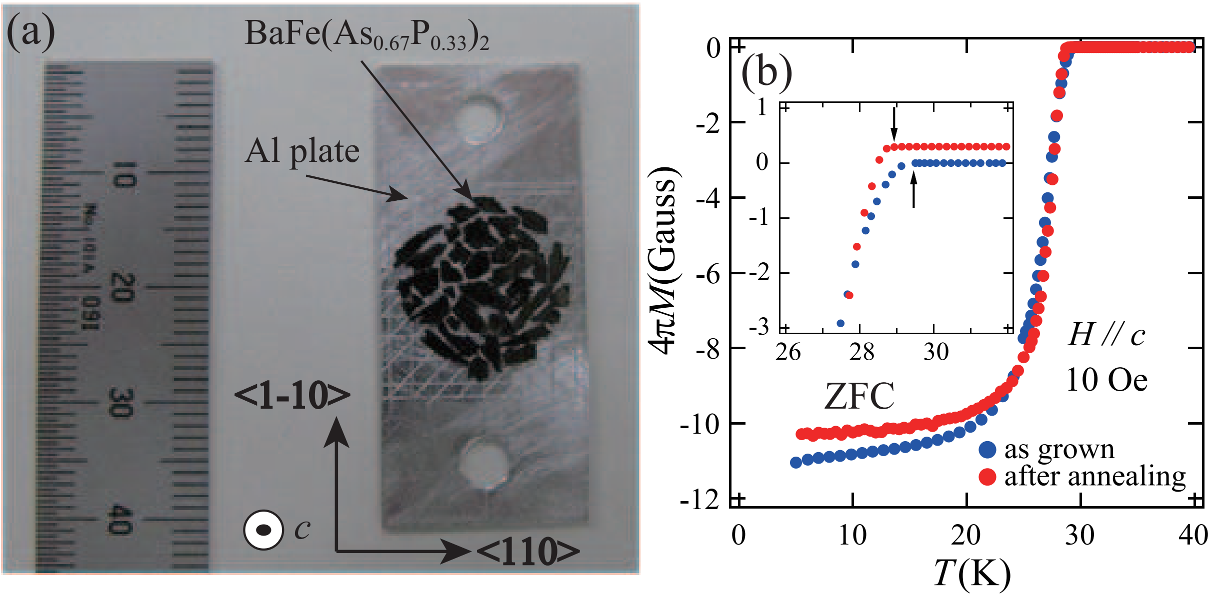

Figure 2.18: a) Picture showing a sample mosaic of BFAP mounted on an aluminium plate. Crystal directions are shown in the figure alongside a scale. b) Magnetisation graphs of the BFAP crystals before and after annealing, with close up of transition point inset showing an improvement in crystal quality after the annealing process. Figure reproduced from (Morisaki-Ishii et al., 2013).

with each crystal having a typical size of $3 \times 3 \times 0.1$ mm. An example of a sample mosaic is shown in fig. 2.18.

Crystals were grown by a self flux method (Kasahara et al., 2010), where mixtures of Ba, FeAs, Fe, P, or FeP powders were sealed in an evacuated cylinder inside an alumina crucible. This was then heated to between 1150 and 1200 °C for 12 hours, and then cooled slowly to around 800 °C. Post growth, crystals were annealed in vacuum at 500°C for 20 hours before SANS measurements were taken, in order to improve crystal perfection and thus pinning forces on the vortex lattice. Susceptibility measurements were performed on these crystals before and after annealing to check for changes in sample quality and showed a reduction in pinning of the flux lines, shown in fig. 2.18.

2.4.3 Field dependence of the VL structure

The vortex lattice structure was investigated at 2 K between fields of 0.05 T and 14 T. Measurements were taken after oscillation field cooling to base temperature and then rocking the sample and applied field through the required angles to satisfy the Bragg condition of the VL. Background measurements, taken at the same field and at 35 K, were then subtracted from the low field measurements to leave behind the signal from the VL. Where appropriate, in order to clarify the patterns when observing as a summed image through all angles, the data was treated with a statistical method to weight the data with appropriate rocking considerations based on Bayes' ideas on probability (Holmes, 2013). This method includes only the data satisfying the Bragg condition on the detector for each result in the sum, thus removing unwanted noise from components of the sum which are far away from the Bragg condition at that point on the detector.

The VL structure as a function of applied field is shown in figure 2.20. Here we see ring-like patterns at very low fields, with defined spots beginning to appear around 0.7 T. Between 5 and 14 T, clear Bragg reflections showing two degenerate hexagonal domains are observed. Whilst it is clearly evident that the vortex pinning below 3 T is enough to bring increased disorder to the lattice, leading to unclear patterns showing no distinct Bragg reflections, it does not dominate to the extent that the lattice is blurred into a ring. However, whilst the rocking curve width of the low field data is wide, data from 0.7 T and upwards show evidence of diffraction spots. This suggests that the lattice is able to obtain a degree of in-plane order, with the dominant disorder being along the length of the vortices (Cubitt et al., 1992). Data at higher fields show narrower rocking curves, seen in fig. 2.19, demonstrating the improvement in lattice quality. At very high fields, from 12 T and above, the rocking curve width in fig. 2.19 widens, perhaps indicating some field induced disorder in the lattice.

At a glance, it may appear that the vortex lattice at 1 T is square in structure, giving this system at least one, if not two, VL structure transitions. However, it is evident in figure 2.20 that this pattern suffers from disorder that blurs the four observed

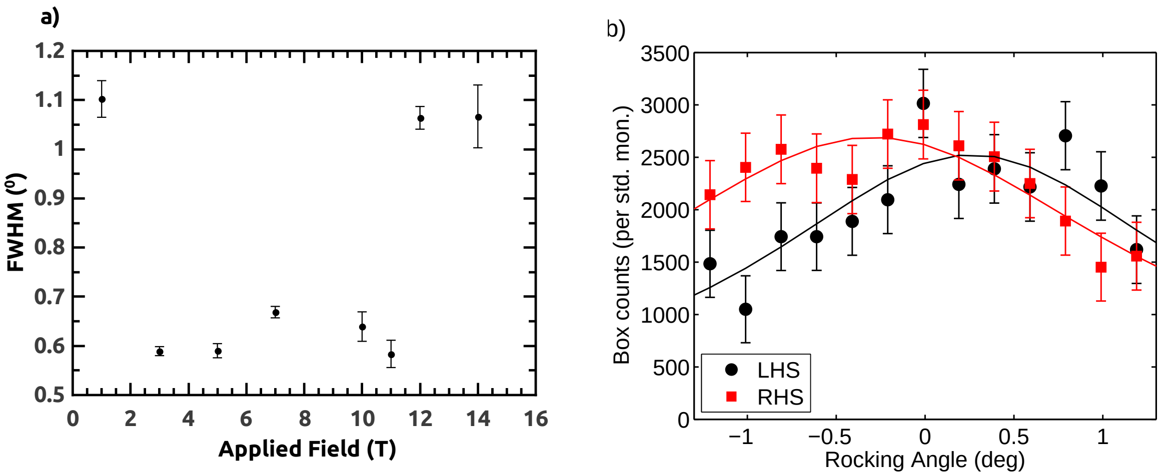

Figure 2.19: a) Figure showing the rocking curve behaviour as a function of applied field between 1 T and 14 T, where analysis of the form factor was possible. b) An example of a rocking curve at 0.3 T, with data from both the left and right side of the diffraction pattern respectively, showing a broad rocking curve. It can be seen that rocking curve widths at lower fields is much wider, with the low field data having a FWHM of around 3 degrees, whilst rocking curve width narrows at higher fields, with some broadening at very high field.

Bragg reflections into spots with a very wide azimuthal occupation. Upon inspection of the experimental scattering vectors, we find that these four diffraction 'spots' have a q of 0.0147Å^{-1}. Contrasting to the expected values of q_{hex} of 0.0148Å^{-1} and q_{square} of 0.0138Å^{-1} we see that these four apparent spots actually hold a scattering vector far closer to a hexagonal lattice than a square, suggesting that they are in fact a combination of diffraction spots from one or more hexagonal lattices blurred by disorder in the lattice, which would explain their large azimuthal occupation.

In light of this, the data appears to show a 45 degree rotation transition around 1 T. The diffraction pattern at 0.7 T shows disordered yet dominant Bragg reflections lined up along the [100] and [010] crystallographic axes that can be attributed to a degenerate pair of hexagonal lattices following the mirror axis running parallel to these crystal axis. The 1 T data shows four very broad spots, attributed to a mid-transition situation frustrated by vortex pinning, whilst the data of 3 T and above show clear hexagonal patterns with mirror axes running along the [110] and [1-10] crystal directions. Whilst exposing details about this transition is made difficult at best by the vortex pinning that is active at low fields, it is perhaps unsurprising that transitions may occur given the complex Fermiology and gap structures that have been proposed for this material (Zhang et al., 2012). Furthermore, this rich environment has the potential to undergo changes with field, evidence for which can be seen in the temperature dependence of the VL form factor, which is to be discussed in a later section.

The anisotropy of the vortex lattice as a function of field is shown in fig. 2.21. Parametrising the anisotropy of the VL in the same manner as with the vortex lattice in KFA, described in section 2.3.1, we can see that the lattice does follow a slight distortion with field but remains reasonably close to isotropic. It was not possible to analyse this information below 3 T, as the blurred diffraction patterns did not allow for the comparison of opening angles. It can be seen that there is a slight deviation as a function of field, with the lattice remaining very close to an isotropic hexagon across the whole accessible field range. Whilst there appears to be a 45 degree reorientation transition at low field, the absence of further structural changes at high field suggest a reasonably isotropic set of superconducting properties as a function of angle about the **c** axis. This behaviour is similar to that noticed in KFA, where the lattice underwent a slight distortion with field with no discontinuity in structure.

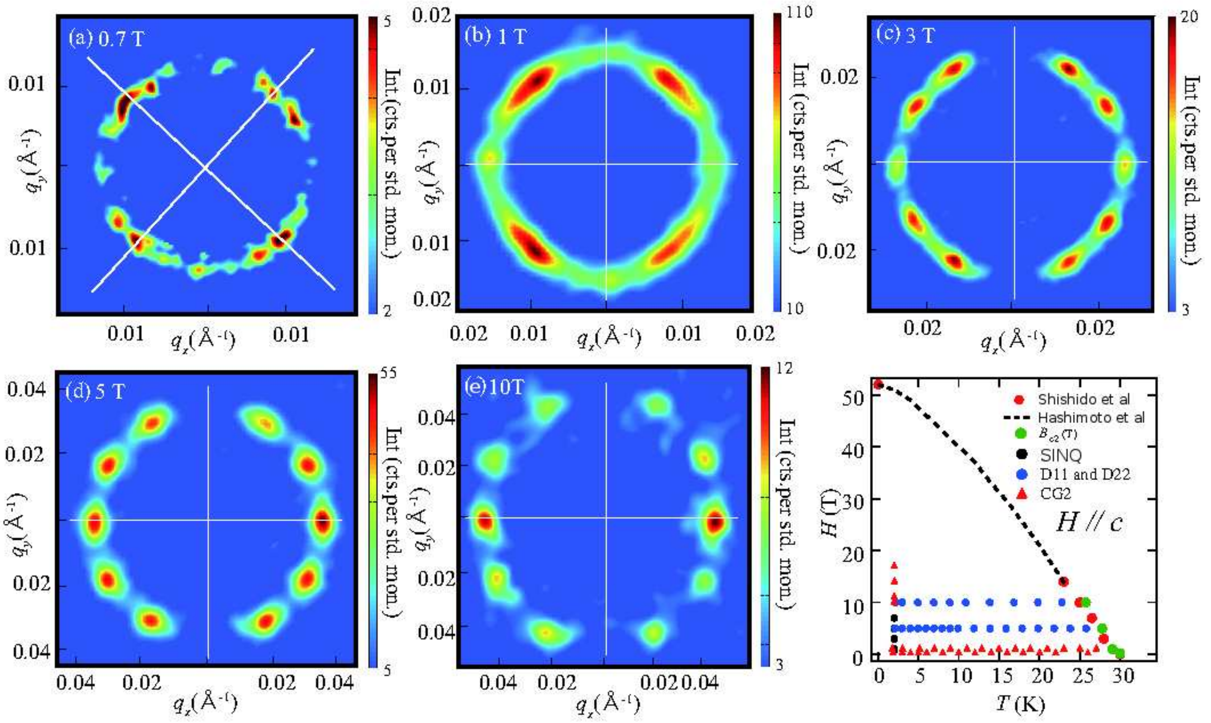

Figure 2.20: Vortex lattice diffraction patterns as a function of applied field for BFAP for a) 0.7 T, b) 1 T, c) 3 T, d) 5 T and e) 10 T, with diffraction patterns taken after OFC to 2 K. Phase diagram shows the location of measured data as a function of temperature and applied field, with a prediction for the $H_c(T)$ line from Hashimoto *et al* (Hashimoto et al., 2010b) and Shishido *et al* (Shishido et al., 2010) indicated. Figure reproduced from (Morisaki-Ishii et al., 2013).

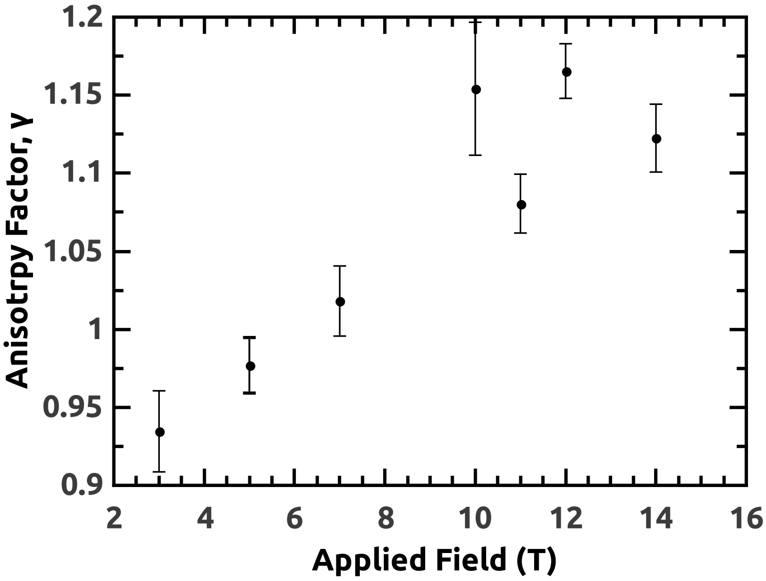

Figure 2.21: Anisotropy factor, defined as the axial ratio of the ellipse on which the diffraction spots lie, as a function of field in the high field phase where distinct diffraction patterns are seen. Data was taken at 2 K after OFC to base temperature.

2.4.4 Field dependence of the vortex lattice form factor

We performed an investigation of the VL form factor as a function of field, shown in fig. 2.22. These results were fitted to the modified London model with core/non-local corrections given in equation 1.28 using a value for c of 0.44, which is considered appropriate for this field range (Yaouanc et al., 1997; Bowell, 2008; White et al., 2011). The results of fitting give values of $\lambda_{ab} = 255 \pm 3$ nm and $\xi_{ab} = 2.85 \pm 0.07$. Our value for λ is longer than that found in previous thermal conductivity studies of 200 ± 30 nm (Hashimoto et al., 2010b) and these results give a Ginzburg-Landau parameter κ of 89.5 for BFAP. From our value for ξ, we calculate an upper critical field of 40.6 T from the relation $B_{c2} = \Phi_0/2\pi\xi_{ab}^2$, which is close to results found by magnetic torque measurements (Shishido et al., 2010). It is possible that the disagreement may be due to distortions of the VL from pinning which result in a static Debye-Waller factor which can lead to an over estimation of ξ in the core correction of the London model. We note, however, that these BFAP results show none of the deviations from the London model with field independent parameters that characterise the behaviour of YBCO in our upper field range detailed in section 3.3.3. However, the VL pinning in BFAP appears less influential than in YBCO, which provides clear diffraction patterns at low field where the VL of BFAP is much more disordered.

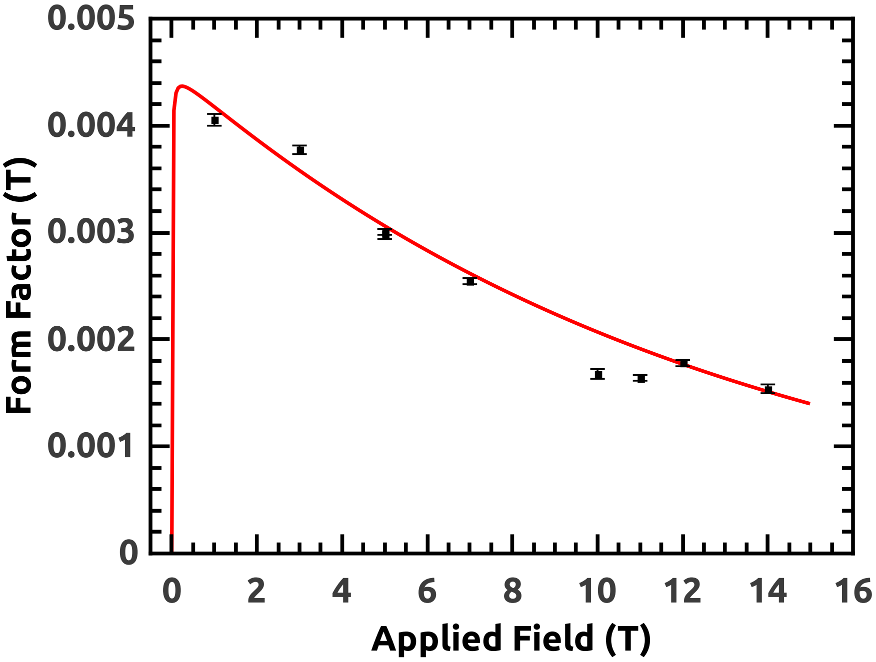

Figure 2.22: Form Factor with field for BFAP at 2 K, fitted to the London model with core/non-local corrections. Using a value of $c = 0.44$, the fit returned values of $\lambda = 255$ nm and $\xi_{ab} = 2.85$ nm.

2.4.5 Temperature dependence of the vortex lattice form factor

The temperature dependence of the VL form factor can provide useful information regarding the gap structure of the system, since the VL form factor is dependent on the superfluid density, which in turn has a temperature dependence governed by the gap structure of the superconducting state. However, given the disorder within the VL of BFAP, leading to wider rocking curves and weaker scattering, experimental time constraints led us to often look at the diffracted intensity at the peak of the rocking curve rather than taking full integrated intensities. In systems with wide rocking curves and weaker scattering, this makes relating the measured intensity to the diffracted intensity difficult, and thus it is not possible to extract absolute values for the form factor. However, under the condition that the rocking curve width does not vary with temperature, the diffracted intensity is proportional to the integrated intensity, and thus the relative variation of intensity as a function of temperature provides us with the same information as would the full form factor variation with temperature. We have taken measurements of both diffracted and integrated intensity, depending on experimental conditions, for fields between 0.2 and 10 T.

We fitted the temperature dependence of the BFAP normalised diffracted intensity to the same simplified gap model as with KFA, since the Fermiology is similar. We therefore retained the approximation that the Fermi surface sheets are cylindrical. After some preliminary tests with the same range of gap models as KFA, it became obvious that neither a single full gap nor single nodal gap would be able to represent the data, so we chose to work with a combination of a single nodal and single full gap. Within the fit, the fractional contribution of the nodal and full gaps and the magnitude of each gap could be varied, and the fits gave a broad minimum in the residuals as a function of these parameters. The statistical accuracy of the temperature dependencies our SANS data is insufficient to constrain a model with a large number of parameters. However, there are changes with field which are represented in the field dependence of the model parameters.

It was found in our analysis of the temperature dependence of the SANS signal in

KFA (Kawano-Furukawa et al., 2011) that a model with horizontal line nodes gives the same ρ_s(T) as a d-wave model. Hence, the temperature dependence of superfluid density can only indicate the presence of nodes, not the detailed gap structure. The full gap was modelled with an s-wave gap and the nodal gap with a d-wave order parameter (with the gap varying with azimuthal angle ϕ, instead of the k_z-dependence of horizontal line nodes). The superfluid density was calculated in the same manner as for KFA, detailed in section 2.2.5. This superfluid density was used to calculate the temperature-dependence of λ, with the absolute values for λ and ξ taken from the London model fit to the field dependence of the vortex lattice form factor in section 2.4.3. The variation in normalised diffracted intensity as a function of temperature was then calculated using the London model with core/non-local corrections given in equation 1.28. To describe the data, we needed to allow the gap magnitudes to vary as well the proportion of full and nodal gaps, which led to problems finding a true minimum at realistic values of parameters. To circumvent this, we fixed the gap magnitudes at pairs of different values and allowed the proportion of full/nodal gaps to vary for each pair of gap magnitudes. The proportion of full to nodal gap was defined by weighting the contribution of each gap to the total superfluid density, normalised to the total weighting. The superfluid density is therefore given by

$$\rho_{total} = \frac{\alpha\rho_{full} + \beta\rho_{nodal}}{\alpha + \beta} \tag{2.13}$$

giving the proportion of nodal gap, γ_n in figure 2.23 as

$$\gamma_n = \frac{\beta}{\alpha + \beta} \tag{2.14}$$

The fitting procedure then used β as a variable, producing a 'matrix' of fit results, showing broad and shallow minima; the results are represented in Fig. 2.23. The data were normalised to the extrapolated intensity at 0 K from fits to the model discussed above.

These fits give broad minima for all temperature dependences as a function of gap magnitudes, although more so for the nodal gap than the full gap. Such broad minima

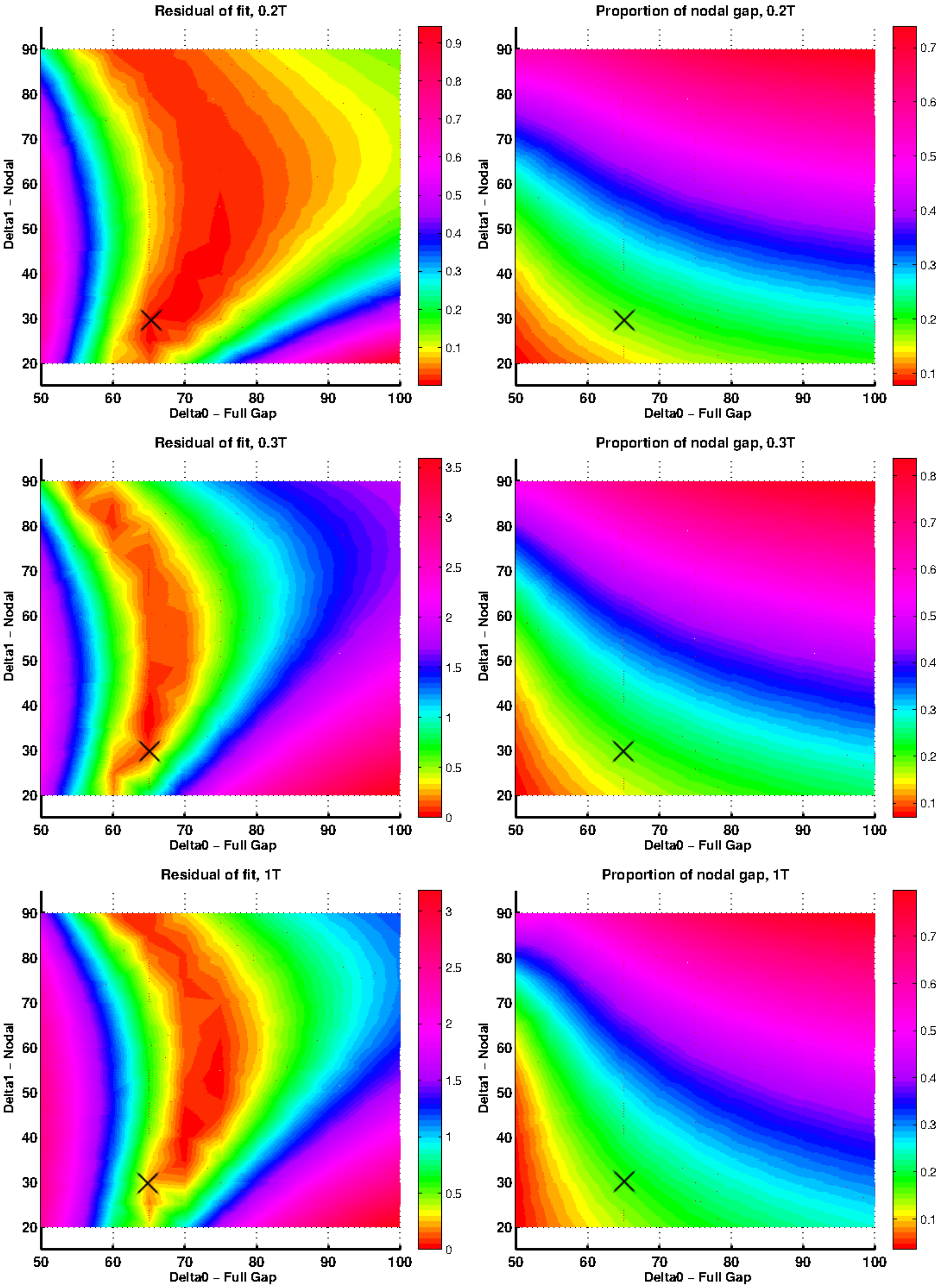

Figure continued on next page.

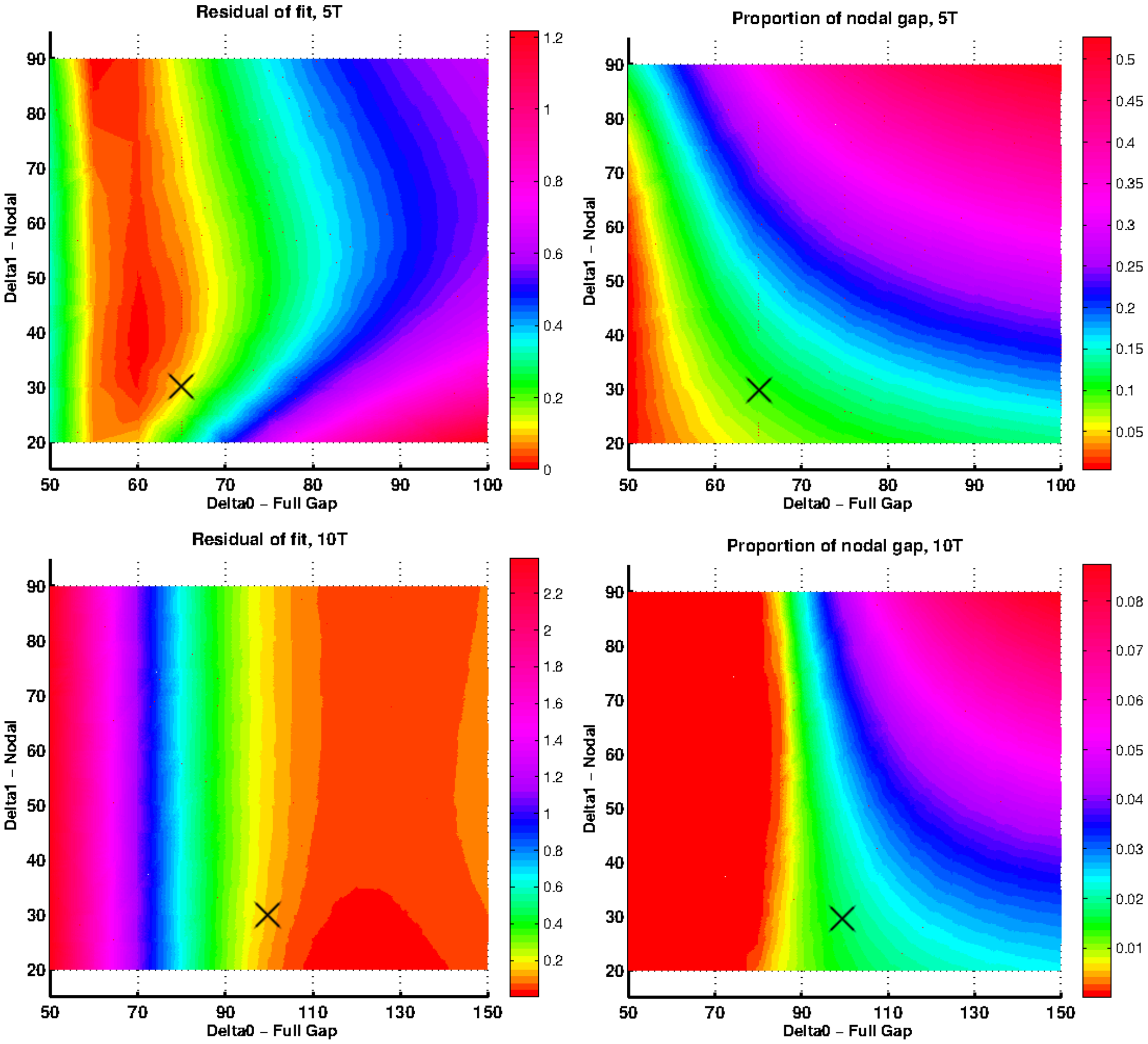

Figure 2.23: Fit results to an array of gap values for the 0.2, 0.3, 1, 5 and 10 T data. Left: Residuals of the fit to an array of gap values, evaluated at a spacing of 5 K. The colour scale is the logarithm of residuals divided by the minimum value. Note the broad minimum, which has little dependence on nodal gap magnitude. Right: proportion of nodal gap given by the same matrix of fits as above. The chosen values for full and nodal gaps for the fits in fig. 2.24, which are listed in table 2.1, are indicated by an X.

indicate that our data is not accurate enough to constrain the model to a high precision, and so it is necessary for us to make some reasonable assumptions about the implications of the results. We note that all fits up to $B = 5$ T indicate the presence of a nodal gap. A field-independent nodal gap value with magnitude of 30 K is reasonable, since it intersects the fit minimum for all fields up to and including 5 T. Secondly, a field-independent full gap value of 65 K is in the 'middle ground' for the 0.2 T to 5 T fits, and avoids non-monotonic variation in the gap magnitude as a function of field. This leads to a proportion of nodal gap of around 0.2 for all fields up to and including 1 T, with 5 T having around 0.1 for the contribution of the nodal gap. This trend of a decreasing nodal gap at high field is continued to the 10 T data, where the model seems able to fit the data with what amounts to a pure full gap. We have chosen to give the 10 T model a full gap magnitude of 100 K, since it is reasonably close to the broad minima around 120 K and our data at 10 T, with the lowest signal to noise ratio, does not have the ability to define a more precise value. Whilst it is possible for all our data to find lower fit residuals in the fits shown in fig. 2.23, doing so results in a non-systematic variation of gap values, and the broad minimum in all fits indicates that the data does not have enough resolution to demand absolute values in this way. As will be seen in figure 2.24, the chosen values of parameters given in the table below give acceptable fits to our measured temperature dependences.

We therefore have a picture of almost field-independent behaviour at lower fields, with a significant change in gap structure at higher fields as the nodal proportion decreases by 5 T and is zero or nearly so at 10 T. This supports the picture of a mix of full and nodal gaps on the various Fermi surface sheets of BFAP, with the smaller nodal gap being suppressed with increasing fields. This may represent a true disappearance of the nodal contribution to the gap, or the increasing importance of non-local effects at high field, since these would also suppress the linear temperature dependence at low temperature. Since the resolution of our data is insufficient to constrain the present model, further parametrisation to represent the influence of non-locality would be unable to produce

Field (T)	Full Gap (K)	Nodal Gap (K)	Prop. Nodal (±)	T$_{c2}(B)$ (K)
0.2	65	30	0.2(0.05)	30.0
0.3	65	30	0.2(0.03)	29.5
1.0	65	30	0.2(0.03)	28.5
5.0	65	30	0.1(0.04)	27.0
10.0	100	30	0.0(0.04)	26.0

Table 2.1: Table showing the chosen parameters from the BFAP temperature dependence fit to a nodal + full gap model.

useful results, so we are unable to distinguish between suppression of nodal behaviour and the increasing importance of non-local effects.

Figure 2.24 shows the temperature dependence of diffracted intensity alongside the fits to the full + nodal gap model with gap values and proportions corresponding to those in the table 2.1. Experimental **q**-vectors were used in the calculation of the normalised intensity, and we can see that these provide a reasonably good fit to all the data. However, as is illustrated in the wide fit residuals of figure 2.23, and the reasonably large errors on the proportion of nodal gap in table 2.1, the data is not of sufficient resolution to strongly confine the available parameters.

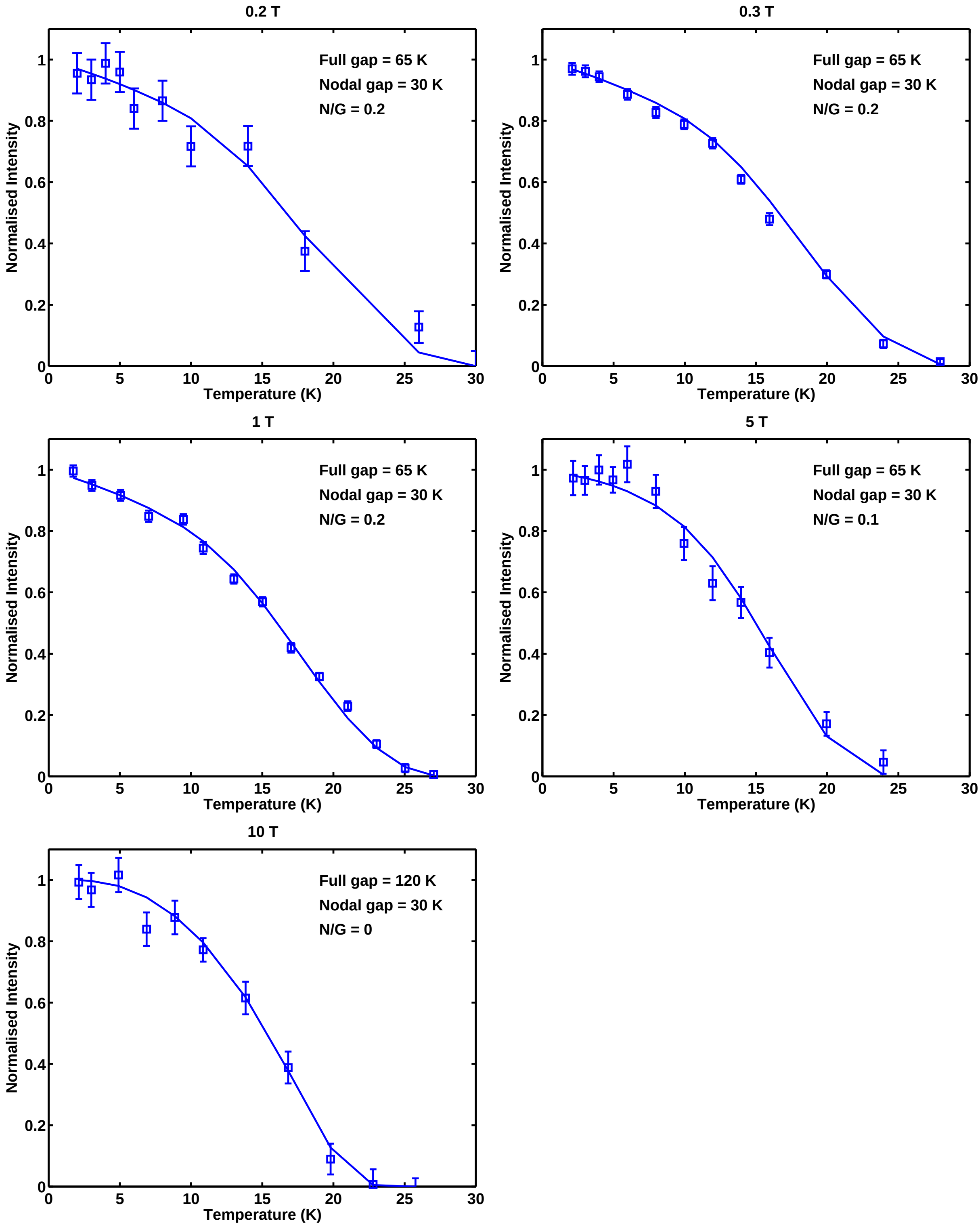

Figure 2.24: Fits to temperature dependence, with gap values and proportions set to those in the table. Data has been normalised to the extrapolated intensity at zero temperature. T_c(B) is taken from figure 2 in our paper.

2.4.6 Discussion

Our results on the field and temperature dependence of the vortex lattice properties in BFAP suggest several important findings. Firstly, the low field temperature dependence shows a good fit to a model comprised of both a full and nodal gap. The balance between nodal and full gap contributions changes at higher fields, with the nodal contribution being suppressed with increasing field. Whilst a 45 degree rotational transition is observed, the absence of a transition to a square structure at high fields rules out a *d*-wave nodal parameter. This structural rotation transition roughly corresponds to the field region where the temperature dependence suggests the nodal contribution is being suppressed, arguing that a field-driven gap change is the origin of this transition. The absence of square symmetries in the lattice or a $\mathbf{q}$ vector corresponding to a square lattice at any point in our data suggests that the gaps must be reasonably symmetric as a function of angle around the $\mathbf{c}$ axis in a similar manner to the gap structure in KFA. Our conclusion is therefore that the nodal contribution to our gap structure takes the same form as our proposed gap structure for KFA - a horizontal ring-like node around one of the Fermi surface sheets.

Our results, suggesting a nodal state in at least one gap on the Fermi surface sheets of BFAP, support an observation that nodes exist in the iron-pnictides when the distance between the iron and the pnictogen is less than 1.33 Å (Kuroki et al., 2009). Given that the VL of BFAP tends towards hexagonal, rather than fourfold symmetry at high field, a *d*-wave state can be ruled out. The nodal behaviour in the temperature dependence, coupled with the hexagonal symmetry at high field supports a horizontal ring-like node structure as has been proposed in pnictides before (Kawano-Furukawa et al., 2011; Zhang et al., 2012).

It is expected that the emergence of nodes in the system will lead to a significant reduction in T_c. However, BFAP retains a respectable transition temperature when compared to its fully gapped relative $\mathrm{Ba}_{1-x}\mathrm{K}_x\mathrm{Fe}_2\mathrm{As}_2$ (Hashimoto et al., 2009; Evtushinsky et al., 2009). This broken expectation may very well be due to the presence of both full and nodal gaps in BFAP, suggested by these results and previous investigations, leading to evidence of nodal behaviour with a T_c more reflective of a gapped system. Furthermore, it has been previously noted that horizontal line nodes in the pnictides seem to result in a very small area of sign reversal of the gap, helping the system retain a T_c more indicative of its fully gapped relatives (Ishikado et al., 2011).

Calculations modelling the VL morphology of unconventional superconductors have shown that first order structure transitions consisting of a 45 degree rotation can occur in fourfold superconductors with an anisotropic Fermi velocity (Suzuki et al., 2010). The work, by Suzuki *et al*, finds the transition appearing irrespective of the magnitude of their anisotropy parameter β, which characterises the anisotropy of the Fermi velocity as a function of angle around the basal plane, where $0 < \beta \leq 1$, for both non-local London models and calculations based on Eilenberger theory. Although in calculating the temperature dependence of the form factor we assume that the Fermi surface sheets in these materials are cylindrical, band structure calculations and ARPES results have indicated that the Fermi surfaces in these materials are not entirely two dimensional or isotropic (Mazin and Schmalian, 2009). It is therefore possible that anisotropies in the Fermi velocity play a role in this transition, although at present we find no published work discussing the precise VL structure which may result from the Pnictide systems. It is also possible that non-local effects play a role in this transition, since they become important in nodal systems.

2.4.7 Conclusions

These SANS results on BFAP provide an important contribution to the ongoing debate on the gap structure in this material. We have seen clear indications of nodal behaviour in the temperature dependence of superfluid density, leading us to believe that there must be at least one Fermi surface in the material whose superconducting gap possesses nodes, which supports recently published ARPES results, among others, which find indications of nodal gaps in this material (Zhang et al., 2012). Further, we see that the temperature dependence of the VL form factor at higher fields indicates the absence of quasiparticle excitations at low temperature, indicating a field driven change in the gap structure. Whilst the vortex lattice at low field is highly disordered, and we find a 45° rotation transition with increasing field, the absence of a transition in the vortex lattice structure to a rhombic phase leads us to draw the same conclusion regarding the nodes in the gap as with KFA: the gap must take the form of a horizontal line node around the $\mathbf{k}_z$ direction of the Fermi surface.

2.4.8 Further Work

As a material with a strong anisotropy between the basal plane and the **c** axis, investigating the behaviour of the VL as the applied field is rotated away from the **c** axis provides us with a tool with which to investigate this anisotropy. In a similar manner to KFA, we would expect a distortion of the VL which is governed by the basal-plane-to-**c**-axis anisotropy, allowing us to investigate this further. In addition to this, with strong indications of a rich Fermiology and nodal gap structure changing the anisotropy experienced by the VL may yield additional information about the underlying superconducting state of BFAP. With a disordered VL at low field, further annealing of the crystals may improve the VL pinning and allow for a more precise investigation of the low field behaviour. In addition, with indications of a field driven change in the gap structure, it would be useful to investigate the temperature dependence of the vortex lattice form factor for fields above 10 T. We are, however, limited by the small signal to noise ratio in this region, and it would take an extended period of experimental time on an instrument with an equivalent neutron flux to the SANS instruments at the ILL, or a significantly larger sample. With our data indicating that at 10 T it is difficult for us to gain the resolution required to make any definitive estimation of the behaviour of the gap structure, it seems that investigation at high fields would be difficult.

A useful avenue of investigation to continue this research would be a similar study on a sample of $\mathrm{BaFe_2(As_{1-x}P_x)_2}$ where the doping parameter x, which sits at $x = 0.32$ for our sample, was varied across the available range of superconductivity. Whilst this results in a lower T_c, we may find different behaviour as charge carriers are either introduced or removed from the system. With BFAP being one of only two superconductors to produce clear SANS results, it is important to investigate the behaviour of this group, since SANS can provide important information regarding anisotropies of the gap structure and Fermi surface, which may evolve with doping. Whilst we may find increased pinning in the sample, the presence of an ordered VL is one member of this group is a promising indication that other members of this group may also be able to produce clear SANS results.

CHAPTER 3

YBCO

Superconductivity was first observed in a cuprate material in $(La_{1-x}Ba_x)CuO_4$ in 1986 (Bednorz and Muller, 1986), with a critical temperature of 35 K. As a marked increase from previously observed critical temperatures this sparked an investigation into other cuprates, with superconductivity being discovered in $YBa_2Cu_3O_{7-\delta}$ (YBCO) in 1987 (Wu et al., 1987) with a composition-dependent T_c of between 80 and 93 K, along with others such as $Bi_2Sr_2Ca_nCu_{n+1}O_{2n+6-\delta}$ (BSCCO) with critical temperatures exceeding 100 K (Maeda et al., 1988). This marked a departure from the BCS prediction of a T_c maximum of between 30 K and 40 K, and demonstrated the existence of critical temperatures above 77 K, the boiling point of liquid nitrogen. As a cryogen, it is cheaper and easier to manipulate than liquid helium, as well as being far more abundant. This made experimentation on these materials easier, as well as opening up the possibility of technological applications that would previously seemed infeasible. The cuprates also provided a host of challenges to our understanding of superconductivity, which ensured that these materials have remained the subject of continued investigation to this day. This chapter presents a SANS investigation into the behaviour of $YBa_2Cu_3O_7$, the fully over-doped member of the $YBa_2Cu_3O_{7-\delta}$ family.

3.1 Literature review

3.1.1 Crystal structure

The crystal lattice plays the pivotal role in determining the superconducting properties of any system. In the specific case of $YBa_2Cu_3O_{7-\delta}$, where the doping parameter for oxygen content can vary between 0 and 1, the un-doped parent compound has $\delta = 1$, with superconductivity emerging in the system as δ is decreased. YBCO has crystal structure composed of a repeating set of poly-layers, shown in figure 3.1, with planes consisting of yttrium, barium oxide, copper oxide or copper dioxide. For $\delta = 0$, there is no distinction between the crystallographic **a** and **b** axes, and thus the system possesses a tetragonal structure with an occupancy of a single 'free' electron per unit cell. At low doping, the oxygen atoms randomly disperse themselves between the Cu ions lying between the BaO planes. However, the randomness of this dispersion ceases (at $\rho = 0.04$), which coincides with the emergence of superconductivity, and the oxygen atoms preferentially occupy sites between Cu ions along the **b** axis.

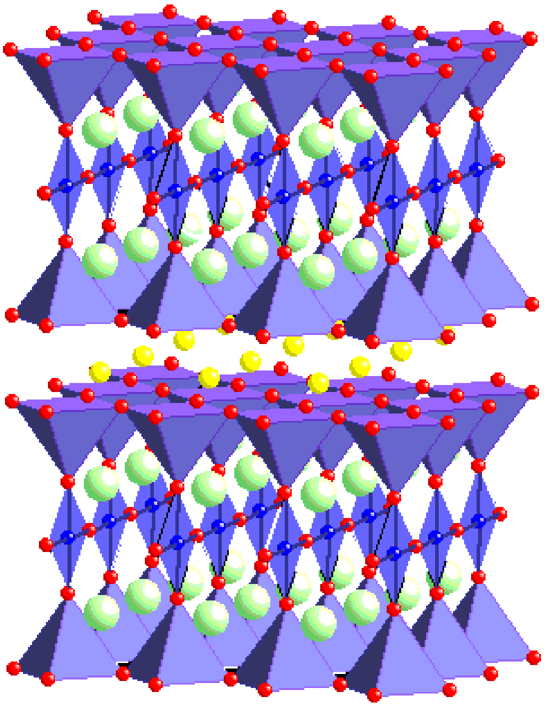

Figure 3.1: Crystal structure of $YBa_2Cu_3O_7$, where copper is given in blue, oxygen in red, barium in green and yttrium in yellow. (Heyes).

The ordering of the oxygen atoms into chains along the **b** axis results in the **a** and **b** axes no longer being equivalent. This causes a transition to an orthorhombic lattice, which also brings rise to crystallographic twinning; a phenomenon found to have an enormous effect on the flux lattice, which will be discussed later. At high temperatures, the oxygen atoms remain disordered, but on cooling the atoms undergo ordering at a temperature between 400-675° C (Lin et al., 1992). During this process, in order to maintain its macroscopic structure, regions of the crystal flip their **a** and **b** axes. This, illustrated in fig. 3.2, happens periodically throughout the crystal on a length scale which is variable between samples. The regions where the **a** and **b** axes flip are known as twin planes, which run at 45° to the Cu-O bonds in the CuO_2 planes. It should be noted that the highly simplified picture of twinning in figure 3.2 does not illustrate the shear angle between the two domains within the crystal. With **a** and **b** being unequal, it is impossible for them to flip by 90° within the boundary constraints of parallel twin planes. The domain will therefore offset itself by a small angle to accommodate this.

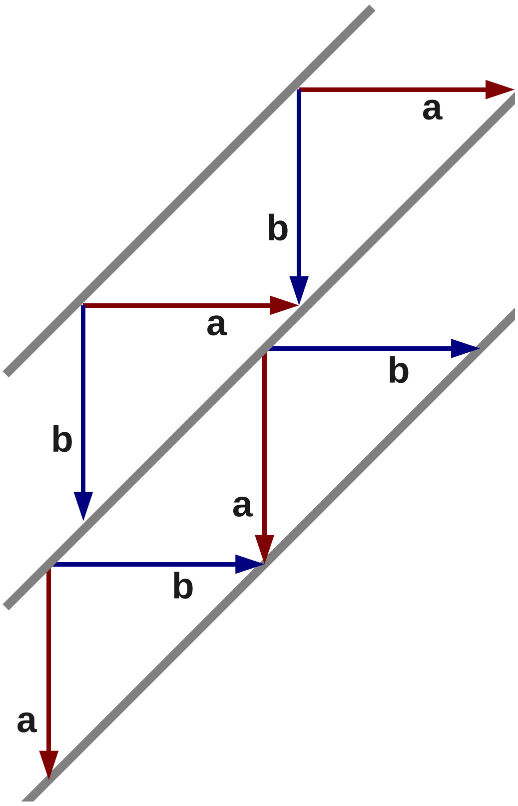

Figure 3.2: Figure showing a simple representation of crystallographic twinning. At the periodic twin plane boundaries, shown in grey, the orientations of the **a** (red) and **b** (blue) axes switch.

The CuO_2 plane is the common unit of all cuprate materials, and it is electronic states associated with these planes that become superconducting. It was identified early on in research on the cuprates that the oxygen doping which controls the emergence of superconductivity relies on a charge transfer between the copper oxide planes and the other layers in the crystal structure (Anderson, 1987). YBCO gives a reasonably complicated picture of the relation between charge transfer, critical temperature and oxygen content, owing to the relation between ordering of the copper oxide layers into which the oxygen doping occurs and the charge transfer as result of the doping. With the Cu-O bonds in this layer running along the crystal **b** axis, and no corresponding bonds along the **a** axis, these are referred to as copper oxide chains. The doping parameter δ corresponds to a filling or emptying of the oxygen sites along these chains, with certain oxygen doping giving rise to ordered chain superstructures, the simplest forming around $YBCO_{6.5}$ where the chains alternate between being filled and empty. For higher oxygen doping, fully occupied/unoccupied chains form more complicated sequences along the **a** axis, with superconductivity in these systems being very sensitive to the ordering of oxygen atoms in these superstructures. The CuO chains are, to a good approximation, 1D systems and so inherently sensitive to the effects of disorder and as such fragmentation of these chains from oxygen disordering has been found to suppress the superconductivity (Jorgensen et al., 1990). This can be attributed to reduced hole doping, arguing that ordered chains are able to contribute holes to the CuO_2 planes whereas disordered oxygen distributions of the same number of atoms are not. In contrast, it could be argued that charge is localised in disordered systems or as a result of electrons scattering off dislocations which arise from the disorder. In $YBCO_{6.5}$, disruption of the chain order has been seen to suppress T_c by around 6 K, with superconductivity in $YBCO_{6.4}$ being completely suppressed by such disorder. Due to disorder in these systems having high dependency on sample preparation, this can lead to an irreproducibility of results between samples. Annealing samples at just above room temperature can help reduce disorder, which was noticed in a long scale time dependence of T_c in early samples.

3.1.2 Electronic Structure and Magnetic correlations

The CuO_2 planes are the common unit of all cuprates, and are generally considered to possess the electronic states responsible for the interesting physical phenomena that have attracted so much attention in the last 26 years. In the absence of doping, where $\delta = 0$, the Cu^{2+} ions in the copper dioxide planes possess 9 electrons in their 3d shell. The degeneracy, however, of this shell is broken, leaving 8 electrons paired off with a single electron left in the higher energy $d_{x^2-y^2}$ orbital. It strongly hybridises with the $2p_{xy}$ orbitals of the O^2- atoms within the CuO_2 layer to form three bands, corresponding to bonding, non-bonding and anti-bonding orbital configurations.

Band structure calculations on the CuO_2 plane predict the bonding and non-bonding bands to be full (Damascelli et al., 2003), with a half filled anti-bonding band at the Fermi energy. For a single CuO_2 plane we therefore have one electron per unit cell that we might expect to act as a charge carrier. In the absence of interactions it should de-localise and the planes would show metallic behaviour. However, the parent compounds of cuprate superconductors are Mott type insulators, in this case displaying commensurate antiferromagnetism with $S = \frac{1}{2}$. This system has a large on site repulsion energy, originating from the Cu^{2+} ions, and the lowest energy excitation is of the order of the charge transfer energy, characterising this to be a charge transfer insulator (Zhang and Rice, 1988; Zaanen and Gunnarsson, 1989). The insulating nature of our parent compounds explains the necessity for doping to bring about superconductivity; without the charge doping that oxygen offers, the CuO_2 planes will, from a charge carrying perspective, remain 'full'.

Fig 3.3 shows the phase diagram as a function of hole doping and temperature. From the perspective of a Mott insulator, this offers a mechanism for the insulating behaviour to break down, as transfer of holes into the planes provides 'spaces' into which charge carriers can move. It was proposed by Anderson (Anderson, 1987) that quantum fluctuations in a 2D system such as the cuprates may be enough to destroy long range antiferromagnetic order. This would result in a spin liquid, containing electron pairs that have anti-parallel alignment of their spins. Anderson noted that the motion of these singlet pairs is similar the resonance of the π bond in Benzene - know as resonating valence bonds (RVB), which resemble the Cooper pairs in BCS. It was proposed that the parent compounds of cuprates act like a suppressed BCS state, with electrons coupled in pairs but with no vacancies to travel to. The adding of holes to the CuO_2 plane with doping would create the required vacant sites, allowing superconductivity to appear. However, experiment shows that the spin liquid system is not realised in the cuprates, and the antiferromagnetic order has a Néel temperature of up to 400 K (Orenstein and Millis, 2000). With increased doping, interactions between the doped holes and the Cu spins allow the holes on the copper sites to de-localise, reducing the stability of the antiferromagnetic phase and, correspondingly, its Néel temperature. When the system reaches a doping level of $7 - \delta = 6.3$, the antiferromagnetic state collapses and the copper oxide planes become more metal like, and eventually superconducting at low temperature. As a prelude to the superconducting phase the cuprates pass through the pseudogap regime, which will be discussed later in section 3.1.4.

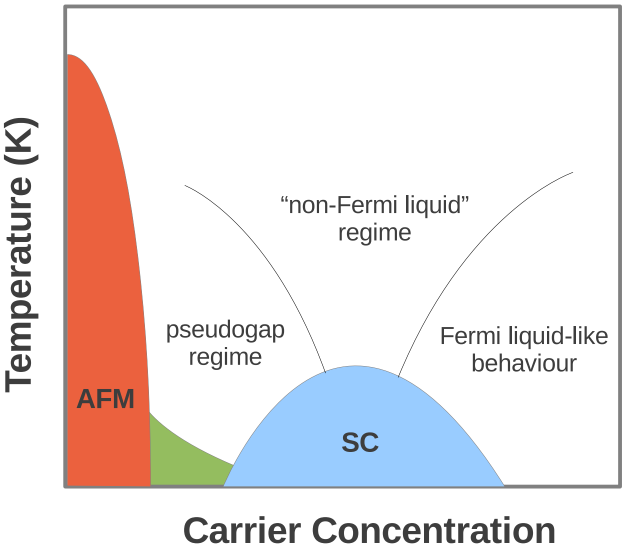

Figure 3.3: Doping and temperature phase diagram of the cuprate superconductors, showing the commensurate antiferromagnetic regime (red) of the parent compounds give way with increased doping to more exotic magnetic behaviour (green), which leads to the superconducting phase (blue).

Antiferromagnetic correlations are still thought to exist in the cuprates beyond the collapse of the Néel state with increased hole doping. The remaining magnetic correlations, indicated in the green region of fig. 3.3, are incommensurate in nature with intermediate levels of doping leading to a spin glass, whilst the magnetic behaviour at higher doping levels being dependent on both system and quality of the sample. Whilst it is surprising that magnetic correlations push into the superconducting regime, an explanation has emerged which has undergone significant investigation in recent years: the concept of inhomogeneous charge and spin ordering regions, known as stripes. These were first noticed in neutron scattering investigations into magnetic behaviour as a function of doping (Mason et al., 1992; Cheong et al., 1991). The two sub-lattice structure of the Néel leads to antiferromagnetic Bragg peaks at $Q = \pm\frac{1}{2}$, which was seen to broaden and and split into 4 incommensurate peaks displaced from Q_{AFM} by a small amount δ. These were explained by spins that are locally commensurate, but who jump in phase by π at a periodic domain wall known as an anti-phase boundary (Tranquada et al., 95, 1997). Stripes are not predicted from Fermi liquid theory (Zaanen and Gunnarsson, 1989; Schulz, 1990), however we have seen that the under doped cuprates engage in a significant departure from Fermi liquid behaviour. Furthermore, recent X-Ray scattering results have shown that stripes are not involved in YBCO, instead reporting a charge density wave forming with a critical temperature of around 150 K (Blackburn et al., 2013).

We now have a picture of high T_c cuprate materials as being poor conductors, especially in the under-doped region, and that they are more commonly regarded as doped antiferromagnets. The stark difference between these systems and Fermi liquid behaviour renders the BCS description, developed for superconductivity emerging out of metal-like states, somewhat inappropriate. As doping increases, the antiferromagnetic correlations decrease and eventually give way to systems with connected Fermi surfaces. Superconductivity in YBCO has an optimal doping level of $7 - \delta = 6.93$, with higher doping reducing T_c. This is therefore referred to as optimally doped, defining the under-doped and over-doped regimes seen on the phase diagram. There is a great deal of interest in the behaviour of the cuprates on the under-doped side of the phase diagram, with questions still being asked about the structure and evolution of the Fermi surface with doping and nature of what is known as the 'pseudogap' phase above T_c. The over-doped side of the phase diagram seems, at a glance, more straightforward with physics consistent with a Fermi liquid like behaviour and the material possessing coherent Fermi surfaces. However, upon closer inspection deviations from Fermi liquid behaviour are observed. This has led to models describing these states as 'marginal Fermi liquids' (Varma et al., 1989) or as a 'strange metal' (Anderson, 1995). Whilst it is beyond the scope of this thesis to delve into the theoretical descriptions of the high T_c cuprates' departure from Fermi liquid theory, it is clear that we can expect some behaviour, such as the presence of Fermi surface above T_c, to be similar.

3.1.3 Superconductivity

Superconductivity in the high T_c cuprates was discovered in 1986 by Bednorz and Muller (Bednorz and Muller, 1986) in $(\mathrm{La}_{1-x}\mathrm{Ba}_x)\mathrm{CuO}_4$, and since then has been found in a range of other cuprates. Like the conventional superconductors discovered over the previous 75 years, in the cuprates superconductivity is characterised by an order parameter ψ giving the probability amplitude for finding electrons in the paired state. Whilst for conventional s-wave pairing the Fermi surface is fully gapped, the order parameter in the cuprates possesses d-wave symmetry, changing sign upon a 90° rotation and therefore having nodes, or zero gap magnitude. In tetragonal systems, the nodes fall at 45° to the Cu-O bond in the CuO_2 planes (Tsuei and Kirtley, 2000). This defines the cuprates as unconventional superconductors, and with such a remarkable difference between this pairing state and the classical superconductors it is important to ask if these superconductors can be described by a modified BCS theory. Whilst the rich phase diagram of antiferromagnetic insulators evolving into superconductors with regions of stripe order and non Fermi liquid like behaviour suggest a more novel state, the low energy excitations of the system seem to follow BCS behaviour (Sachdev, 2000). Here, the nodal quasiparticles from d-wave BCS are expected to have a Dirac spectrum, $\epsilon = vp$, with anisotropic Fermi velocity for momentum perpendicular and parallel to the Fermi surface, giving a quasiparticle dispersion with the shape of an anisotropic cone. The corresponding density of states is linear in energy (Orenstein and Millis, 2000), as the range in ϕ of quasiparticle excitation is proportional to $k_B T$. This quasiparticle spectrum was first confirmed in the observation of linear dependence with temperature of the superfluid density by Hardy et al (Hardy et al., 1993), and subsequently by other measurements such as ARPES data on BSCCO (Ding et al., 1996).

The quasiparticle lifetime, however, is a more difficult question to answer when looking for conventionality in the cuprates. BCS based calculations predict T^{-3} or stronger power behaviour at low temperature, which looked to be found in samples of YBCO from microwave absorption measurements (Hirschfeld et al., 1993). Here, they found a T^{-4} behaviour in the transport lifetime which is in agreement with the BCS prediction. ARPES measurements on BSCCO, however, observed a T^{-1} increase in quasiparticle lifetime as the temperature was reduced below T_c, which is a continuation of the normal state behaviour, and indicates that the nodal quasiparticles may not be strongly affected by the emergence of superconductivity. This suggests that the ground state may not be BCS-like and that the quasiparticles feel strong fluctuations at low energy, which would be expected near a quantum critical point (Sachdev, 2000). It may be, however, that the nodal quasiparticles are more strongly scattered in BSCCO than YBCO, which could account for this behaviour and is supported by thermal conductivity (Krishana et al., 1997) and ac transport (Lee et al., 1996; Jacobs et al., 1995) measurements. Whilst the differences at low temperature may be explained by sample quality, these conductivity measurements should not be so sensitive to crystal quality at high temperature as the dominant scattering process is inelastic.

3.1.4 The question of the pseudogap

In the earlier sections, we explored how superconductivity emerges out of an insulating antiferromagnet, and questioned the form it took and how this differed from the conventional superconductors. Here we ask the question of how superconductivity is destroyed, and perhaps unusually, what remains behind after either temperature or doping has taken us out of the superconducting state. In the under-doped cuprates, Uemura et al (Uemura et al., 1989) found that T_c is proportional to ρ_s, or phase stiffness, in many under-doped cuprates. A superconductor has two energy scales: the BCS gap, Δ, which measures the strength of the Cooper pair binding, and the phase stiffness, ρ_s, which is a measure of how robust the superfluid is to carrying a supercurrent (Emery and Kivelson, 1995). For the conventional superconductors, the gap is much smaller than the phase stiffness, and as such the breaking of Cooper pairs is responsible for the destruction of superconductivity. In the unconventional high T_c cuprates, however, it seems that the two energy scales are reasonably equivalent. For the under-doped cuprates, the phase stiffness is now the smaller of the two energy scales and so is overcome by $k_B T$ faster than the Cooper pair binding, resulting in the loss of phase coherence marking the end of superconductivity.

With the loss of long range phase coherence marking the end of superconductivity, we expect upon warming above T_c to see a region with short range phase coherence, finite in both space and time. This is seen in the frequency dependence of the phase stiffness of the system above T_c (Corson et al., 1999). At low frequency, the phase stiffness is seen to be zero, as expected for a normal state system. However, the phase stiffness is seen to return in ac conductivity measurements on BSCCO when the frequency passes above the maximum de-phasing rate, which is around 1 THz (Corson et al., 1999). This frequency dependent regime is seen to last till about 20 K above T_c, whereupon the system enters an incoherent regime.

It is in this region of the phase diagram - the incoherent regime above T_c in the underdoped materials - that the d-wave pseudogap is observed (Shen and Dessau, 1995). Here, parts of the Fermi surface are gapped in regions corresponding to the antinodes of the d-wave gap, leaving behind arcs of non-connected Fermi surface. This is well documented in ARPES (Damascelli et al., 2003), and the presence of the pseudogap affects some response functions, such as causing a strong suppression of between-plane charge transport (Basov et al., 1994), but not others, such as the in-plane charge transport (Orenstein et al., 1990).

3.1.5 The Vortex Lattice in the cuprates

Vortex lattice studies have provided a wealth of information on the cuprate superconductors. The vortex lattice is very sensitive to anisotropies in the host crystal, Fermi surface or superconducting order parameter, and as a bulk probe SANS is perfectly placed to investigate these effects. For a high κ superconductor, the simplest approximation is for an anisotropic penetration depth to arise from an effective mass anisotropy (Kogan and Miranović, 1997), which will lead to distortions from the ideal triangular lattice. In more complicated situations, a superconducting order parameter which has lower symmetry than the crystal may also express itself in the vortex lattice structure. The observed tendency for d-wave materials is for the lattice to evolve from a hexagonal low field structure to a square or rhombic high field structure, which has been strongly observed in the cuprates (Brown et al., 2004; Affleck and Franz, 1997; Ichioka et al., 1997, 1999; Shiraishi et al., 1999). Non-local effects may also give rise to VL transitions, although these are predominately seen in lower κ materials such as the borocarbides (Paul et al., 1998; De Wilde et al., 1997) or V_3Si (Yethiraj et al., 1999; Sosolik et al., 2003).

Vortex lattice studies on YBCO were initially performed on twinned samples (Brown et al., 2004), where the **ab** crystal anisotropy had forced the crystal to split into alternating domains where the **a** and **b** axes were reversed. The results, at low field, showed an initial configuration with fourfold symmetry - reflecting the average fourfold symmetry of the twinned sample. The local coordination of the lattice was, however, triangular, with a distortion governed by the **ab** anisotropy of the crystal and a VL orientation which was controlled by pinning to the twin boundaries. With increasing field, the vortex lattice was seen to smoothly distort to a near square lattice by 11 T. The change of structure, and alignment of vortices along probable node directions, supported d-wave theories (Shiraishi et al., 1999; Ichioka et al., 1997, 1999), although the non local theory of Kogan et al (Kogan and Miranović, 1997) using an s-wave gap could also predict a similar transition. This was in part agreement and part contrast to investigations into the vortex lattice of $La_{1.83}Sr_{0.17}CuO_{4+\delta}$, where a triangular to square vortex lattice transition with field had also been observed, but with an orientation that was at 45° to these results. The hypothesis in this case was that the symmetry of the VL was being governed by the d-wave order parameter, but the orientation by band structure effects (Gilardi et al., 2002; Nakai et al., 2002). These results were in disagreement with results from an STM study

(Fischer et al., 1997; Shibata et al., 2003a), highlighting the ability of SANS to perform bulk measurements.

3.1.6 Previous investigations into de-twinned YBCO

Many of the results detailed in this thesis form a continuation of the investigations into the flux lattice of YBCO by the Condensed Matter group at the University of Birmingham. Previous measurements were taken in fields up to and including 10.8 T. In order to understand the context in which the present measurements fit, it will be necessary to review the previous data. Figure 3.4 shows the results from the structure investigations undertaken in fields of up to 10.8 T at 2 K. Three distinct structure phases are observed, with the hexagonal lattice observed up to around 6.5 T, with a 90° re-orientation transition at 2 T. By 7.5 T, however, the vortex lattice has undergone a transition to a rhombic phase. This lattice structure was seen to evolve with field continuously until the maximum achievable field of 10.8 T, with the opening angle ν gradually evolving towards, but not quite reaching a square lattice. In the research by White *et al* (White et al., 2009), the structural evolution of the vortex lattice with field was attributed to the influence of anisotropies in the order parameter and Fermi surface. Whilst anisotropic London theory could not predict the observed transitions, non local models which couple the vortex lattice to anisotropies in the Fermi surface predict an analogous transition to the low field 90° rotation (Kogan and Miranović, 1997; Franz et al., 1997). These models approximated the anisotropy to exist either in the order parameter or Fermi surface, with the other taken to be anisotropic, and were suitable for tetragonal crystals. As such, they predict a 45° rotation of the VL rather than a 90° rotation, and it was hypothesised by White *et al* that higher order terms were needed in the expansion for VL free energy in order to adjust for an orthorhombic crystal. The second structure transition at 6.7 T was attributed to the superconducting order parameter, and the continued evolution of the high field structure phase was associated with changes in the order parameter with field. Phase sensitive measurements (Kirtley, 2005) showed that the nodes in the order parameter existed not

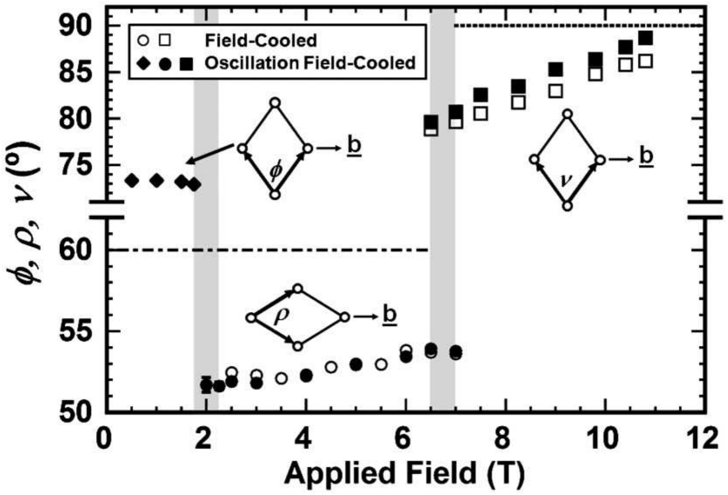

Figure 3.4: Diagram showing the vortex lattice structure as a function of field, in terms of the opening angle of the lattice. Three distinct structure phases are observed, with opening angles of each being labelled as ϕ, ρ and ν respectively. Image reprinted from work by White *et al* (White et al., 2009)

at the 45° expected for a pure *d*-wave order parameter, but were slightly stretched away from this configuration. This is expected, since the crystal symmetry is orthorhombic and so the 45° directions are not symmetry planes. The continuous evolution of the rhombic phase with field was attributed to an *s*-wave addition to the order parameter arising from superconducting states associated with the CuO chains, thought to occur due to the proximity effect emanating from the CuO_2 planes. It was hypothesised that the chain contribution to the order parameter would be suppressed with increasing field, gradually reducing the contribution they made to the order parameter and causing the nodes to shift. With the nearest neighbour directions of the vortices being governed by the minima in the order parameter, this change in the superconducting gap would be clearly reflected in the flux lattice (Atkinson and Carbotte, 1995; Atkinson and Sonier, 2008).

The temperature dependence of the vortex lattice form factor was also investigated in previous work by the group (White et al., 2009), at a variety of fields. Figure 3.5 shows the temperature dependences of the form factor at 2 and 5 T. Here it was found that the temperature dependence at low fields fitted well to a local *d*-wave model, whilst the mid field data (5 T) required the addition of non-local corrections, demonstrating emerging non-locality with field in YBCO. This, combined with a slight temperature dependence of the VL structure in the mid and high field regions and an emergence of a form factor anisotropy with field strongly suggested that whilst local physics governed the behaviour of the vortex lattice at low fields, the higher field region was dominated by non-local effects. The structural transitions, however, were found to be temperature independent despite the expected tendency for the high field structure to evolve away from a square lattice with increasing temperature.

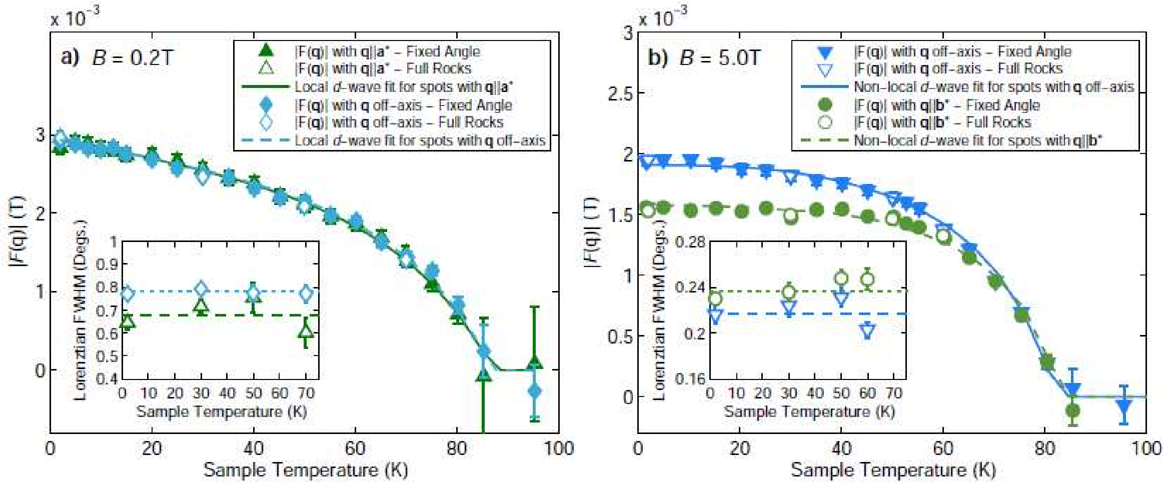

Figure 3.5: Temperature dependence of the vortex lattice form factor across the full superconducting temperature range of YBCO for fields of 2 and 5 T. Image reproduced from (White et al., 2009).

3.2 Samples

Measurements presented here were taken on a polycrystal mosaic of de-twinned $YBa_2Cu_2O_7$. The sample consisted of six crystals, with a total mass of around 20 mg, which were mounted on a 1 mm thick aluminium plate with a co-alignment within 1.5 degrees, as shown by X-Ray Laue photography. The mean thickness of the crystals was estimated to be 0.35 mm, much less than the 1/e length of 2.0 cm, thus meaning that attenuation of the neutron beam should not be a problem in this experiment. The sample is depicted in figure 3.6. Cadmium was mounted around the sample to prevent unwanted scattering and provide easy alignment with the neutron beam. Aluminium foil was used to wrap the sample, to protect it from moisture in the atmosphere and condensation, should it be removed from a cryostat when below room temperature.

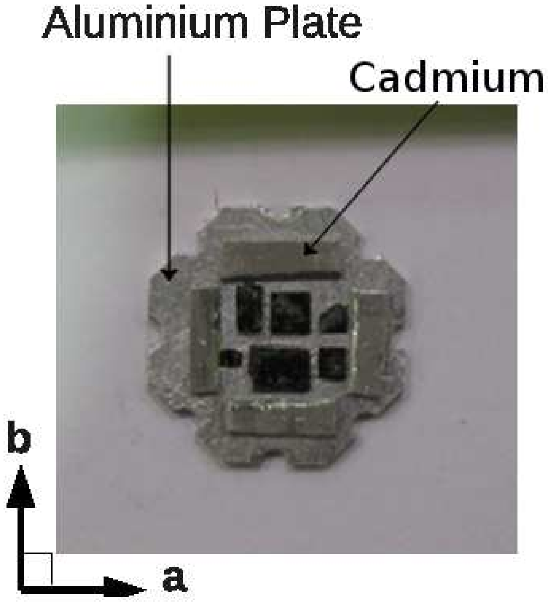

Figure 3.6: Photograph of the sample used for these experiments, of total mass $\sim$ 20 mg, which was mounted in the cryostat with the crystal **a** axis vertical.

Due to the inequality of the **a** and **b** lattice parameters, the crystal structure of YBCO is orthorhombic, with the **a**/**b** inequality in the region of 2% (Jorgensen et al., 1990). This inequality results in the formation of twin planes in YBaCuO crystals during the growth process, where a single domain at high temperatures naturally decomposes into twin domains during cooling, illustrated in figure 3.2. Here, different domains in the crystal have orthogonal **a** and **b** directions, which nucleate randomly and result in a lack of reproducibility between samples. It has been seen in previous flux lattice studies (White et al., 2008) on twinned samples that the orientation of the VL is different between twin domains depending on the domain's orientation. Flux lines are also susceptible to pinning at twin plane boundaries, which has been observed in real space scanning tunnelling spectroscopy measurements (Maggio-Aprile et al., 1997; Shibata et al., 2003b). These show not only that flux lines are strongly pinned to the twin planes, but also that the local orientation of the flux lattice is perturbed as to be aligned in a square configuration with the vortices along the planes. Far from the planes, the vortices are able to resume the orientation expected from the local physics, which is in contrast to neutron scattering measurements which suggest that the twin planes have a far reaching effect on vortex lattice orientation (Keimer et al., 1994; Brown et al., 2004). From these neutron scattering measurements, a total of four vortex lattice domains have been observed as a result of twinning. Since it is not always possible to distinguish between the intrinsic effects of the crystal lattice and those governed by the twin plane structure, investigations on de-twinned samples are important. For the samples used in these measurements, removal of the crystallographic twinning was undertaken to return the structure to a single domain. This was achieved by application of uniaxial stress of order $2 \times 10^7 \mathrm{Nm}^{-2}$ along the $\langle 100 \rangle$ direction at around 500° C. It was estimated that the sample was de-twinned to a minority domain fraction of 1%, meaning that the VL structure studied should be governed by the intrinsic effects of the crystal lattice.

After the initial experiments it was suspected that the sample had a slightly lower oxygen content than desired. This oxygen deficiency was thought to be non-uniform, and result in a broadening of the superconducting transition temperature. In order to test this, we re-oxygenated the sample in an oxygen atmosphere at 100 bar of O_2 at 577 K for 150 h, before repeating the relevant measurements.

3.3 Investigation with B parallel to the c axis

The experiment discussed here was performed on D22 at the ILL. Fields of up to 16 T were applied parallel to the **c** axis of YBCO, across the full superconducting temperature range of the material.

In order to form an ordered flux lattice from which to take measurements, we predominantly used the oscillation field cool method. Previous SANS measurements on the vortex lattice of YBCO has shown that the procedure, where the sample is cooled in a field undergoing small oscillations about the desired value, to be the method which produces a vortex lattice that is closest to its equilibrium structure (White et al., 2009). In this case, an oscillation of around 0.1% of B was employed.

3.3.1 Structure of the Vortex lattice

In previous work, the structure of the vortex lattice was investigated up to 11 T (White et al., 2009). It was found that a first order reorientation transition of a hexagonal structure took place at 2 T, with another transition from this hexagonal phase to a rhombic phase took place at around 7.7 T. The re-orientation transition was attributed to non-local corrections to anisotropic London theory, whilst the hexagonal/rhombic transition appeared to be driven by the order parameter. Here, we investigate the behaviour of the vortex lattice structure in applied fields of up to 16 T, by rocking over all diffraction spots in the lattice at the required fields. Figure 3.7 shows the variation in opening angle as a function of field at both 2 K and 60 K, and also as a function of temperature at both 10 T and 16 T. Here, spot positions are calculated using data from the peak of the rocking curves for each spot, as defined by the full width at half height and above, with their position on the detector calculated by a fit to a 2D Gaussian. All field-dependent structure measurements were taken at base temperature with the lattice prepared using the oscillation field cool method. For the temperature-dependent data, the lattice was prepared using the oscillation field cool procedure, with data taken on warming. The vortex lattice structure is seen to remain reasonably stable from base temperature to around 35 K, whereupon the side opening angle monotonically decreases until we loose signal from the lattice at high temperature.

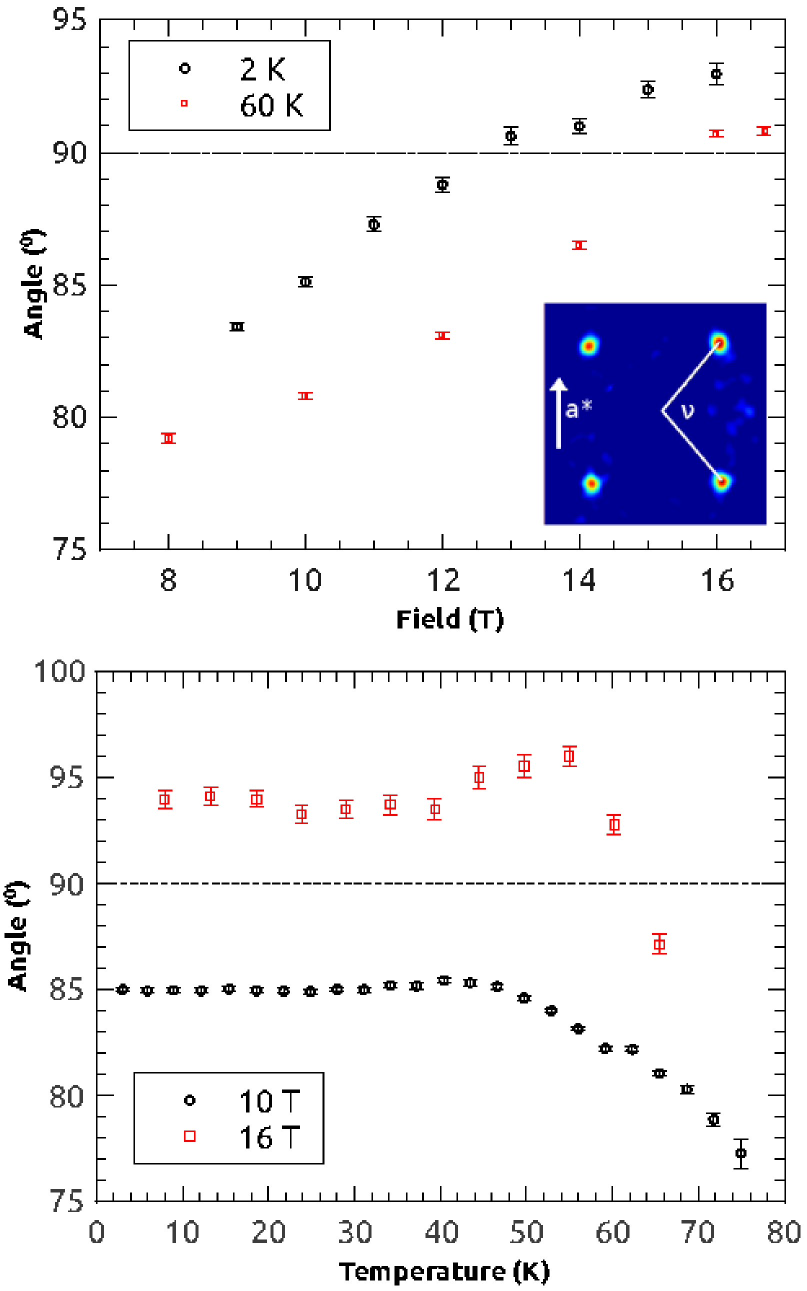

Figure 3.7: Top: Graph showing the variation of side opening angle with applied field at both 2 K and 60 K of the reciprocal space lattice, with data taken after OFC to the temperature at which the data was taken. The relevant opening angle, ν, is shown in the diffraction pattern. Bottom: Variation of the same opening angle as a function of temperature, for applied fields of 10 T and 16 T. The VL was prepared by OFC to base temperature, with data taken on warming.

It can be seen that the vortex lattice continues the field dependent trend seen in previous measurements (White et al., 2009), with the structure passing *through* square at around 12 T, with no transition to a field independent structure. This being said, the rate of evolution of the vortex lattice with field is decreasing towards the maximum of our field range, so in the absence of any further structure transitions it would seem that the lattice is heading towards a field independent structure, although we are unable to confirm this in these measurements. For a pure d-wave superconductor, with the field applied in the basal plane, it would be expected at high field for the vortex lattice to assume a square symmetry, since the order parameter determines the symmetry of the vortex cores which are most influential in vortex lattice coordination at high fields (Affleck and Franz, 1997; Ichioka et al., 1997, 1999; Shiraishi et al., 1999). However, since YBCO_7 possesses an orthorhombic crystal symmetry, the order parameter cannot be intrinsically pure d-wave but must contain a finite s-wave admixture, giving the basal plane order parameter a rhombic symmetry.

Whilst it may be possible that the observed anisotropy in superconducting properties is inherent to the CuO_2 planes, low field measurements on the vortex lattice gave a penetration depth anisotropy of around ~ 1.28 (White et al., 2009), which implies an anisotropy in n_s/m^* of > 1.6. This value appears to be too high to be accounted for by plane superconductivity alone, and the sign of this anisotropy at low field implies an extra contribution to superconductivity along the chain directions. To find an explanation for the evolution of rhombic phase with field, we therefore consider the effect of the copper oxide chains on a system whose superconducting properties are predominantly governed by the physics of the CuO_2 planes. In theory, we find two different hypothesis arise to explain superconducting states on the CuO chains (Xiang and Wheatley, 1996; Zhang et al., 1994). Models are based either on the idea of single particle tunnelling between the planes and chains or a Josephson-like cooper pair tunnelling model. Looking at the temperature dependence of the superfluid density from the low field work (White et al., 2009) we see that both the **a** and **b** directions exhibit nodal behaviour, indicating that the pair tunnelling model, which predicts nodes in any chain order parameter, is a more appropriate description for nodal behaviour, rather than the single particle proximity effect (Atkinson and Carbotte, 1995). In our high field data, we see that the anisotropy is decreasing and changing sign, which may indicate a modification in chain superconductivity since we would expect that, at a low fraction of H$_{c2}$, the quasi 1-D chain states would be less robust than their 2-D plane counterparts.

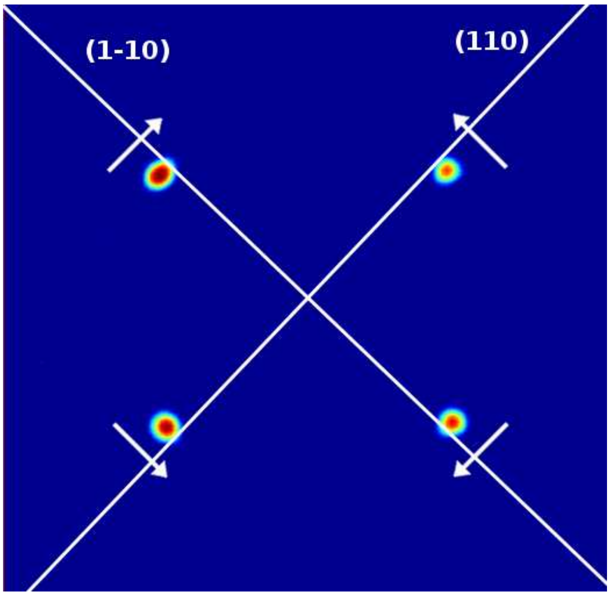

Figure 3.8: Figure showing the VL diffraction pattern at 9 T, with the (110) axes indicated. Arrows indicate the structural evolution of the VL diffraction spots as the field is increased.

Adding non-local corrections to London theory has proven to be a reasonably successful method in describing the VL structure of unconventional superconductors along a fourfold axis (Kogan and Miranović, 1997; Kogan et al., 1996) and conventional high-κ materials such as V_3Si (Yethiraj et al., 1999). Non-local effects can provide additional anisotropy alongside the effective mass anisotropy included in local London models or Ginzburg-Landau theories. Presently, theories tackle the input of non-local effects from two separate sources: either an anisotropic gap in the presence of an isotropic Fermi surface (Kogan and Miranović, 1997; Franz et al., 1997; Suzuki et al., 2010) or an isotropic gap combined with an anisotropic Fermi surface (Kogan and Miranović, 1997; Kogan et al., 1996). For d-wave materials such as YBCO, non-local effects are brought into play due to the effective coherence length, $\xi \propto 1/\Delta(k)$, being divergent near the nodes in the order parameter. Despite the success of these models explaining some of the observed structural evolution, it was pointed out by White *et al* (White et al., 2011) that none of the non-local theories agree with the structural evolution observed in YBCO_7.

Figure 3.7 also shows the temperature dependence of the vortex lattice structure. Both the 10 T and 16 T data are seen to have a systematic temperature dependence, although the precise behaviour differs between the fields. The VL structure at 10 T shows no temperature dependence below 40 K, possibly due to the lattice being 'frozen in' due to pinning effects. Here, the flux line pinning in the sample is strong enough such that $k_B T$ is unable to remove the flux line from the relevant pinning site and thus the vortex lattice structure is unable to evolve. However, it may also be possible that the mechanism responsible for the structural evolution at higher temperatures does not influence the system until ≈40 K, and that pinning plays a minimal role in the steady structure at lower temperatures. We discuss the effects of pinning on the VL in YBCO in the following section. The temperature dependence above 40 K can be understood in the context of the *d*-wave order parameter, where the flux line nearest neighbours are expected to align themselves along the node directions (Ichioka et al., 1999). With increasing temperature, one might expect the nodes to be come less influential in the vortex lattice structure as increasing $k_B T$ smears the quasiparticle excitation spectra out away from the nodes, which may allow the VL to assume a coordination closer to that of a hexagonal lattice. Furthermore, it was seen in the work by White *et al* (White et al., 2009, 2011) that non-local effects play a strong role in determining the structure of the VL. Non-local effects are expected to become less important with increasing temperature (Kogan and Miranović, 1997; Kogan et al., 1996; Franz et al., 1997), and as such the increase in temperature may result in the structural variation seen here where the lattice evolves towards the lower field structure seen by White *et al* (White et al., 2009) which is governed by local effects.

At 16 T the structure of the vortex lattice presents an unusual temperature dependence. It, too, has a reasonably constant structure at temperatures below 40 K, which may again be influenced by both flux line pinning and an inability for $k_B T$ to access new physics. Above 40 K, however, it presents us with a non-monotonic behaviour in its structure. The lattice first becomes more anisotropic before reversing the direction of its evolution, and passing through both its low temperature structure and a square lattice. In order to exhibit such a non-monotonic behaviour it seems necessary that multiple sources of anisotropy are contributing to its evolution. With YBCO possessing both an anisotropic Fermi velocity and a d-wave like gap, it is possible that both of these are influencing the structure of the vortex lattice. With models used to predict vortex lattice structure assuming only a single anisotropic component, be it the anisotropic gap models or anisotropic Fermi velocity models (Suzuki et al., 2010), we at present lack the theoretical framework to explore the possibility of these competing. Furthermore, these models are assuming a tetragonal crystal symmetry, rather than orthorhombic, and have not been expanded to discuss the effects of temperature.

3.3.2 Irreversibility in the Lattice

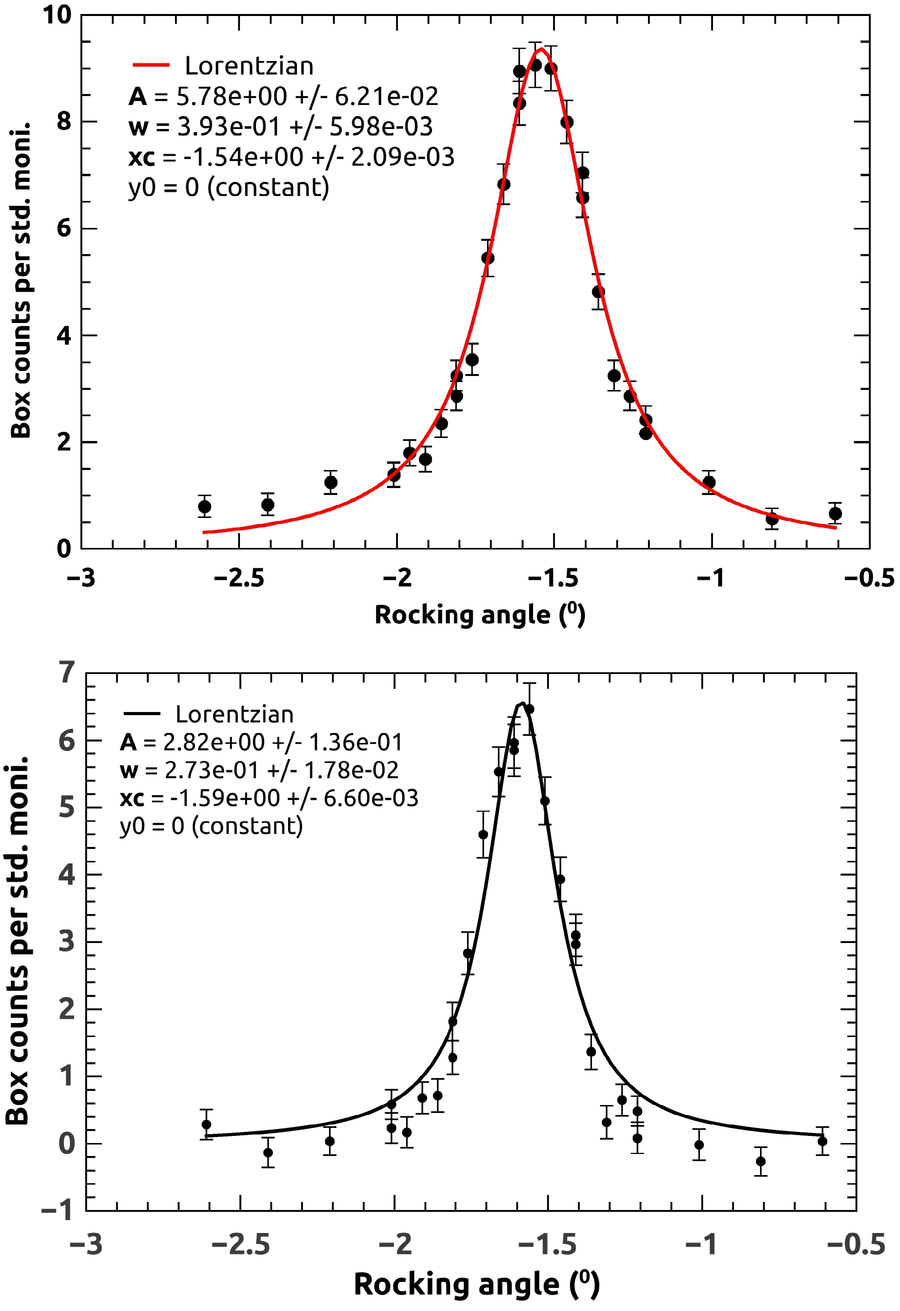

Figure 3.9: Top: figure showing a rocking curve at 8 K in a field of 10 T. Bottom: figure showing a rocking curve at 65 K in a field of 10 T. The fitting functions for both rocking curves is a Lorentzian, with respective parameters shown in the figure, with A the amplitude of the function, w the width, x_c the centre in x and $y0$ a constant, which is held at zero.

We discuss first the behaviour of the rocking curve width as a function of temperature, since it provides several important points for interpreting the corresponding form factors. As shown in figure 3.9, the rocking curve was fitted to a Lorentzian line-shape, of the form

$$I(x) = y_0 + \frac{A}{\pi}\frac{\omega}{4(x - x_c)^2 + \omega^2}. \tag{3.1}$$

Here, the y_0 is a constant background which is set equal to zero, A is the amplitude, or peak height, of the function, x is the rocking angle, x_c is the centre of the distribution and ω is the full width at half maximum of the function (FWHM). The rocking curve width is a function of both instrumental resolution and perfection of the vortex lattice (Cubitt et al., 1992), which was discussed in section 1.14. We have estimated the contribution of the vortex lattice to the rocking curve width by comparing it to the resolution limit of the instrument, shown in the dotted lines in figure 3.10. Here, we have assumed that the $\Delta D/D$ of the vortex lattice spacing and the flux line mosaic spread, b, are both zero and used only the collimation width and neutron wavelength spread in calculating the predicted rocking curve width. We can see in fig. 3.10 that the rocking curve width of the vortex lattice dominates at all but the highest temperatures. We identify for each temperature scan an 'irreversibility temperature', below which the vortex lattice is frozen in and the rocking curve width does not change. Above 50 K, the rocking curve width narrows as the system approaches T_c, indicating an improvement of lattice quality as the temperature increases. For the rocking curve width as a function of temperature at 10 T, this change was gradual, but for the 16 T a large peak was seen in the rocking curve width, which occurs in the same temperature region where the VL structure begins to change. Recalling the lattice being prepared by OFC, with data taken on warming, this increasing disorder is surprising as we would perhaps expect the VL to be most disordered at low temperatures where the structure is frozen-in. This increase is not reflected in a broadening of the spots across the detector as they move, which would increase the rocking curve width, and so appears to be a real effect. Beyond this peak, the rocking curve width decreases as we approach T_c, owing to the increased ability for the thermal energy of the flux lines to overcome the potential of pinning sites. However, despite this improvement the rocking curve width never reaches the resolution limit, indicating that the VL pinning is still effective above the irreversibility temperature. This is not only seen in macroscopic measurements of magnetic reversibility, but also in the temperature dependence of the structure of the vortex lattice shown in figure 3.11.

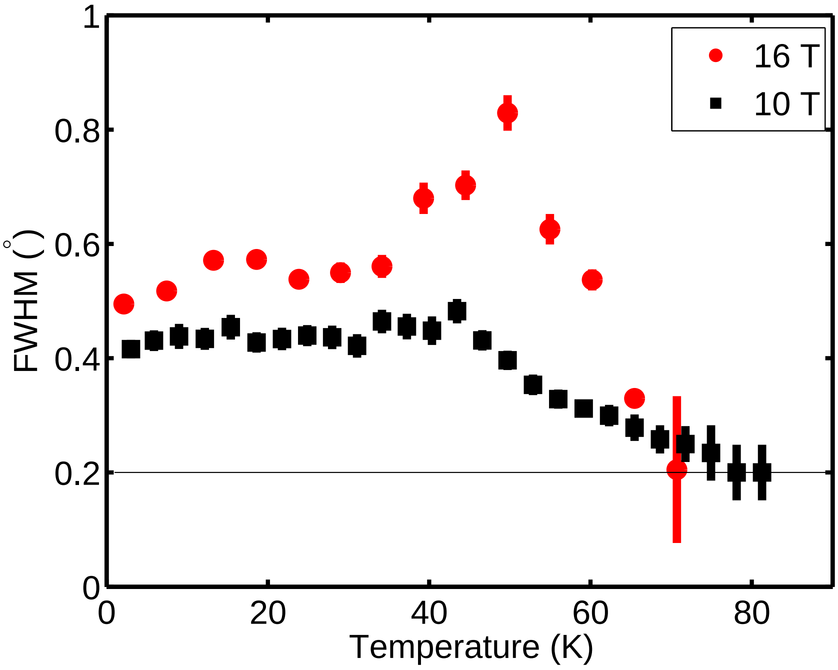

Figure 3.10: Figure showing the rocking curve width as a function of temperature for the same data as the structure scan in figure 3.7 and the form factors in figure 3.15. Data were taken by oscillation field cooling the lattice to 2 K and then measuring on warming. Dotted lines correspond to the resolution width of the instrument.

In figure 3.10, high temperature data, around 50 K and above, shows rocking curves which approach the resolution limit. Passing below this temperature, rocking curves become broader, this suggests pinning effects becoming important at lower temperatures, disordering the lattice along the axis of flux lines and providing a broader range of Bragg conditions. The rocking curves taken here were larger than those found by White *et al*, illustrated by the signal present at large rocking angles seen in figure 3.9. We suspected that the new crystals we were using suffered from a degree of pinning not found in the mosaic used in previous experiments. This formed part of our decision to re-oxygenate the crystals, which will be discussed in more detail in the section on vortex lattice melting.

The pinning effects which result in the broadening of the rocking curves is also expressed in hysteresis of the vortex lattice shape. Fig. 3.7 shows the structural variation, as a function of temperature for a scan taken on *warming*. Fig. 3.11 shows the same opening angle from a temperature scan where data was taken successively in both warming and cooling scans. Small field oscillations of the same type as with the oscillation field cooling method were applied between each temperature, both on warming and on cooling. Whilst this scan was done in less detail, and only to 30 K, the data clearly shows hysteresis in the VL coordination and FWHM of rocking curve, with the temperature at which the lattice begins to evolve being different for warming and cooling. The irreversibility temperature is clearly seen, where the structure of the vortex lattice ceases to be reversible under changes in temperature, and below which the lattice seems unable to evolve both in coordination and perfection. For comparison, the integrated intensities are shown in figure 3.11, indicating that despite changes in the structure the integrated intensity scattered from the lattice is the same. It was hypothesised in the work by White *et al* that neutron diffraction from the vortex lattice of YBCO was subject to a static Debye-Waller (DW) effect, where strong vortex pinning can reduce the scattering volume of the VL by causing defects in the lattice. If such a Debye-Waller effect is affecting the lattice, it seems systematic in its appearance with temperature and is unaffected by the hysteresis in lattice structure.

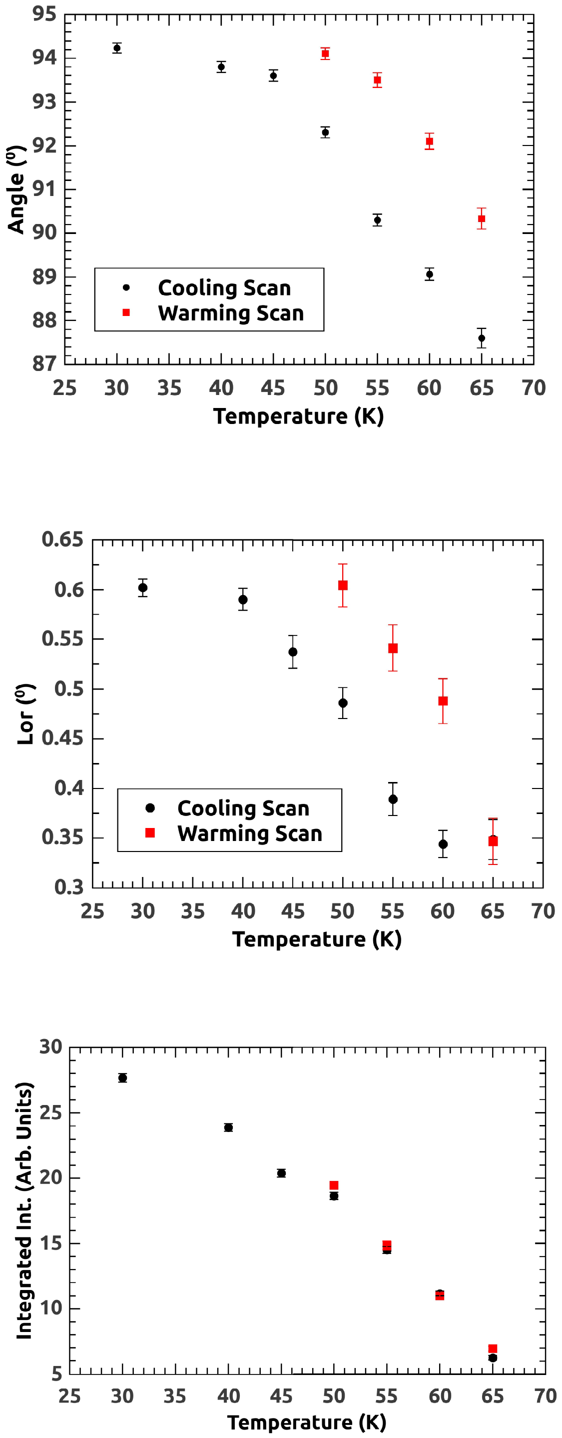

Figure 3.11: Top: figure showing the vortex lattice opening angle as a function of temperature at 16 T. Middle: the corresponding weighted FWHM of the rocking curves fitted to a Lorentzian function. Bottom: The integrated intensities for the same data. Data was taken by OFC at 16 T between each temperature, for both cooling and warming.

The signal from the vortex lattice in the tails of the rocking curve also showed unusual behaviour in terms of its structure. When investigating the vortex lattice structure, such as in figure 3.7, it is appropriate to take data only from the peak of the rocking curve in order to determine the location of the Bragg reflection, since the spot will appear to move across the detector as the spot is rocked through. The peak of the rocking curve represents the ideal case Bragg condition, and will therefore provide the most accurate data with which to investigate the vortex lattice structure. However, the data from the tails of the rocking curve should average out to the same structure if the Bragg spot has been fully rocked through, since the distortion on one side of the rock should be cancelled out by the corresponding data on the other side, leaving an average position equivalent to that of the peak data. Figure 3.12 shows the opening angle determined from both the tail and the peak data as a function of temperature in an applied field of 10 T, with data taken on warming after oscillation field cooling to base temperature. We can see that below around 50 K, the data from the tails gives a different vortex lattice shape than the peak data. Furthermore, the VL opening angle present in the tail data is *larger* than the peak data, appearing to possess a lower irreversibility temperature. This is contrary to what we might expect from flux lines subjected to pinning, where it would be logical to assume that more disordered sections of the lattice would get frozen out before the more ordered regions, leaving the more ordered flux lines to continue their structural evolution as the temperature is further reduced. These data could suggest that the more disordered parts of the lattice are perhaps being influenced by slightly different local physics, where oxygen vacancies that bring about pinning sites also result in a variation in local physics as the charge transfer to the CuO_2 planes is reduced. If the oxygen content is varied across the crystal with regions of deficiency much larger than the inter vortex spacing, one might expect variations in local physics large enough to influence the coordination of the vortex lattice. However, since this phenomenon has a characteristic temperature much lower than the critical temperature of YBCO, it seems very unlikely that a variation in local physics is causing the unusual temperature dependence of the vortex lattice coordination in the tails. It seems far more likely that this unusual behaviour is a result of vortex lattice pinning given that its characteristic temperature is the same as the irreversibility temperature. We note that, in twinned YBCO, pinning to the twin planes is able to govern the orientation and coordination of the vortex lattice when compared to the behaviour of the lattice in de-twinned sample (Brown et al., 2004; White et al., 2011). Although we expect these crystals to be de-twinned to around 1 % or less (White et al., 2009), it is possible that these crystals still posses enough twin planes to influence the orientation of small regions of the vortex lattice. We note from the work by Brown *et al* that the presence of twinning results in two vortex lattice domains which are orthogonal to each other. Our results in figure 3.12 show that data in the tails possess an opening angle which is almost, but not quite, symmetric about 90° with that of the peak data. The unusual behaviour of the tail data could be a result of a re-orientation of small parts of the vortex lattice due to a minority of remaining, small, twinned regions which may also explain the presence of disorder which leads to wide rocking curves.

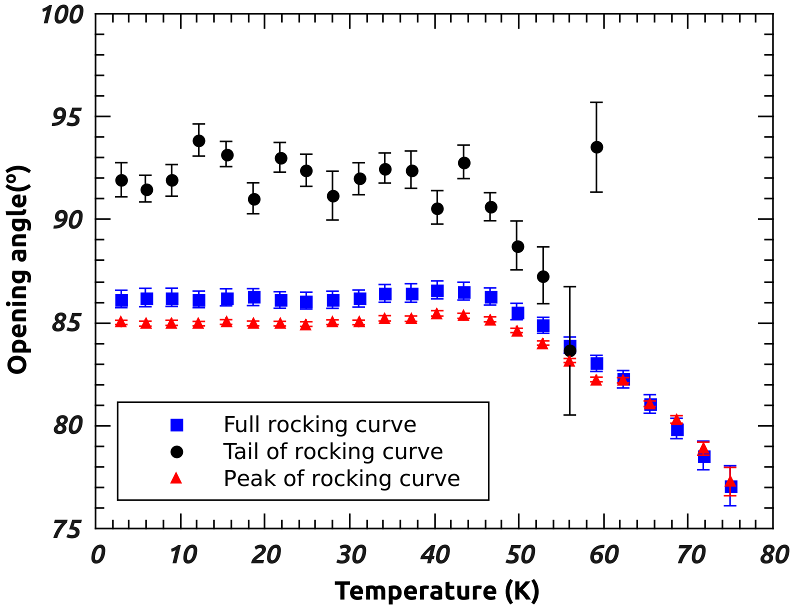

Figure 3.12: Figure showing the opening angle of the vortex lattice as a function of temperature in an applied field of 10 T. The opening angle is given for data from the full rocking curve, data from the peak of the rocking curve and data from the tails of the rocking curve, showing different behaviour from the tail and peak data.

3.3.3 Investigation into the vortex lattice Form Factor

The local field within a flux lattice can be represented as the sum over all the spatial Fourier components, F($\mathbf{q}$), at the various scattering vectors $\mathbf{q}$ of the reciprocal lattice. The magnitude of F($\mathbf{q}$) is referred to as the 'form factor', and is related to the integrated intensity $\mathrm{I}_{\mathbf{q}}$ of a Bragg reflection from the vortex lattice through the relationship described earlier in equation 1.71. Investigating the field and temperature dependence of the VL form factor can elucidate important information about the superconducting state.

We have investigated the field dependence of the vortex lattice form factor between 9 T and 16 T at base temperature, and the results are shown in figure 3.13. To model its field dependence, we have employed the local London model which has been extended to account for both **ab** plane anisotropy and the finite size of the vortex cores (White et al., 2011) .

$$F(\mathbf{q}) = \frac{\langle B \rangle \exp(-c(q_x^2\xi_b^2 + q_y^2\xi_a^2))}{q_x^2\lambda_a^2 + q_y^2\lambda_b^2}, \tag{3.2}$$

$\langle B \rangle$ is the average internal induction, ξ_i is the coherence length along i, λ_i is the penetration depth resulting from supercurrents flowing in the direction i and $\mathbf{q}_i$ are components of the scattering vector. Here, i is an in-plane Cartesian component with $\mathbf{q}_x$ parallel to $\mathbf{b}^*$. The cut-off parameter c accounts for the finite size of the vortex cores, and both theoretical predictions and previous experiments have shown that a suitable value for c in our field and temperature range is 0.44 (White et al., 2011; Ichioka et al., 1997). Following the values for ξ, λ and c found from previous neutron scattering experiments, we find that the form factor above 10 T is larger than expected from the London model when extrapolating from the low field data. The model is unable to fit the whole range of data using field independent parameters, whilst the strong indications that a static Debye-Waller factor is affecting our data suggests that finding a field dependence for ξ or λ is not possible. Figure 3.13 shows two plots of the predicted form factor from the extended London model using field independent values for ξ and λ. Unlike the low field measurements (White et al., 2009) where these field independent parameters provided a good fit in fields up to 11 T, we can see that they do not provide such a fit in our higher field range. Fig. 3.13 shows two predictions from the extended London model, one of which is appropriate for either the low field region around 10 T, which also fitted the low field data taken by White *et al* (White et al., 2009), and another that fits the higher field data at 15 - 16 T. The values for ξ and λ used to create these predictions are shown in table 3.1. It is evident that either ξ and/or λ are no longer field independent as they were seen to be at fields lower than 11 T or we require another explanation for the inability of the extended London model to fit our data. We note that since our data does not include any Bragg reflections parallel to $\mathbf{a}^*$ or $\mathbf{b}^*$, we are unable to fit along **a** or **b** individually. As such, we fixed the **a**/**b** ratio in our attempts to fit the data, since we have no specific reason to suspect this ratio to change.

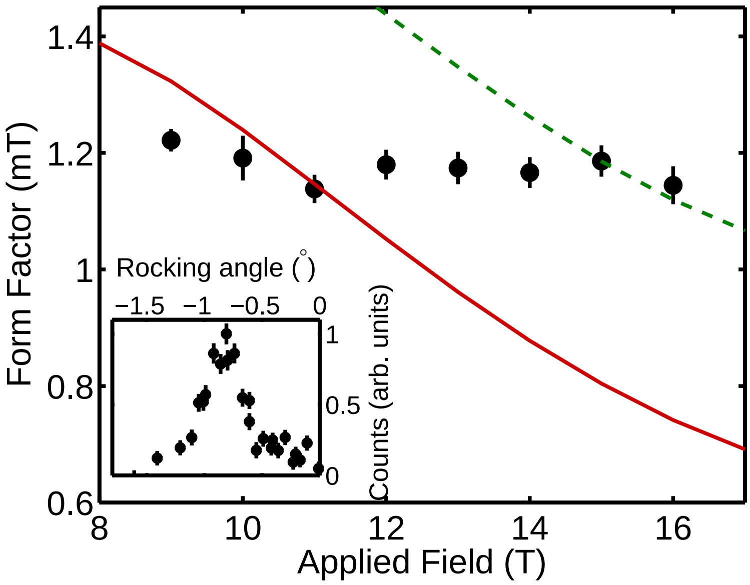

Figure 3.13: Figure showing the variation with field of the vortex lattice form factor at a base temperature of 2 K. Experimental data are shown as discrete points, whilst the solid and dashed lines give the prediction from the extended London model (ELM). The red line gives the London model with parameter values from earlier experiments done below 11 T (White et al., 2011), whilst the green dashed line uses the same penetration depth, but a shorter coherence length. Inset, a rocking curve at 10 T is shown.

Field Range	λ_a (nm)	λ_b (nm)	ξ_a (nm)	ξ_b (nm)
Low Field	138	107	3.04	3.54
High Field	138	107	2.70	3.14

Table 3.1: Table showing the values for ξ and λ used in extended London model fits in fig. 3.13. The 'low field' values are taken from the work at lower fields by White *et al*, whilst the 'high field' values have the same penetration depth but a shorter coherence length, with the **a**/**b** ratio kept the same as for the low field data.

The red line in fig. 3.13 shows the fit to the extended London model using the values obtained from neutron scattering experiments at low field (White et al., 2011). We note that the values for ξ_a and ξ_b found in previous experiments seemed too large, since from equation 1.56 they give an upper critical field of around 30 T, which is too low for YBCO_7. This could result from frozen-in disorder along the vortices, giving a static Debye-Waller factor which reduces the scattering from the vortex lattice. A mean square deviation $\langle u^2 \rangle$ from a straight vortex would contribute an additional term of the form $\exp(-q^2\langle u^2\rangle/4)$ to the numerator of the London model in equation 3.2. This is indistinguishable from the Gaussian cut-off term, and has the effect of making the core correction seem larger, leading the fit to return an incorrect estimation of the coherence length. It is possible that the effects of disorder are reduced in the high field range we are investigating here, and the actual values of ξ are smaller than those obtained previously. The 'high field' fit to the data in fig. 3.13 uses a shorter coherence length than was found previously, whilst maintaining the **a** / **b** ratio and using the same values for penetration depth. We can see that the high field data at the top of our field range can be fit to the London model with a smaller coherence length than found before. This strongly suggests that there is a static Debye Waller effect present in the low field data which is being reduced at high field. We note that this estimate for the coherence length returns an upper critical field prediction of around 40 T, which is still too low for YBCO, but closer to reality. This suggests that whilst the DW is reduced at higher fields it still seems to be affecting the lattice.

Another model which has proven able to model the field dependence of the VL form factor is the Clem model (Clem, 1975). Obtained from a variational solution to the GL equations, it takes the form

$$F(\mathbf{q}) = \langle B\rangle \frac{gK_1(g)}{q_x^2\lambda_a^2 + q_y^2\lambda_b^2}, \quad g = \sqrt{2}(q_x^2\xi_b^2 + q_y^2\xi_a^2)^{1/2} \tag{3.3}$$

where K_1 is a modified Bessel function of the second kind. Since this model is based on the GL equations, we might expect it only to be valid near T_c, however it proved to be applicable in the earlier work on YBCO at lower fields (White et al., 2011).

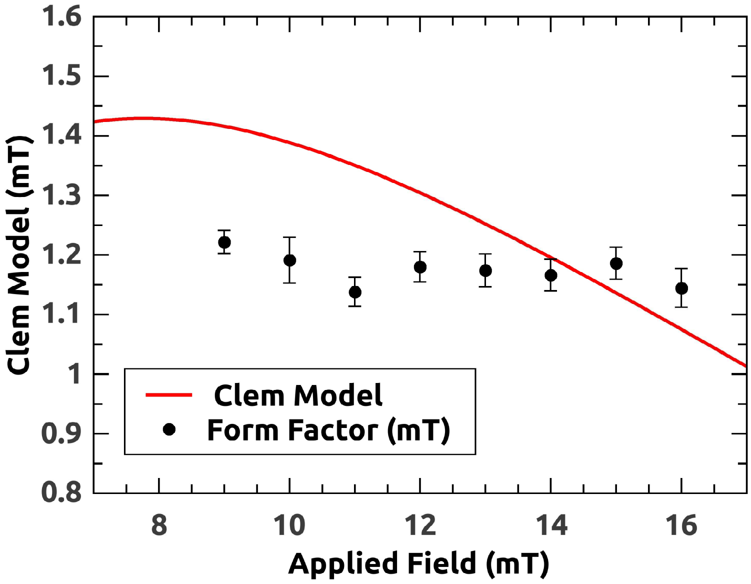

Figure 3.14: Figure showing the variation with field of the vortex lattice form factor at a base temperature of 2 K alongside a prediction for the variation of the vortex lattice form factor as given by the Clem model. The model, described in the text, is given parameters $\xi_a = 2.50$ nm, $\xi_b = 2.88$ nm, $\lambda_a = 138$ nm and $\lambda_b = 107$ nm.

We can see in fig. 3.14 that whilst the Clem model performs better than the London model, it still does not provide a good fit to the data. The Clem model is unable to account for the slow variation in the form factor in the same manner as with the extended London model - they both predict a faster fall off in the form factor with increasing field than is observed in the data. However, we note that in order to fit the high field data, maintaining the **ab** ratio of the lower field data and value of λ, the model gives slightly shorter values for the coherence length. This supports the same suggestion as the anisotropic extended London model, where it appears that a static Debye-Waller factor is affecting the lower field data and being reduced upon reaching the higher field regime. With no obvious sharp transition point, it seems likely that the reduction in the DW factor with field is a gradual process.

3.3.4 Investigation into the vortex lattice Form Factor at higher temperatures

Temperature dependence of the vortex lattice form factor was measured at 10 T and 16 T. These data, shown in figure 3.15, show unusual, non *d*-wave like behaviour. Whilst the form factor at 10 T appears to remain reasonably flat till around 50 K, the 16 T temperature dependence of the vortex lattice form factor shows a sudden drop in form factor at 70 K. This drop is an indication of vortex lattice melting, and marks a departure from Bragg diffraction, resulting in a clear loss of signal, which will be discussed in more detail in section 3.3.5.

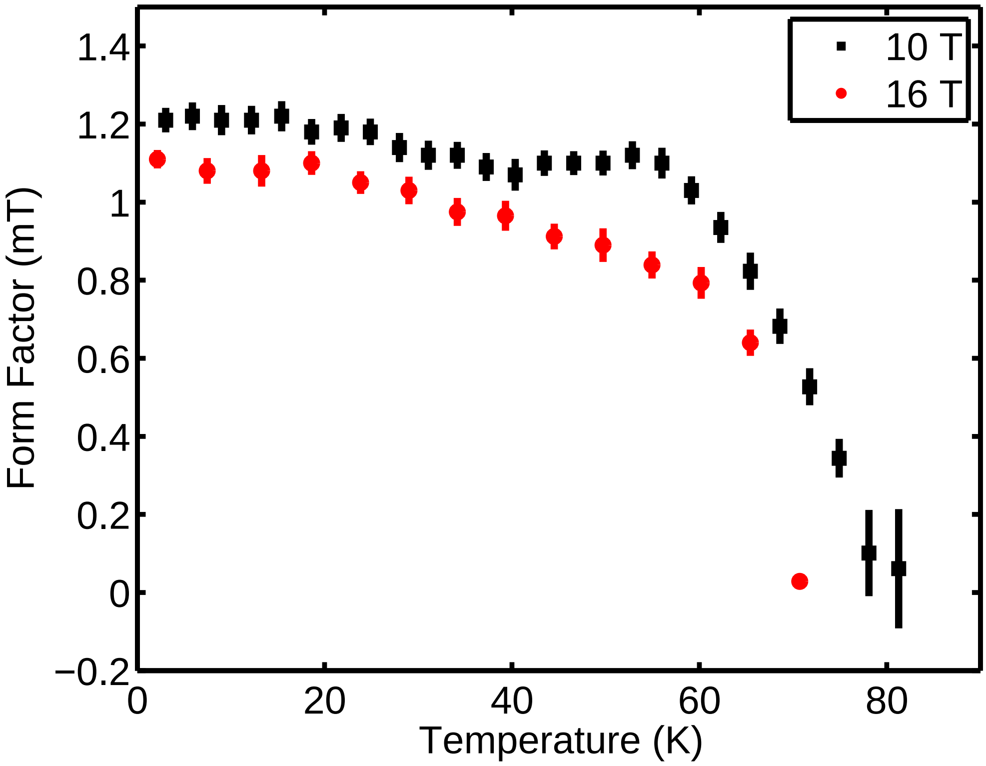

Figure 3.15: The temperature dependence of the vortex lattice form factor for 10 T and 16 T. Intensity was integrated over rocking curves for all temperatures.

At 10 T, the form factor shows unusual, non-monotonic variation as the temperature is increased between 40 K and 55 K, which begins as the rocking curve width starts to change. Here, the form factor appears to remain flat within experimental error till around 50 K, which is contrary to expected behaviour since the form factor is proportional to the superfluid density, which should decrease with increasing temperature. This flattening between 40 K and 55 K may be a result of the flux lattice annealing with increasing temperature. The data was taken after oscillation field cooling to base temperature, with each subsequent data point taken after warming to the relevant temperature, with each data point taking 20 minutes for the 10 T data and 40 minutes for the 16 T data. Here, the static Debye-Waller factor, which we suspect from our field dependence of the VL form factor is present at this field, may be reduced as the temperature is high enough to anneal out the defects in the lattice, effectively increasing the scattering volume of the vortex lattice.

At low temperatures, the 10 T data shows a weak temperature dependence. Aside from the possibility of a static Debye-Waller effect which varies with temperature, it is probable that this flattening of the VL form factor at low temperature is due to strong field induced non-local response, which was seen at 5 T in this material (White et al., 2011). The effect of non-local effects on the magnetic penetration depth was studied by Amin *et al* in $\mathrm{YBCO}_{6.95}$. It was found that with increasing field the expected linear temperature dependence at low temperatures of the superfluid density crossed over to a T^3 dependence below a temperature $T^* = \Delta_0(\xi_0/d)\alpha\sqrt{H}$, where ξ_0 is the non-local length scale, or Pippard coherence length given in equation 1.27. Following the method described previously in the section on pnictide superconductors 2.2.5, this would cause the temperature dependence of the superfluid density in equation 2.8 to take the form (Amin et al., 2000, 1998)

$$\frac{1}{\lambda^{nl}_{\mathbf{a/b}}} = 1 - (1 - \rho_{s,\mathbf{a/b}}(T))\left(\frac{T_c + T^*}{T_C}\right)\left(\frac{T^2}{T^2 + (T^*)^2}\right) \tag{3.4}$$

where $\lambda^{nl}_{\mathbf{a/b}}$ is the penetration depth with non local corrections and $\rho_{s,\mathbf{a/b}}(T)$ is the superfluid density calculated in equation 2.8. This method of accounting for non-local effects proved successful in describing the temperature dependence of the form factor at lower fields (White et al., 2011). However, following the same method as described in the section on the pnictide superconductors, section 2.2.5, whilst using the non local correction given in equation 3.4, we find our present data more challenging to fit.

To fit these data, we have fixed the **ab** ratios of ξ and λ to those found in the lower field measurements (White et al., 2011) in the same manner as when modelling the form factor variation with field in section 3.3.3. The temperature dependences of the VL form factor at both 10T and 16 T did not posses precise minimum in their residuals of fit, which combined with a large number of parameters made it difficult for the fit routine to find a definite answer. In order to overcome this, we followed a similar method to that used in fitting the temperature dependence of normalised diffracted intensity in BFAP 2.4.5. This method entailed providing the program with a sequence of possible values for ξ and λ whilst giving it another parameter to vary - in this case we chose the superconducting gap magnitude Δ. We expect the superconducting gap in YBCO to have a magnitude of around 295 K (White et al., 2011), and we note that the minimum in the fit residuals shown in fig. 3.16 and fig. 3.18 come close to this expected value in the corresponding plot of gap magnitude, although as discussed later we find that these fits are subject to pinning effects which cause the fit minimum to not quite lie on this gap magnitude. For the fitting, T_c was taken from data by Junod *et al* (Junod et al., 1997), which is shown in fig 3.22.

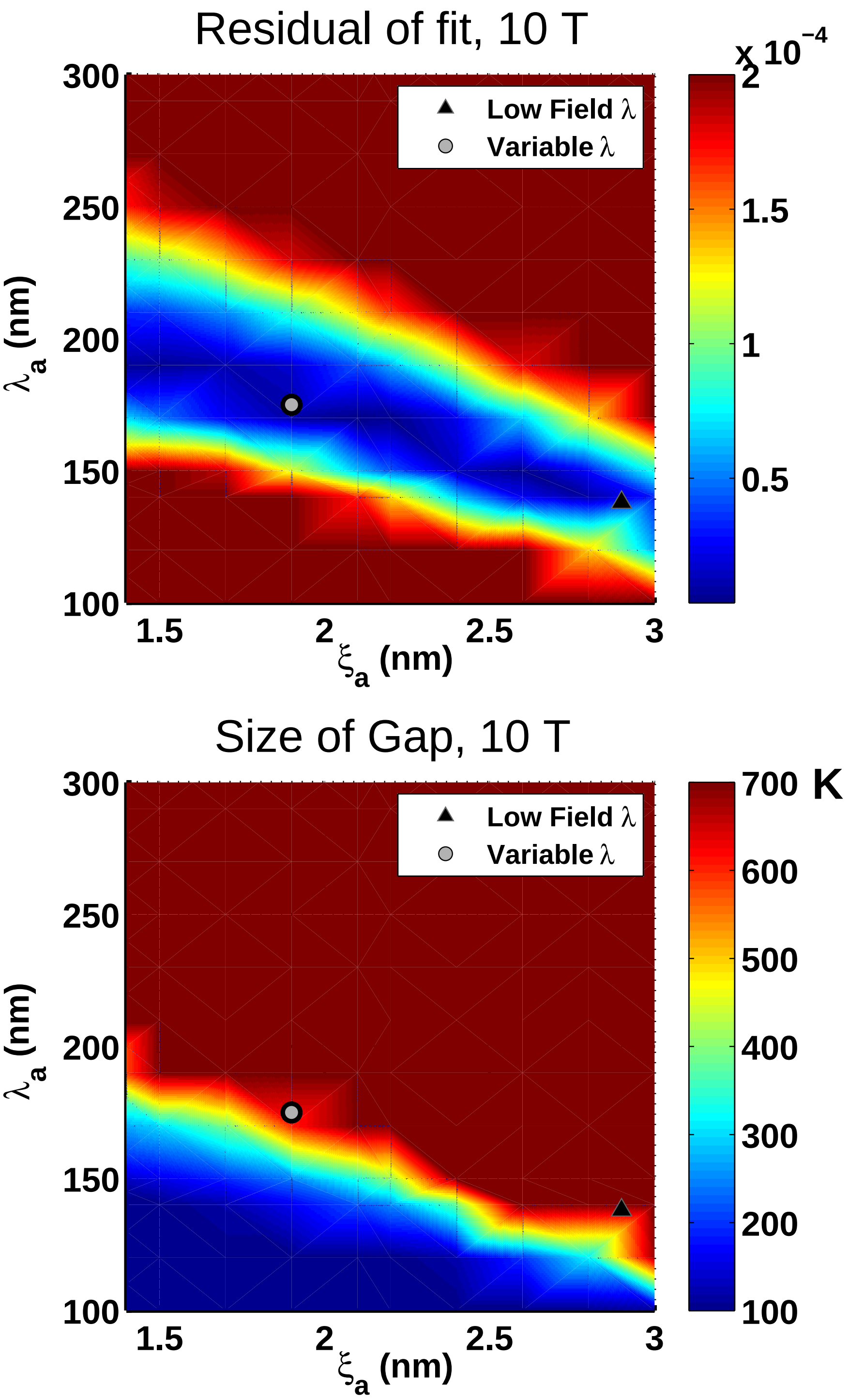

Figure 3.16: Top: figure showing the residuals of fit for the fit to the temperature dependence of the vortex lattice form factor at 10 T to a *d*-wave model with non-local effects. Bottom: figure showing the magnitude of the superconducting gap for the same fit.

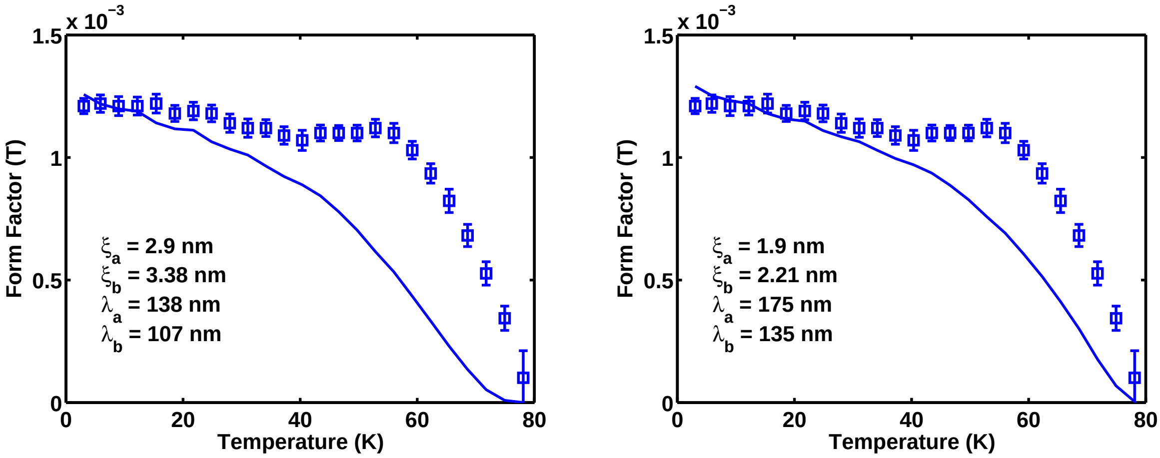

Figure 3.17: Left: figure showing the temperature dependence of the vortex lattice form factor at 10 T alongside the fit to a *d*-wave model with non-local effects where λ has been held fixed to low field values from White *et al* (White et al., 2011), while ξ has been allowed to vary. The location of these values for ξ and λ are indicated in fig. 3.16 under *Low field* λ. Right: figure showing the same temperature dependence where both λ and ξ have been allowed to vary in the model, and these values are indicted in fig. 3.16 under *Variable* λ. Values for λ and ξ are shown inset. For both plots, the model used experimental **q**-vectors.

Whilst it is obvious from fig. 3.17 that the *d*-wave model with non-local effects is unable to fit the data, we can draw several important conclusions from the problems it faces. Firstly, the increase in form factor between 40 and 55 K is a feature that the model is unable to account for, whilst the low temperature form factor accounted for reasonably well. The left hand plot in figure 3.17 shows the result from fitting the data whilst using the values for λ found to fit the lower field data. We can see that the corresponding values for the coherence length returned by this process are very close to those found in the same low field data (White et al., 2011). The right hand plot of fig. 3.17 utilised values for the penetration depth and coherence length which were allowed to vary, and we can see from fig. 3.16 that these values sit in long ‘valley’ of fit residual minimum. This represents an inherent inability for the model to find precise values for the available parameters, and this is most likely aided by the increase in form factor at around 50 K. This feature seems most likely a result of a temperature dependence to the static Debye-Waller factor observed in the field dependence of the form factor. We note that the temperature about which the form factor in fig. 3.17 shows an increase with temperature also corresponds to the irreversibility temperature seen in section 3.3.2, suggesting that the onset of the lattice improving in perfection corresponds to an increase in scattered intensity from the lattice, causing the form factor to appear to change. This strongly suggests that below the irreversibility temperature a static Debye-Waller effect is present in the diffraction from YBCO, and that it is reduced smoothly both with increasing temperature and increasing field. The presence of a DW effect which varies with temperature renders us unable to provide an accurate estimate for the penetration depth or coherence length by fitting the form factor, since the DW effect would enter into the form factor in the same manner as the core correction in the London model. This is reflected in the wide 'valley' of fit residual minimum, where a spread in values for ξ and λ provide fits of a similar quality.

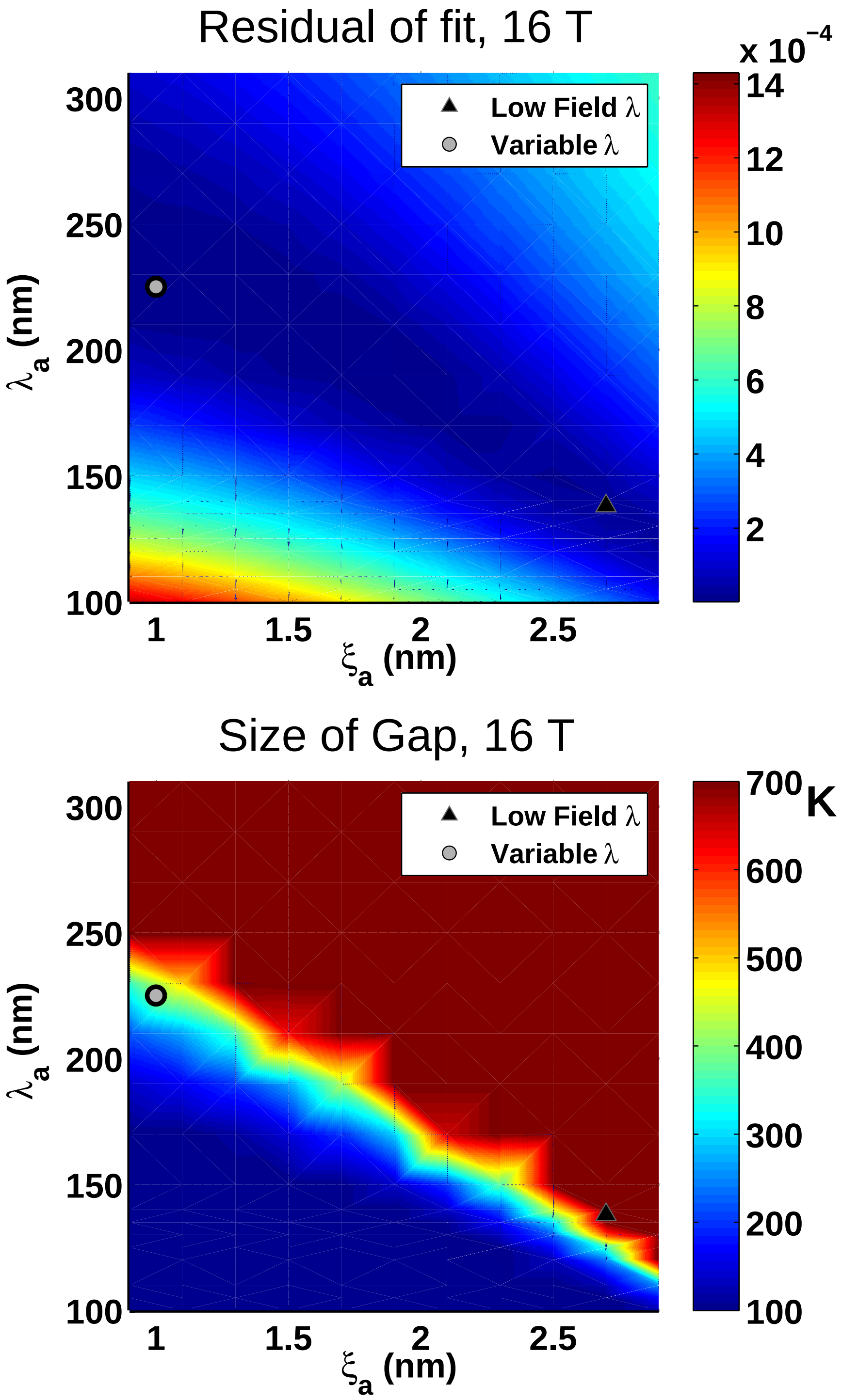

Figure 3.18: Top: figure showing the residuals of fit for the fit to the temperature dependence of the vortex lattice form factor at 16 T to a *d*-wave model. Bottom: figure showing the magnitude of the superconducting gap for the same fit. In both cases the locations of ξ_a and λ_a used in figure 3.19 is indicated.

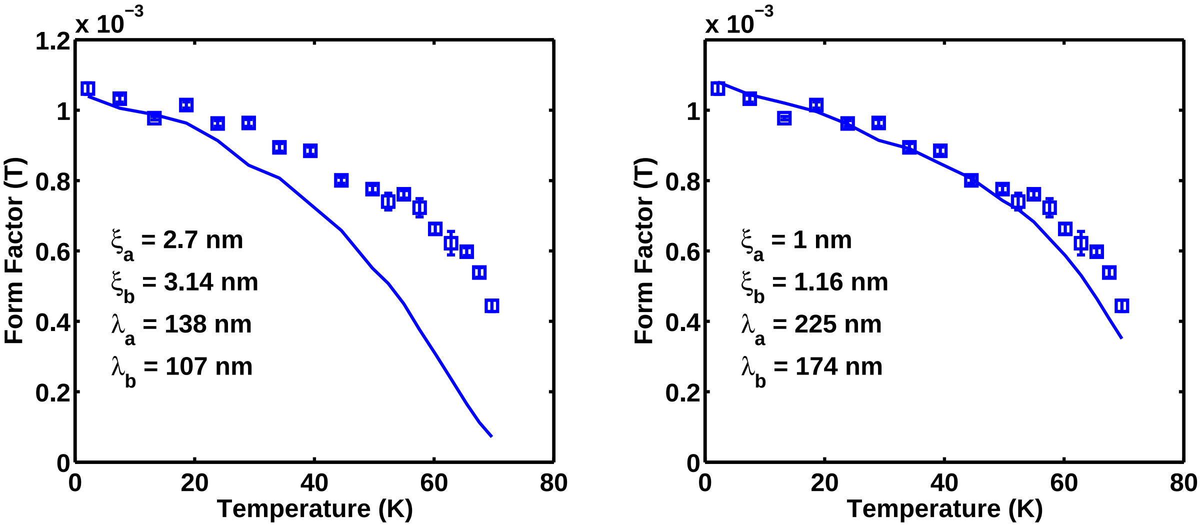

Figure 3.19: Left: Figure showing the temperature dependence of the vortex lattice form factor at 16 T alongside the fit to a d-wave model where λ has been held fixed to low field values from White *et al* (White et al., 2011), while ξ has been allowed to vary. These are indicated in figure 3.18 under *Low Field* λ. Right: Figure showing the same temperature dependence where both λ and ξ have been allowed to vary, where this is indicated in fig 3.18 under *Variable* λ. Values for λ and ξ are shown inset.

The form factor at 16 T presents a slightly different challenge to 10 T when finding an appropriate model for the temperature dependence of the form factor. Following the same general method as with 10 T, we found that the d-wave model with non-local effects was inappropriate, and that the data fitted better to the d-wave model. We see immediately in figure 3.18 that these data posses the same wide array of fit residual minima as the 10 T data. Figure 3.19 shows the results of fitting the d-wave model to the data at 16 T, with the left plot showing the results obtained when the penetration depth is held at the values obtained from low field data. Whilst the lowest temperature data are fitted to the model, the data and model separate at around 20 to 30 K. The right hand plot of fig. 3.19 gives the same data but fitted to the d-wave model with variable parameters that seem non-physical. This shows that despite the d-wave model providing a better fit to these data than the d-wave with non-local effects, it is still unable to fit the data. This suggests that, whilst the field dependence of the form factor in fig. 3.15 showed that the static DW effect was being reduced with field, at 16 T there is still a DW effect present at the lowest temperatures and, as with the form factor at 10 T, it is reduced as the temperature is increased. We note from figure 3.10 the 16 T data also shows a significant improvement of vortex lattice quality as the temperature increases.

The field and temperature dependence of the VL form factor between 10 and 16 T shows strong evidence of a static Debye-Waller effect which itself is field and temperature dependent. Diffraction from the vortex lattice does not follow the predictions from the London model, *d*-wave theory or *d*-wave theory with non-local effects, all of which were able to explain the behaviour of the vortex lattice of YBCO at lower fields (White et al., 2011). The variation in vortex lattice perfection at temperatures where the form factor deviates most strongly from theory suggests that the perfection of the lattice is correlated with this deviation, pointing towards a static DW affecting the diffraction from the vortex lattice. We note that at our highest fields the coherence length corresponding to the low temperature fit to the form factor returns an upper critical field which is much closer to the expected value than that found at lower fields, suggesting that the DW factor is nearly gone at these fields.

3.3.5 Vortex lattice melting

Figure 3.20 gives a scan of the vortex lattice form factor vs temperature at 16.7 T between 60 K and 80 K, and shows that on the approach to T_c the form factor of the vortex lattice form factor experiences a sudden drop. Data was taken by oscillation field cooling the lattice to 60 K, performing a rocking curve at 60 K, and then taking measurements on warming whilst holding the rocking angle fixed to that of the peak of the rocking curve. Rocking curves were performed every 5 K or so for several fields, and showed a linear variation in rocking curve width with temperature.

Vortex lattice melting is expected to occur when thermal fluctuations reach a critical fraction of the equilibrium vortex spacing, d_0, such that

$$\langle u_T \rangle^2 = c_L^2 d_0^2, \tag{3.5}$$

where u_T is the magnitude of thermal displacements of the vortices and c_L is the Lindemann criterion, which typically holds a value $c_L \sim 0.1 - 0.3$ for a vortex lattice (Brandt, 1989). While the loss of scattered intensity on the approach to melting is governed by the reduction in superfluid density with temperature, the sharp drop in scattered intensity from the VL is a feature of melting. The solid vortex matter, whose components occupy fixed points in the 2D lattice, melts upon crossing the temperature and field dependent melting transition. No longer possessing any of the long range order necessary to undergo Bragg diffraction, the scattered intensity of the lattice sharply drops to a level of zero within our experimental error.

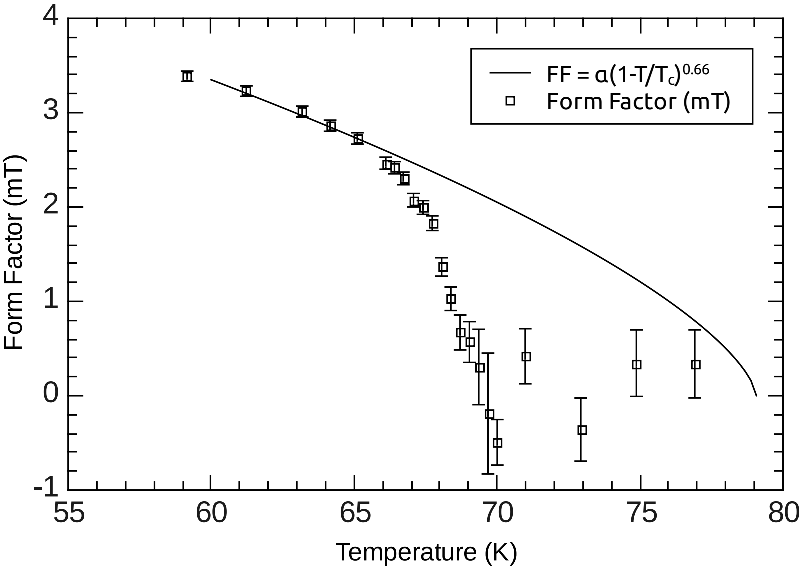

Figure 3.20: The temperature dependence of the vortex lattice form factor for 16.7 T, showing the sudden drop in intensity due to vortex lattice melting. The solid line shows the prediction for the vortex lattice form factor from the 3D XY model (Kamal et al., 1994).

In order to compare the behaviour of the vortex lattice due to melting with that expected from the reduction in superfluid density, we have followed the use of the 3D XY model by Kamal *et al* (Kamal et al., 1994), which accounts for thermal fluctuations, in providing a description of the penetration depth on the approach to T_c in a cuprate superconductor. Written in terms of the VL form factor, the model is given as

$$F_{XY}(B,T) = \alpha\big(1 - \frac{T}{T_{c2}}\big)^{n}, \tag{3.6}$$

where T_c is taken from work by Junod *et al* (Junod et al., 1997), shown in fig. 3.22, α is a constant determined by fitting the data far away from the melting transition and $n = 0.66$ (Kamal et al., 1994). Figure 3.20 shows the measured form factor at 16.7 T falls to zero earlier than is predicted by the model, indicating that the observed drop in intensity is not simply due to the reduction in superfluid density as the temperature increases. We investigated the melting transition between 8 and 16.7 T. Fig. 3.21 presents the reduced form factor, F(B,T)/F$_{XY}$(B,T) for fields between 8 T and 16.7 T. The data collected after the lattice melts show wildly varying signal with large errors. This is partly due to the difficulty in measuring a signal that is close or equal to zero, and also an artefact of presenting the reduced form factor which divides the raw data by a function that is tending to zero, so small variations in the noise above the melting line have been amplified by this process.

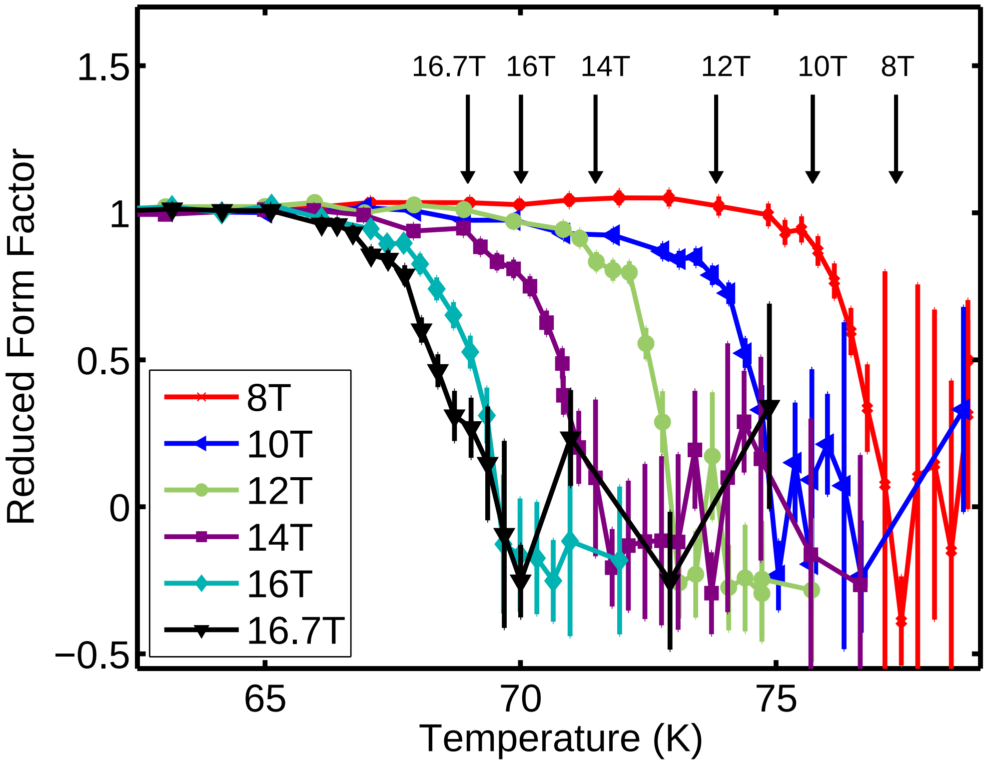

Figure 3.21: The temperature dependence of the reduced vortex lattice form factor for fields between 8 T and 16.7 T, taken on the YBCO sample before re-oxygenation. Arrows are to indicate the point where the intensity of the VL falls to zero, as determined by fitting the ‘fall off’ to a linear function. These correspond to the data in 3.22.

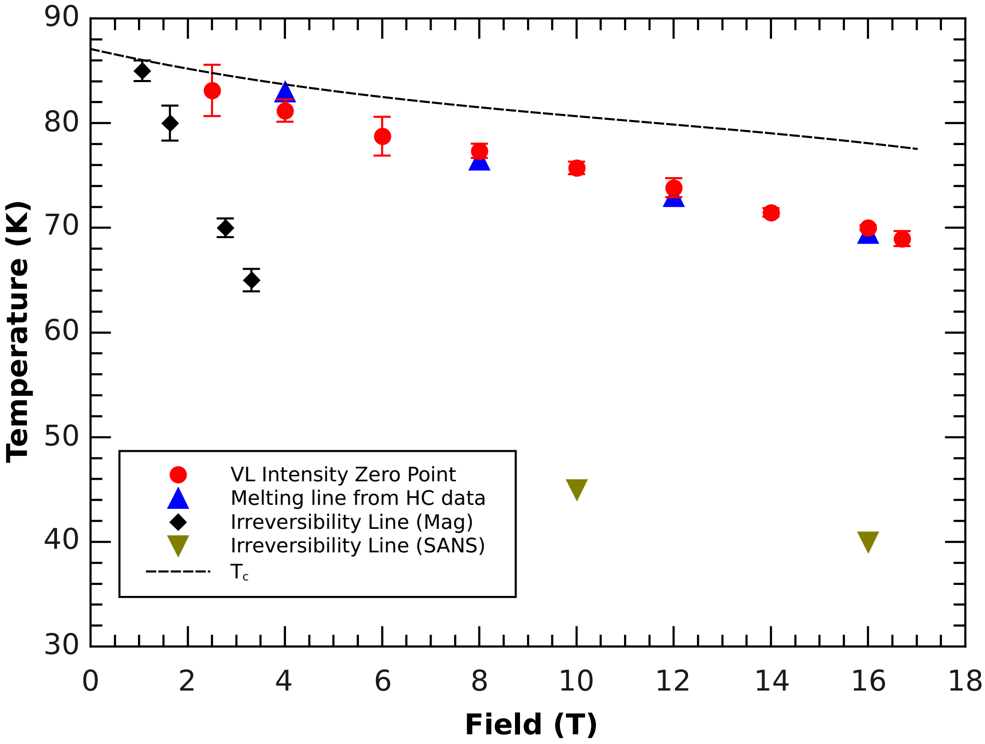

Figure 3.22: A comparison between the melting point as a function of field and temperature as derived from our SANS data and the heat capacity measurements of Roulin *et al* (Roulin et al., 1998), with the T_c from Junod *et al* (Junod et al., 1997) shown for comparison. These data show that the spikes in the heat capacity corresponding to the melting transition fall on the same line as the point in our data where the scattered intensity of the flux lattice falls to zero. Also, the irreversibility line is shown from both the magnetisation measurements performed on our crystals and the SANS data at high field.

The melting points found in this investigation follow the melting line found by heat capacity measurements (Roulin et al., 1998) for the lattice-liquid transition which are shown in figure 3.22. Previous studies have found that both first and second order transitions are possible, dependent on pinning related disorder and oxygen content for both YBCO and other cuprates, and the first order melting line has been found in $YBCO_7$ for fields up to 30 T (Roulin et al., 1998; Nishizaki and Kobayashi, 2000; Khaykovich et al., 1997). Whilst for a first order transition we expect a sharp drop in form factor as the solid melts instantaneously at the transition, our results clearly show a spread of several

Kelvin. To investigate the origin of this spread, we performed near zero field magnetisation measurements on our crystals to investigate the width of the transition, the results of which are shown in figure 3.23. We see that our crystals have a similar transition width, indicating that is is likely that the melting transition is first order and that spread seen is following the broadening of the superconducting transition. We postulated that this may be a result of a slight variance in oxygen content across the crystals comprising our mosaic, so we re-oxygenated them. This was done in an atmosphere of 100 bar of O_2 at 577 K for 150 h, as described in the discussion on the sample 3.2. Following these measurements, we performed the same melting scan done in figure 3.21, and for comparison the results are shown in figure 3.23. This shows that the width of the transition before and after re-oxygenation has not changed, and so we cannot attribute the spread in the melting line to a change in oxygen content across the mosaic. Furthermore, SQUID magnetometry measurements on the re-oxygenated sample also gave the same width as shown in fig. 3.23. We note that, while the behaviour of a first order transition in the presence of disorder is not well understood, the disorder would be expected to affect the nucleation and propagation of melting, and whether the transition is smeared is dependent on the strength of the disorder (Imry and Wortis, 1979). We can see that the rocking curve widths in fig. 3.10 near the transition temperature are close to, but greater, than the resolution width of the instrument indicating that VL pinning is still active at this temperature and some disorder must still be present.

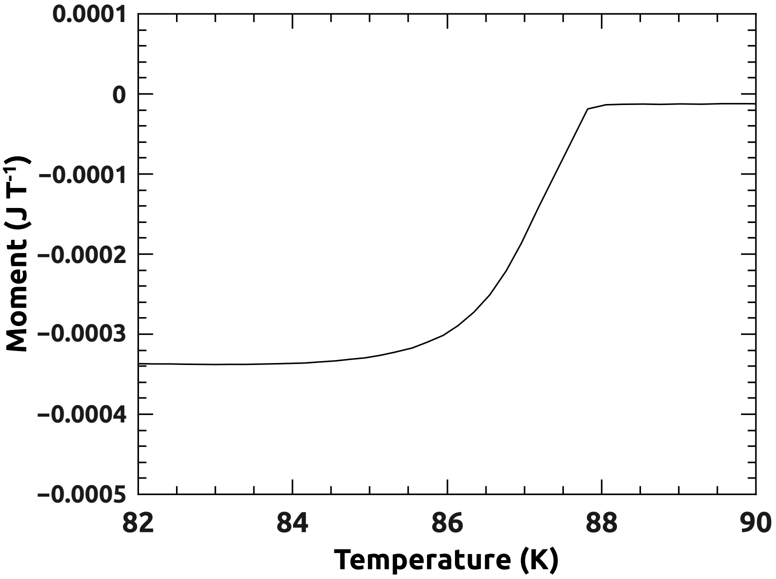

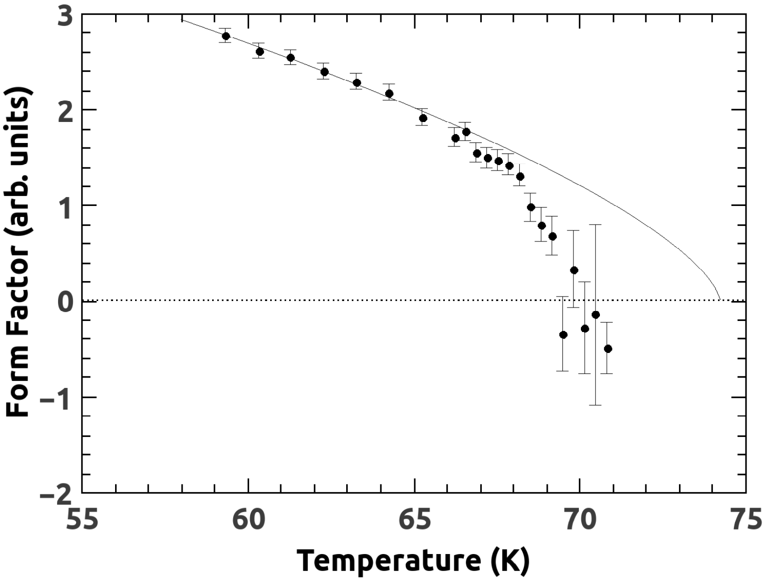

Figure 3.23: Top: Figure showing the magnetisation measurement taken at 10 Gauss using a SQUID magnetometer on the sample before re-oxygenation. Sample shows a transition width of around 2 K, which is similar to the spread in melting observed in fig 3.21. Bottom: figure showing the form factor as a function of temperature across the melting transition at 16 T after re-oxygenation of the sample. The transition shows a similar width to the sample before the re-oxygenation procedure.

Figure 3.24 gives a description of the shape of the vortex lattice Bragg reflections as a function of temperature in an applied field of 16 T. Data are from the same scan at 16 T as presented in figure 3.21. The shape of the diffraction spots is parametrised in terms of the radial and azimuthal widths of the spot, which were obtained by fitting spots to a 2D Gaussian function where the radial and azimuthal positions are given relative to the centre of the diffraction pattern. It can be seen that the Bragg reflections remain reasonably fixed in shape across the melting transition - we recall from figure 3.21 that in an applied field of 16 T the VL melted between 67 and 69 K. We expect the scattering pattern of a liquid to be a ring, diffuse both in scattering vector and azimuthal distribution, since it possesses no rotational or translational order. However, no sign of broadening in azimuthal or radial width from a liquid contribution to the diffraction can be seen in these data.

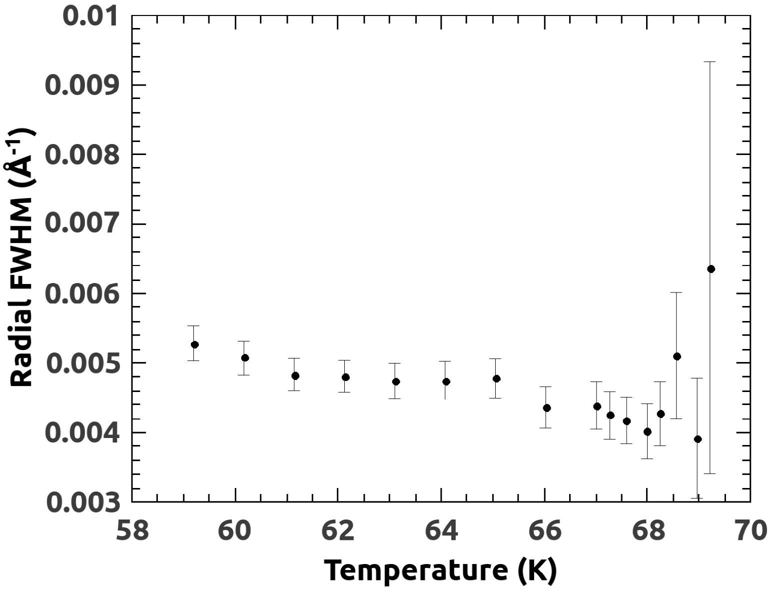

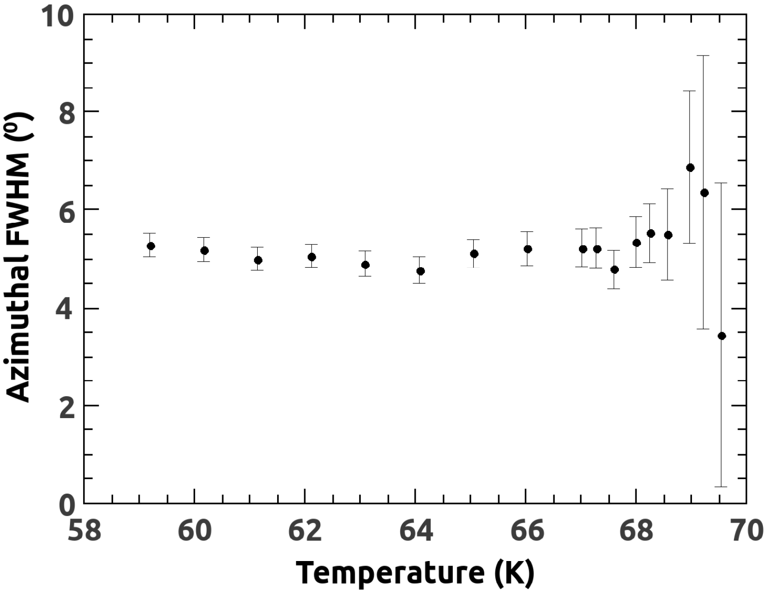

Figure 3.24: Top: Figure showing the FWHM of the radial width of the diffraction spots as a function of temperature in an applied field of 16 T on the approach to VL melting. Bottom: Figure showing the FWHM of the azimuthal width of the diffraction spots as a function of temperature for the same scan at 16 T.

In addition to searching for the contribution to scattering from the liquid component of the vortex matter during the melting transition, we can also look for the SANS signal from the vortex liquid above the transition. Should there be a scattering contribution as the liquid melts, it may be obscured by the signal from the VL and not show up as a broadening of the diffraction spots investigated in fig. 3.24. Whilst a liquid does not possess the long range order required from a solid to exhibit Bragg diffraction, we can expect the *average* inter-vortex spacing to be equivalent to the vortex spacing of the solid, since both the applied field and flux quantised vortices remain. We would expect any signal from a vortex liquid to be azimuthally invariant, since no rotational order would exist, in a similar manner to the ring-like diffraction patterns seen in the pnictides (Inosov et al., 2010), and also diffuse in $\mid \mathbf{q} \mid$ since it is only the average spacing that would be equivalent to the lattice spacing. It is obvious that the data in figure 3.21 possesses a great deal of noise just above the melting transition, and whilst this is to be expected in a data set which is being divided by a function on its approach to zero we suspected that there may be some signal from a vortex liquid in this region. Fig. 3.25 shows both the scattered intensity as a function of temperature for the 16.7 T scan alongside a plot of the intensity on the detector as a function of $\mid \mathbf{q} \mid$ at a point just above the melting transition, indicated on the graph, which focusses on the azimuthal range in which the Bragg reflections were seen. Whilst it may seem that the intensity vs temperature plot shows some sort of signal just above the melting transition, the intensity vs $\mid \mathbf{q} \mid$ shows no signal beyond the noise in the region where we expect the average inter-vortex spacing. This result is typical for all investigated fields, where we found no discernible signal above or during the melting transition which we could attribute to the vortex liquid.

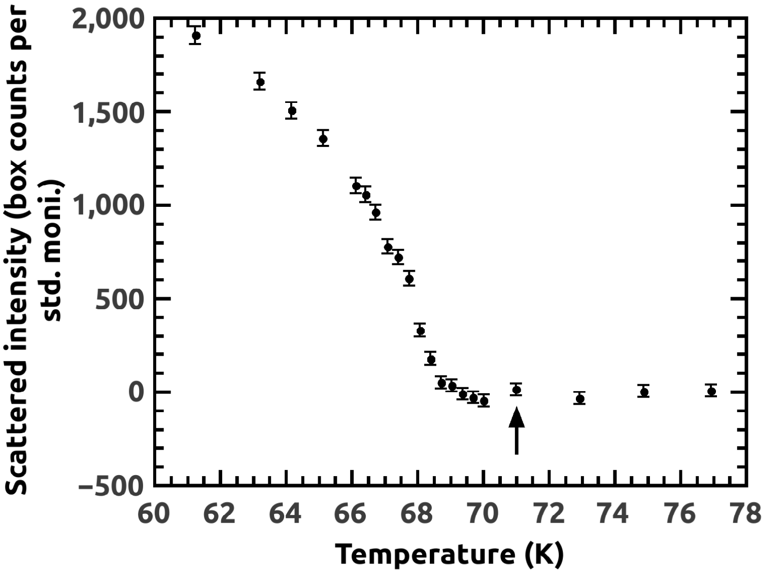

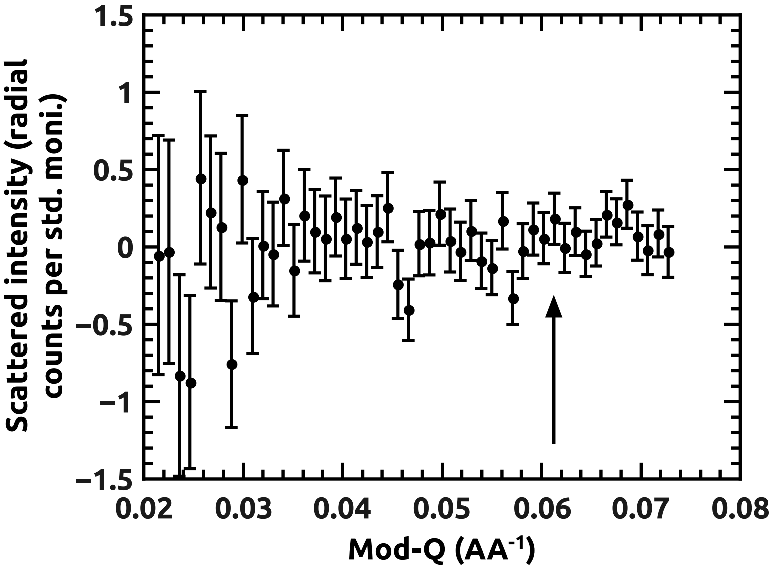

Figure 3.25: Top: Figure showing the scattered intensity into the area of the detector corresponding to the Bragg reflections of the vortex lattice at 16.7 T as a function of temperature. Arrow indicates the temperature of measurement for the right hand figure. Bottom: Figure showing the scattered intensity onto the detector as a function of scattering vector $| \mathbf{q} |$. Arrow indicates the expected $| \mathbf{q} |$ for a square lattice at 16.7 T.

In addition to the measurements discussed so far, and in an attempt to overcome the background noise when investigating a system from which we expect very weak and diffuse scattering, we performed a specific measurement dedicated to finding a signal from the vortex liquid. We rocked on to the expected Bragg angle for a vortex solid and performed long counts in both foreground and background. However, despite the long count times and use of perhaps the most intense neutron source available for this measurement we were unable to find a signal we could directly attribute to a vortex liquid. From this we can infer several properties of a vortex liquid. Either the deviations from the average inter-vortex spacing are large enough that the assumption of a weaker, more diffuse signal is too optimistic, or the correlation length along the vortices becomes so short that considering the vortex matter to be two dimensional in nature is unrealistic. In either of these cases, the scattering of neutrons from the vortex matter would be both very weak and very diffuse, leading the measurement to be indistinguishable from the background on the time-scale of our measurements.

3.3.6 Conclusions

These results represent the first microscopic study of vortex matter at fields of up to 16.7 T, both in YBCO and in superconductors as a whole. We have observed a continuation of the smooth variation in vortex lattice structure at high fields, with the VL passing through a square structure at around 12 T and continuing to vary until our maximum available field. This observation lends weight to the idea of a suppression with field of a contribution to superconductivity in YBCO from the copper oxide chains, which provide an s-wave addition to an already $d + s$ order parameter. We note, therefore, that for the VL to assume an 'accidental' square structure at around 12 T, that the contributions to the order parameter from the chain layers must possess an opposite sign to the intrinsic s-wave component of the CuO_2 planes in this orthorhombic material. Should higher field magnets for this research become available at neutron scattering facilities in the future, we may find that the lattice enters a field independent structure once the chain superconductivity has been completely suppressed.

The temperature and field dependence of scattered intensity of the vortex lattice show strong evidence of a static Debye-Waller effect arising from disorder in the lattice, suggesting that values for the coherence length obtained from lower field data may be too long. The behaviour of the form factor and perfection of the lattice as a function of both field and temperature suggest that the static DW effect is slowly reducing over our investigated field and temperature range. This is particularly noticeable in the temperature dependence of the VL form factor at 10 T, where the d-wave model with non local effects, which was successful in describing the form factor at lower fields, is completely unable to account for the unusual variation in form factor seen between 40 and 50 K. This is less noticeable at high fields, although the temperature dependence of the form factor at 16 T also eludes the d-wave model used to fit it when using physically reasonable parameters. Whilst the field and temperature dependence of the form factor, which strongly suggest the presence of a static Debye-Waller effect, is an indication of the effect of disorder in the lattice on SANS, the temperature and field dependence of the VL structure gives direct evidence of such disorder. The rocking curve width is unusually wide, with a strong temperature dependence of its width at higher temperatures. The VL structure also follows a strong temperature dependence, indicating an irreversibility temperature below which the VL is pinned to lattice defects and unable to evolve.

We have observed the melting of the vortex lattice at high fields as the temperature approaches T_c, with the transition points corresponding to the first order melting transition observed in heat capacity measurements. The lattice shows no sign of broadening or disordering across the transition, which is spread over a width of around 2 K, indicating that any scattering from a liquid component of the vortex matter is much weaker than the Bragg scattering from the VL. We do not see any signal that can be directly attributed to a vortex liquid above the melting transition, even in extended measurements of around 3 hours of counting for a single data point, suggesting that any scattering of neutrons from the vortex liquid is either too diffuse or incoherent to be observable on the time-scale of a neutron scattering experiment.

3.3.7 Further Work

To clarify the role possible oxygen deficiencies in the lattice of YBCO had in the behaviour of the VL, specifically with respect to pinning, it would be useful to investigate the low temperature behaviour of the VL in the re-oxygenated crystals. Whilst we checked the width of the melting transition with the re-oxygenated crystals, a thorough low temperature investigation was not done. Initial measurements at low fields ($\sim$ 2 T) done to align the sample suggested a more disordered VL at low fields than was found before the re-oxygenation process. It is probable that the pinning experienced by the VL in the sample has changed, and we therefore may find a change in static Debye-Waller effect, and it is possible that the observed static DW effect has been reduced or a further annealing process on these would significantly improve the situation. Further, we need to re-measure the width of the superconducting transition in the SQUID magnetometer in order to fully investigate the broadening of the melting transition, since at present we only have magnetometry data from before the re-oxygenation process. We are undertaking an investigation into the behaviour of the vortex lattice in YBCO as the field is rotated away from the **c** axis, in order to further investigate the origin and behaviour of the structure transitions observed at low field. Should pinning to the remnants of twin planes still be affecting these samples, which was indicated in the temperature dependence of the VL structure when data from the peak of the rocking curve was compared to data from the tails, rotation away from the basal plane should significantly reduce this.

Publications arising from work in this thesis

Cameron, A.S., Holmes, A.T., Blackburn, E. Forgan, E.M., White, J.S., Lim, J., Loew, T., Dewhurst, C.D. and Erb, A. *High Field SANS measurements of the Vortex Lattice in* $YBa_2Cu_3O_7$*. In preparation,* 2013.

Kawano-Furukawa, H., Bowell, C. J., White, J. S., Heslop, R. W., Cameron, A. S., Forgan, E. M., Kihou, K., Lee, C. H., Iyo, A., Eisaki, H., Saito, T., Fukazawa, H., Kohori, Y., Cubitt, R., Dewhurst, C. D., Gavilano, J. L. and Zolliker, M. *Gap in* KFe_2As_2 *studied by small-angle neutron scattering observations of the magnetic vortex lattice. Phys. Rev. B,* 84:024507, 2011.

Kawano-Furukawa, H., DeBeer-Schmitt, L., Kikuchi, H., Cameron, A. S., Holmes, A. T., Heslop, R. W., Forgan E. M., White, J. S., Gavilano, J. L., Kihou, K., Lee,C.H. , Iyo, A., Eisaki, H., Saito, T., Fukazawa, H., Kohori, Y., *Probing the anisotropic vortex lattice in the Fe-based superconductor* KFe_2As_2 *using small angle neutron scattering. Submitted Phys. Rev. B,* 2013.

Morisaki-Ishii, R. , Kawano-Furukawa, H., Cameron A. S., Lemberger, L., Blackburn, E., Holmes, A. T., Forgan, E. M., DeBeer-Schmitt, L. M., Littrell, K., Nakajima, M., Kihou, K., Lee, C. H., Iyo, A., Eisaki, E., Uchida, S., White, J. S., Gavilano, J. L., Zolliker, M. and Dewhurst, C. D. *Vortex lattice structure in* $BaFe_2(As_{0.67}P_{0.33})_2$ *studied by the small angle neutron scattering technique. In preparation,* 2013.

Publications arising from work done during this thesis

Inosov, D. S., White, J. S., Evtushinsky, D. V., Morozov, I. V., Cameron, A., Stockert, U., Zabolotnyy, V. B., Kim, T. K., Kordyuk, A. A., Borisenko, S. V., Forgan, E. M., Klingeler, R., Park, J. T., Wurmehl, S., Vasiliev, A. N., Behr, G., Dewhurst, C. D. and Hinkov, V. *Weak Superconducting Pairing and a Single Isotropic Energy Gap in Stoichiometric LiFeAs. Phys. Rev. Lett.* 104:187001, 2010.

White, J. S., Bowell, C. J., Cameron, A. S., Heslop, R.W., Mesot, J., Gavilano, J. L., Strassle, S., Maechler, L., Khasanov, R., Dewhurst, C. D., Karpinksi, J. and Forgan, E. M. *Magnetic field and temperature effects on CuO chain superconductiviy in* $YBa_2Cu_4O_8$*. In preparation,* 2013.

3.4 Other work

Aside from the work in this thesis and the various publications that have arisen either as a result of or in addition to this, there are some ongoing projects by the Condensed Matter group at the University of Birmingham in which I have been involved, but which have not yet reached publication.

An investigation was performed into the vortex structure within a current carrying niobium wire, in continuation of previous measurements (Cubitt et al., 2009), where helical vortex structures were predicted to form as a result of interaction between the self field of the current and an applied field. Here, the external field is applied parallel to the current flowing through the wire, such that the self field and applied field exist perpendicular to each other and vector addition of the fields results in a helix. The results from this experiment are still under analysis, although we saw strong indications in the initial results that the predicted helical vortex structure was formed in the wire.

In addition to the SANS investigations on $YBCO_7$, we have performed an investigation into the VL in calcium-doped YBCO. Here, the calcium replaces yttium in the lattice, resulting in greater hole doping. With a range of calcium dopings available in this project, we hope to see evidence of a doping dependence to the s-wave admixture in the order parameter of the YBCO systems.

We have begun an investigation into the VL in Nb_3Sn. Despite being a commonly used superconductor, its crystal lattice shows a structural transition between square and tetragonal above T_c (Malifert et al., 1967), and its effect on superconductivity is not well understood. We hope to gain information about the superconducting state with respect to the changes in crystal structure in these samples, and with the VL possessing great sensitivity to changes in crystal symmetry it appears to be a useful tool with which to investigate this recent discovery.

LIST OF REFERENCES

Abdel-Hafiez M, Aswartham S, Wurmehl S, Grinenko V, Hess C, Drechsler S.-L, Johnston S, Wolter A. U. B, Büchner B, Rosner H, and Boeri L. *Specific heat and upper critical fields in* KFe_2As_2 *single crystals. Phys. Rev. B*, 85:134533, 2012.

Abrikosov A. A. *On the magnetic properties of superconductors of the second group. JETP*, 5:1174, 1957.

Affleck I and Franz M. *Generalized London free energy for high-T. PRB*, 55:704–707, 1997.

Amin M. H, Affleck I, and Franz M. *Low-temperature behavior of the vortex lattice in unconventional superconductors. Physical Review B*, 58:5848–5855, 1998. ISSN 0163-1829.

Amin M. H, Franz M, and Affleck I. *Effective penetration depth in the vortex state of a d-wave superconductor. Physical review letters*, 84:5864–7, 2000. ISSN 0031-9007.

Analytis J. G, McDonald R. D, Chu J.-H, Riggs S. C, Bangura A. F, Kucharczyk C, Johannes M, and Fisher I. R. *Quantum oscillations in the parent pnictide* $BaFe_2As_2$*: Itinerant electrons in the reconstructed state. Phys. Rev. B*, 80:064507, 2009.

Anderson P. W. *The Resonating Valence Bond State in* La_2CuO_4 *and Superconductivity. Science*, 235:1196, 1987.

Anderson P. W. *The Theory of Superconductivity in the High Tc Cuprates Ch. 3.* Princeton Univ. Press, 1995.

Atkinson W. A and Carbotte J. P. *Effect of proximity coupling of chains and planes on the penetration-depth anisotropy in* $YBa_2Cu_3O_7$*. Phys. Rev. B*, 52:10601–10609, 1995.

Atkinson W. A and Sonier J. E. *Role of CuO chains in vortex core structure in* $YBa_2Cu_3O_{7-\delta}$*. Phys. Rev. B*, 77:024514, 2008.

Bardeen J, Cooper L. N, and Schrieffer J. R. *Microscopic Theory of Superconductivity. Phys. Rev.*, 106(1):162–164, 1957.

Bardeen J, Kümmel R, Jacobs A. E, and Tewordt L. *Structure of Vortex Lines in Pure Superconductors. Phys. Rev.*, 187(2):556–569, 1969.

Basov D. N, Timusk T, Dabrowski B, and Jorgensen J. D. *c -axis response of* $YBa_2Cu_4O_8$*: A pseudogap and possibility of Josephson coupling of* CuO_2 *planes. Phys. Rev. B*, 50: 3511–3514, 1994.

Bednorz J. G and Muller K. A. *Possible high Tc superconductivity in the Ba-La-Cu-O system. Zeitschrift fur Physik B Condensed Matter*, 64:189–193, 1986.

Bianchi A. D, Kenzelmann M, DeBeer-Schmitt L, White J. S, Forgan E. M, Mesot J, Zolliker M, Kohlbrecher J, Movshovich R, Bauer E. D, Sarrao J. L, Fisk Z, Petrovic C, and Eskildsen M. R. *Superconducting Vortices in* $CeCoIn_5$*: Toward the Pauli-Limiting Field. Science*, 319(5860):177–180, 2008.

Blackburn E, Chang J, Hücker M, Holmes A. T, Christensen N. B, Liang R, Bonn D. A, Hardy W. N, Rütt U, Gutowski O, Zimmermann M. v, Forgan E. M, and Hayden S. M. *X-Ray Diffraction Observations of a Charge-Density-Wave Order in Superconducting Ortho-II* $YBa_2Cu_3O_{6.54}$ *Single Crystals in Zero Magnetic Field. Phys. Rev. Lett.*, 110: 137004, 2013.

Bowell C. J. PhD thesis, School of Physics and Astronomy, University of Birmingham, 2008.

Brandt E. H. *Thermal fluctuation and melting of the vortex lattice in oxide superconductors. Phys. Rev. Lett.*, 63:1106–1109, 1989.

Brown S. P, Charalambous D, Jones E. C, Forgan E. M, Kealey P. G, Erb A, and Kohlbrecher J. *Triangular to Square Flux Lattice Phase Transition in* $YBa_2Cu_3O_7$*. Phys. Rev. Lett.*, 92(6):067004, 2004.

Campbell L. J, Doria M. M, and Kogan V. G. *Vortex lattice structures in uniaxial superconductors. Phys. Rev. B*, 38(4):2439–2443, 1988.

Caroli d. G. P. G, C. and Matricon J. *Bound Fermion states on a vortex line in a type II superconductor. Appl. Phys. Lett*, 18:427, 1964.

Carrington A and Manzano F. *Magnetic penetration depth of* MgB_2*. Physica C: Superconductivity*, 385(1-2):205 – 214, 2003. ISSN 0921-4534.

Chen H. *Coexistence of the spin-density wave and superconductivity in* $Ba_{1-x}K_xFe_2As_2$*. EPL*, Volume 85 Number 1, 2009.

Cheong S.-W, Aeppli G, Mason T. E, Mook H, Hayden S. M, Canfield P. C, Fisk Z, Clausen K. N, and Martinez J. L. *Incommensurate magnetic fluctuations in* $La_{2-x}Sr_xCuO_4$*. Phys. Rev. Lett.*, 67:1791–1794, 1991.

Christainson A.D. e. a. *Unconventional superconductivity in* $Ba_{0.6}K_{0.4}Fe_2As_2$ *from inelastic neutron scattering. Nature (London)*, 456:930, 2008.

Christen D. K, Tasset F, Spooner S, and Mook H. A. *Study of the intermediate mixed state of niobium by small-angle neutron sattering. Phys. Rev. B*, 15(9):4506–4509, 1977.

Clem J. R. *Simple Model for the Vortex Core in a Type-II Superconductor. J. Low Temp. Phys.*, 18:472, 1975.

Cooper L. N. *Bound Electron Pairs in a Degenerate Fermi Gas. Phys. Rev.*, 104(4): 1189–1190, 1956.

Corson J, Mallozzi R, Orenstein J, and and+ I. Bozovic J. N. E. *Vanishing of phase coherence in underdoped* $Bi_2Sr_2CaCu_2O_{8+\delta}$. *Nature*, 398:221, 1999.

Cubitt R, Forgan E, Paul D, Lee S, Abell J, Mook H, and Timmins P. *Neutron diffraction by the flux lattice in high-*T_c *superconductors. Physica B: Condensed Matter*, 180-181 (Part 1):377 – 379, 1992.

Cubitt R, Eskildsen M. R, Dewhurst C. D, Jun J, Kazakov S. M, and Karpinski J. *Effects of Two-Band Superconductivity on the Flux-Line Lattice in Magnesium Diboride. Phys. Rev. Lett.*, 91(4):047002, 2003.

Cubitt R, Campbell A. S, Forgan E. M, Dewhurst C. D, and Yang G. *Investigation of vortex structures in a current-carrying Nb wire. Superconductor Science and Technology*, 22(3):034014, 2009.

Damascelli A, Hussain Z, and Shen Z.-X. *Angle-resolved photoemission studies of the cuprate superconductors. Rev. Mod. Phys.*, 75:473–541, 2003.

Das P, de Bruyn Ouboter R, and K.W.Taconis. *A realization of a London-Clarke-Mendoza type refrigerator. Proc. LT9, Columbus Ohio*, pages 1253–1255, 1964.

de Gennes P. G. *Superconductivity of Metals and Alloys 2nd edition.* Addison-Wesley, 1989.

De Wilde Y, Iavarone M, Welp U, Metlushko V, Koshelev A. E, Aranson I, Crabtree G. W, and Canfield P. C. *Scanning Tunneling Microscopy Observation of a Square Abrikosov Lattice in* $LuNi_2B_2C$. *Phys. Rev. Lett.*, 78:4273–4276, 1997.

Dewhurst C. D. *http://www.ill.eu/ instruments -support /instruments-groups /groups /lss /grasp /home/.*

Ding H, Norman M. R, Campuzano J. C, Randeria M, Bellman A. F, Yokoya T, Takahashi T, Mochiku T, and Kadowaki K. *Angle-resolved photoemission spectroscopy study of the superconducting gap anisotropy in* $Bi_2Sr_2CaCu_2O_{8+x}$. *Phys. Rev. B*, 54:R9678–R9681, 1996.

Dong J. K, Zhou S. Y, Guan T. Y, Zhang H, Dai Y. F, Qiu X, Wang X. F, He Y, Chen X. H, and Li S. Y. *Quantum Criticality and Nodal Superconductivity in the FeAs-Based Superconductor* KFe_2As_2. *Phys. Rev. Lett.*, 104:087005, 2010.

Emery V. J and Kivelson S. A. *Importance of phase fluctuations in superconductors with small superfluid density. Nature*, 374:464, 1995.

Evtushinsky D. V, Inosov D. S, Zabolotnyy V. B, Koitzsch A, Knupfer M, Büchner B, Viazovska M. S, Sun G. L, Hinkov V, Boris A. V, Lin C. T, Keimer B, Varykhalov A, Kordyuk A. A, and Borisenko S. V. *Momentum dependence of the superconducting gap in* $Ba_{1-x}K_xFe_2As_2$. *Phys. Rev. B*, 79:054517, 2009.

Fernandes R. M and Schmalian J. *Competing order and nature of the pairing state in the iron pnictides. Phys. Rev. B*, 82:014521, Jul 2010.

Fischer O, Renner C, Maggio-Aprile I, Erb A, Walker E, Revaz B, and Genoud J.-Y. *Tunneling spectroscopy and STS observation of vortices on high temperature superconductors. Physica C: Superconductivity*, Volumes 282-287:315–318, 1997.

Franz M, Affleck I, and Amin M. H. *Theory of Equilibrium Flux Lattices in Unconventional Superconductors. Physical Review Letters*, 79(8):1555–1558, 1997.

Fröhlich H. *Theory of the Superconducting State. I. The Ground State at the Absolute Zero of Temperature. Phys. Rev.*, 79(5):845–856, 1950.

Fukazawa H, Yamada Y, Kondo K, Saito T, Kohori Y, Kuga K, Matsumoto Y, Nakatsuji S, Kito H, Shirage P. M, Kihou K, Takeshita N, Lee C.-H, Iyo A, and Eisaki H. *Possible Multiple Gap Superconductivity with Line Nodes in Heavily Hole-Doped Superconductor* KFe_2As_2 *Studied by* ^{75}As *Nuclear Quadrupole Resonance and Specific Heat. Journal of the Physical Society of Japan*, 78(8):083712, 2009.

Gilardi R, Mesot J, Drew A, Divakar U, Lee S. L, Forgan E. M, Zaharko O, Conder K, Aswal V. K, Dewhurst C. D, Cubitt R, Momono N, and Oda M. *Direct Evidence for an Intrinsic Square Vortex Lattice in the Overdoped High-* T_c *Superconductor* $La_{1.83}Sr_{0.17}CuO_{4+\delta}$. *Phys. Rev. Lett.*, 88:217003, 2002.

Ginzburg V. L and Landau L. D. *On the Theory of superconductivity. Zh. Eksp. Teor. Fiz.*, 20:1064–1082, 1950.

Gor'Kov L. *On the Energy Spectrum of Superconductors. JETP*, 34:735–739, 1958.

Gorter G.J. C. H. *On supraconductivity. Physica*, 1:306–320, 1934.

Graser S, Kemper A. F, Maier T. A, Cheng H.-P, Hirschfeld P. J, and Scalapino D. J. *Spin fluctuations and superconductivity in a three-dimensional tight-binding model for* $BaFe_2As_2$. *Phys. Rev. B*, 81:214503, 2010.

Hardy W. N, Bonn D. A, Morgan D. C, Liang R, and Zhang K. *Precision measurements of the temperature dependence of* λ *in* $YBa_2Cu_3O_{6.95}$*: Strong evidence for nodes in the gap function. Phys. Rev. Lett.*, 70:3999–4002, 1993.

Hashimoto K, Shibauchi T, Kasahara S, Ikada K, Tonegawa S, Kato T, Okazaki R, van der Beek C. J, Konczykowski M, Takeya H, Hirata K, Terashima T, and Matsuda Y. *Microwave Surface-Impedance Measurements of the Magnetic Penetration Depth in Single Crystal* $Ba_{1-x}K_xFe_2As_2$ *Superconductors: Evidence for a Disorder-Dependent Superfluid Density. Phys. Rev. Lett.*, 102:207001, 2009.

Hashimoto K, Serafin A, Tonegawa S, Katsumata R, Okazaki R, Saito T, Fukazawa H, Kohori Y, Kihou K, Lee C. H, Iyo A, Eisaki H, Ikeda H, Matsuda Y, Carrington A, and Shibauchi T. *Evidence for superconducting gap nodes in the zone-centered hole bands of* KFe_2As_2 *from magnetic penetration-depth measurements. Phys. Rev. B*, 82:014526, 2010a.

Hashimoto K, Yamashita M, Kasahara S, Senshu Y, Nakata N, Tonegawa S, Ikada K, Serafin a, Carrington A, Terashima T, Ikeda H, Shibauchi T, and Matsuda Y. *Line* *nodes in the energy gap of superconducting $BaFe_2As_{1-x}P_x)_2$ single crystals as seen via penetration depth and thermal conductivity. Physical Review B*, 81(22):220501, 2010b.

Heyes S. J. *www.ncl.ox.ac.uk/icl/heyes/structureofsolids/lecture4/lec4.html.*

Hirschfeld P. J, Putikka W. O, and Scalapino D. J. *Microwave conductivity of d -wave superconductors. Phys. Rev. Lett.*, 71:3705–3708, 1993.

Holmes A. *On the Baysian treatment of diffraction patterns. In preparation*, 2013.

Hook J and Hall H. *Solid State Physics.* Wiley, 1991.

Hsieh D, Xia Y, Wray L, Qian D, Gomes K, Yazdani A, Chen G, Luo J, Wang N, and Hasan M. *Experimental determination of the microscopic origin of magnetism in parent iron pnictides. arXiv*, page 0812.2289.

Hu W. Z, Dong J, Li G, Li Z, Zheng P, Chen G. F, Luo J. L, and Wang N. L. *Origin of the Spin Density Wave Instability in AFe_2As_2 (A=Ba,Sr) as Revealed by Optical Spectroscopy. Phys. Rev. Lett.*, 101:257005, 2008.

Huang Q, Qiu Y, Bao W, Green M. A, Lynn J. W, Gasparovic Y. C, Wu T, Wu G, and Chen X. H. *Neutron-Diffraction Measurements of Magnetic Order and a Structural Transition in the Parent $BaFe_2As_2$ Compound of FeAs-Based High-Temperature Superconductors. Phys. Rev. Lett.*, 101:257003, 2008.

Ichioka M, Hayashi N, Enomoto N, and Machida K. *Vortex structure in d-wave superconductors. Phys. Rev. B*, 53(22):316–326, 1996.

Ichioka M, Enomoto N, and Machida K. *Vortex Lattice Structure in a $d_{x^2-y^2}$-Wave Superconductor. Journal of the Physical Society of Japan*, 66(12):3928–3943, 1997.

Ichioka M, Hasegawa A, and Machida K. *Field dependence of the vortex structure in d-wave and s-wave superconductors. Phys. Rev. B*, 59(13):8902–8916, 1999.

Imry Y and Wortis M. *Influence of quenched impurities on first-order phase transitions. Phys. Rev. B*, 19:3580–3585, 1979.

Inosov D. S, White J. S, Evtushinsky D. V, Morozov I. V, Cameron A, Stockert U, Zabolotnyy V. B, Kim T. K, Kordyuk A. A, Borisenko S. V, Forgan E. M, Klingeler R, Park J. T, Wurmehl S, Vasiliev A. N, Behr G, Dewhurst C. D, and Hinkov V. *Weak Superconducting Pairing and a Single Isotropic Energy Gap in Stoichiometric LiFeAs. Phys. Rev. Lett.*, 104(18):187001, 2010.

Ishida K, Nakai Y, and Hosono H. *To What Extent Iron-Pnictide New Superconductors Have Been Clarified: A Progress Report. Journal of the Physical Society of Japan*, 78 (6):062001, 2009.

Ishikado M, Nagai Y, Kodama K, Kajimoto R, Nakamura M, Inamura Y, Wakimoto S, Nakamura H, Machida M, Suzuki K, Usui H, Kuroki K, Iyo A, Eisaki H, Arai M, and Shamoto S.-i. *$s_\pm$-like spin resonance in the iron-based nodal superconductor $BaFe_2(As_{0.65}P_{0.35})_2$ observed using inelastic neutron scattering. Phys. Rev. B*, 84: 144517, 2011.

Jacobs T, Sridhar S, Li Q, Gu G. D, and Koshizuka N. *In-Plane and c−Axis Microwave Penetration Depth of $Bi_2Sr_2Ca_1Cu_2O_{8+\delta}$ Crystals. Phys. Rev. Lett.*, 75:4516–4519, 1995.

Jiang S, Xing H, Xuan G, Wang C, Ren Z, Feng C, Dai J, Xu Z, and Cao G. *Superconductivity up to 30 K in the vicinity of the quantum critical point in $BaFe_2(As_{1-x}P_x)_2$. J. Phys.: Condens. Matter*, 21:382203, 2009.

Jorgensen J. D, Veal B. W, Paulikas A. P, Nowicki L. J, Crabtree G. W, Claus H, and Kwok W. K. *Structural properties of oxygen-defficent $YBa_2Cu_3O_{7-\delta}$. Phys. Rev. B*, 41 (4):1863, 1990.

Junod A, Roulin M, Genoud J. Y, Revaz B, Erb A, and Walker E. *Specific heat peaks observed up to* 16 *T on the melting line of the vortex lattice in $YBa_2Cu_3O_7$. Physica C: Superconductivity*, 275(3-4):245–258, 1997. ISSN 0921-4534.

Kamal S, Goldenfeld N, Hirschfeld P. J, Liang R, and Hardy W. N. *Penetration Depth Measurements of 3D XY Critical Behaviour in $YBa_2Cu_3O_{6.95}$ Crystals. Phys. Rev. Lett.*, 73(13):1845–1848, 1994.

Kamihara Y, Hiramatsu H, Hirano M, Kawamura R, Yanagi H, Kamiya T, and Hosono H. *Iron-Based Layered Superconductor LaOFeP. Journal of the American Chemical Society*, 128(31):10012–10013, 2006. PMID: 16881620.

Kamihara Y, Watanabe T, Hirano M, and Hosono H. *Iron-Based Layered Superconductor LaOFFeAs with Tc = 26 K. Journal of the American Chemical Society*, 130(11):3296–3297, 2008.

Kasahara S, Shibauchi T, Hashimoto K, Ikada K, Tonegawa S, Okazaki R, Shishido H, Ikeda H, Takeya H, Hirata K, Terashima T, and Matsuda Y. *Evolution from non-Fermi- to Fermi-liquid transport via isovalent doping in $BaFe_2(As_{1-x}P_x)_2$ superconductors. Phys. Rev. B*, 81:184519, 2010.

Kawano-Furukawa H, Ishida Y, Yano F, Nagatomo R, Noda A, Nagata T, Ohira-Kawamura S, Kobayashi C, Yoshizawa H, Littrell K, Winn B. L, Furukawa N, and Takeya H. *Creation of vortices by ferromagnetic order in. Physica C: Superconductivity*, 470:S716–S718, 2010. ISSN 09214534.

Kawano-Furukawa H, Bowell C. J, White J. S, Heslop R. W, Cameron A. S, Forgan E. M, Kihou K, Lee C. H, Iyo A, Eisaki H, Saito T, Fukazawa H, Kohori Y, Cubitt R, Dewhurst C. D, Gavilano J. L, and Zolliker M. *Gap in KFe_2As_2 studied by small-angle neutron scattering observations of the magnetic vortex lattice. Phys. Rev. B*, 84:024507, 2011.

Kawano-Furukawa H, DeBeer-Schmitt L, Kikuchi H, Cameron A. S, Holmes A. T, Heslop R. W, Forgan E. M, White J. S, Gavilano J. L, Kihou K, Lee C, Iyo A, Eisaki H, Saito T, Fukazawa H, and Kohori Y. *Probing the anisotropic vortex lattice in the Fe-based superconductor KFe_2As_2 using small angle neutron scattering. Phys. Rev. B, submitted*, 2013.

Kealey P. G, Charalambous D, Forgan E. M, Lee S. L, Johnson S. T, Schleger P, Cubitt R, Paul D. M, Aegerter C. M, Tajima S, and Rykov A. I. *Transverse-field components of the flux-line lattice in the anisotropic superconductor* $YBa_2Cu_3O_{7-\delta}$. *Physical Review B*, 64(17):1–4, 2001. ISSN 0163-1829.

Keimer B, Shih W. Y, Erwin R. W, Lynn J. W, Dogan F, and Aksay I. A. *Vortex Lattice Symmetry and Electronic Structure in* $YBa_2Cu_34O_7$. *Phys. Rev. Lett.*, 73:3459–3462, 1994.

Ketterson J and Song S. *Superconductivity.* Cambridge University Press, 1999.

Khaykovich B, Konczykowski M, Zeldov E, Doyle R. A, Majer D, Kes P. H, and Li T. W. *Vortex-matter phase transitions in* $Bi_2Sr_2CaCu_2O_8$*: Effects of weak disorder. Phys. Rev. B*, 56:R517–R520, 1997.

Kirtley J. R. *Angle-resolved phase-sensitive determination of the in-plane gap symmetry in* $YBa_2Cu_3O_{7-\delta}$. *Nature Physics*, 2.3:190, 2005.

Kleiner W. H, Roth L. M, and Autler S. H. *Bulk Solution of Ginzburg-Landau Equations for Type II Superconductors: Upper Critical Field Region. Phys. Rev.*, 133(5A):A1226–A1227, 1964.

Klintberg L. E, Goh S. K, Kasahara S, Nakai Y, Ishida K, Sutherland M, Shibauchi T, Matsuda Y, and Terashima T. *Chemical Pressure and Physical Pressure in* $BaFe_2(As_{1-x}P_x)_2$. *Journal of the Physical Society of Japan*, 79(12):123706, 2010.

Kogan V. G. *London approach to anisotropic type-II superconductors. Phys. Rev. B*, 24: 1572–1575, 1981.

Kogan V. G and Miranović P. *Vortex lattices in cubic superconductors. Phys. Rev. Lett.*, pages 741–744, 1997.

Kogan V. G, Gurevich A, Cho J. H, Johnston D. C, Xu M, Thompson J. R, and Martynovich A. *Nonlocal electrodynamics and low-temperature magnetization of clean high* κ *superconductors. Phys. Rev. B*, 54(17):12386–12396, 1996.

Kogan V. G, Bullock M, Harmon B, Miranović P, Dobrosavljevic-acute Grujic-acute L, Gammel P. L, and Bishop D. J. *Vortex lattice transitions in borocarbides. Physical Review B*, 55(14):R8693–R8696, 1997. ISSN 0163-1829.

Kontani H and Onari S. *Orbital-Fluctuation-Mediated Superconductivity in Iron Pnictides: Analysis of the Five-Orbital Hubbard-Holstein Model. Phys. Rev. Lett.*, 104:157001, 2010.

Kosztin I and Leggett A. J. *Nonlocal Effects on the Magnetic Penetration Depth in d-Wave Superconductors. Phys. Rev. Lett.*, 79(1):135–138, 1997.

Krishana K, Ong N. P, Li Q, Gu G. D, and Koshizuka N. *Plateaus Observed in the Field Profile of Thermal Conductivity in the Superconductor* $Bi_2Sr_2CaCu_2O_8$. *Science*, 83: 277, 1997.

Kuroki K, Usui H, Onari S, Arita R, and Aoki H. *Pnictogen height as a possible switch between high-T_c nodeless and low-T_c nodal pairings in the iron-based superconductors. Phys. Rev. B*, 79:224511, 2009.

Laver M and Forgan E. M. *Magnetic fluc lines in type-II superconductors and the 'hairy ball' theorem. Nature Communications*, 1:45, 2010.

Lee C.-H, Iyo A, Eisaki H, Kito H, Fernandez-Diaz M. T, Ito T, Kihou K, Matsuhata H, Braden M, and Yamada K. *Effect of Structural Parameters on Superconductivity in Fluorine-Free $LnFeAsO_{1-y}$ (Ln = La, Nd). Journal of the Physical Society of Japan*, 77(8):083704, 2008.

Lee S.-F, Morgan D. C, Ormeno R. J, Broun D. M, Doyle R. A, Waldram J. R, and Kadowaki K. *a-b Plane Microwave Surface Impedance of a High-Quality $Bi_2Sr_2CaCu_2O_8$ Single Crystal. Phys. Rev. Lett.*, 77:735–738, 1996.

Lin C, Zhou W, and Liang W. *Growth of large and untwinned single crystal of YBCO. Physica C*, 195:291–300, 1992.

Liu R.H. e. a. *A large iron isotope effect in $SmFeAsO_{1-x}F_x$ and $Ba_{1-x}K_xFe_2As_2$. Nature (London)*, 459:64, 2009.

London F and London H. *The Electromagnetic Equations of the Supraconductor. Proceedings of the Royal Society of London. Series A, Mathematical and Physical Sciences*, 149(866):pp. 71–88, 1935. ISSN 00804630.

London H. *Proc. Internat. Conf. Low Temperature Physics,Clarendon, Oxford*, page 157, 1951.

Maeda H, Tanaka Y, Fukutomi M, and Asano T. *A New High-T_c Oxide Superconductor without a Rare Earth Element. Japanese Journal of Applied Physics*, 27:L209–L210, 1988.

Maggio-Aprile I, Renner C, Erb A, Walker E, and Fischer O. *Critical currents approaching the depairing limit at a twin boundary in $YBa_2Cu_3O_{7-\delta}$. Nature*, 390:487, 1997.

Maiti S, Korshunov M. M, Maier T. A, Hirschfeld P. J, and Chubukov A. V. *Evolution of the Superconducting State of Fe-Based Compounds with Doping. Phys. Rev. Lett.*, 107: 147002, 2011.

Malifert R, Batterman B. W, and Hanak J. J. *Phys. Lett.*, 24A:315, 1967.

Mason T. E, Aeppli G, and Mook H. A. *Magnetic dynamics of superconducting $La_{1.86}Sr_{0.14}CuO_4$. Phys. Rev. Lett.*, 68:1414–1417, 1992.

Mazin I. I, Singh D. J, Johannes M. D, and Du M. H. *Unconventional Superconductivity with a Sign Reversal in the Order Parameter of $LaFeAsO_{1-x}F_x$. Phys. Rev. Lett.*, 101: 057003, 2008.

Mazin I and Schmalian J. *Pairing symmetry and pairing state in ferropnictides: Theoretical overview. Physica C: Superconductivity*, 469(9-12):614 – 627, 2009. ISSN 0921-4534.

Meissner W and Ochsenfeld R. *Ein neuer Effekt bei Eintritt der Supraleitfahigkeit. Naturwissenschaften*, 21:787–788, 1933. ISSN 0028-1042.

Mizuguchi Y, Hara Y, Deguchi K, Tsuda S, Yamaguchi T, Takeda K, Kotegawa H, Tou H, and Takano Y. *Anion height dependence of T_c for the Fe-based superconductor. Superconductor Science and Technology*, 23(5):054013, 2010.

Morisaki-Ishii R, Kawano-Furukawa H, Cameron A. S, Lemberger L, Blackburn E, Holmes A. T, Forgan E. M, DeBeer-Schmitt L. M, Littrell K, Nakajima M, Kihou K, Lee C. H, Iyo A, Eisaki E, Uchida S, White J. S, Gavilano J. L, and Zolliker M. *Vortex lattice structure in $BaFe_2(As_{0.67}P_{0.33})_2$ studied by the small angle neutron scattering technique. In preparation*, 2013.

Nakai N, Miranović P, Ichioka M, and Machida K. *Reentrant Vortex Lattice Transformation in Fourfold Symmetric Superconductors. Physical Review Letters*, 89(23):23–26, 2002. ISSN 0031-9007.

Nakai Y, Iye T, Kitagawa S, Ishida K, Kasahara S, Shibauchi T, Matsuda Y, and Terashima T. *^{31}P and ^{75}As NMR evidence for a residual density of states at zero energy in superconducting $BaFe_2(As_{0.67}P_{0.33})_2$. Phys. Rev. B*, 81:020503, 2010.

Nishizaki T and Kobayashi N. *Vortex-matter phase diagram in $YBa_2Cu_3O_y$. Superconductor Science and Technology*, 13:1, 2000.

Okazaki K, Ota Y, Kotani Y, Malaeb W, Ishida Y, Shimojima T, Kiss T, Watanabe S, Chen C, Kihou K, Lee C. H, Iyo A, Eisaki H, Saito T, Fukazawa H, Kohori Y, Hashimoto K, Shibauchi T, Matsuda Y, Ikeda H, and Miyahara H. *Octet-Line Node Structure Parameter in KFe_2As_2. Science*, 337:1314–1317, 2012.

Onnes H. K. *On the Sudden Rate at Which the Resistance of Mercury Disappears. Comm. Leiden.*, 1911.

Orenstein J and Millis A. J. *Advances in the Physics of High-Temperature Superconductivty. Science*, 288:468, 2000.

Orenstein J, Thomas G. A, Millis A. J, Cooper S. L, Rapkine D. H, Timusk T, Schneemeyer L. F, and Waszczak J. V. *Frequency- and temperature-dependent conductivity in $YBa_2Cu_3O_{6+x}$ crystals. Phys. Rev. B*, 42:6342–6362, 1990.

Osborn R, Rosenkranz S, Goremychkin E, and Christianson A. *Inelastic neutron scattering studies of the spin and lattice dynamics in iron arsenide compounds. Physica C: Superconductivity*, 469(9-12):498 – 506, 2009. ISSN 0921-4534.

Paul D. M, Tomy C. V, Aegerter C. M, Cubitt R, Lloyd S. H, Forgan E. M, Lee S. L, and Yethiraj M. *Nonlocal Effects and Vortex Lattice Transitions in YNi_2B_2C. Phys. Rev. Lett.*, 80:1517–1520, 1998.

Pippard A. *An Experimental and Theoretical Study of the Relation between Magnetic Field and Current in a Superconductor. Proc. Roy. Soc. (London)*, A216:547, 1953.

Prozorov R and Giannetta R. W. *Magnetic penetration depth in unconventional superconductors. Superconductor Science and Technology*, 19(8):R41, 2006.

Rotter M, Tegel M, and Johrendt D. *Superconductivity at 38 K in the Iron Arsenide* $(Ba_{1-x}K_x)Fe_2As_2$. *Phys. Rev. Lett.*, 101(10):107006, 2008.

Roulin M, Junod A, Erb A, and Walker E. *Calorimetric Transitions on the Melting Line of the Vortex System as a Function of Oxygen Deficiency in High-Purity* $YBa_2Cu_3O_x$. *Phys. Rev. Lett.*, 80:1722–1725, 1998.

Sachdev S. *Quantum Criticality: Competing Ground States in Low Dimensions. Science*, 288:475, 2000.

Sasmal K, Lv B, Lorenz B, Guloy A. M, Chen F, Xue Y.-Y, and Chu C.-W. *Superconducting Fe-Based Compounds* $(A_{1-x}Sr_x)Fe_2As_2$ *with A=K and Cs with Transition Temperatures up to 37 K. Phys. Rev. Lett.*, 101(10):107007, 2008.

Sato T, Nakayama K, Sekiba Y, Richard P, Xu Y.-M, Souma S, Takahashi T, Chen G. F, Luo J. L, Wang N. L, and Ding H. *Band Structure and Fermi Surface of an Extremely Overdoped Iron-Based Superconductor* KFe_2As_2. *Phys. Rev. Lett.*, 103(4):047002, 2009.

Schiff L. I. *Quantum Mechanics.* McGraw-Hill, 3rd Edition, 1968.

Schulz H. J. *Incommensurate antiferromagnetism in the two-dimensional Hubbard model. Phys. Rev. Lett.*, 64:1445–1448, 1990.

Scientific A. URL `http://www.asscientific.com /products /cryostats /index.html`.

Sebastian S. E, Gillett J, Harrison N, Lau P. H. C, Singh D. J, Mielke C. H, and Lonzarich G. G. *Quantum oscillations in the parent magnetic phase of an iron arsenide high temperature superconductor. Journal of Physics: Condensed Matter*, 20(42):422203, 2008.

Sefat A. S, Jin R, McGuire M. A, Sales B. C, Singh D. J, and Mandrus D. *Superconductivity at 22 K in Co-Doped* $BaFe_2As_2$ *Crystals. Phys. Rev. Lett.*, 101(11):117004, 2008.

Shen Z. X and Dessau D. *Electronic structure and photoemission studies of late transition-metal oxides -Mott insulators and high-temperature superconductors. Physics Reports*, 253:1, 1995.

Shibata K, Maki M, Nishizaki T, and Kobayashi N. *Quasiparticle spectra and their spatial variation on* $YBa_2Cu_3O_y$ *by scanning tunneling spectroscopy. Physica C: Superconductivity*, 388-389:277–278, 2003a.

Shibata K, Maki M, Nishizaki T, and Kobayashi N. *Scanning tunneling spectroscopy studies on vortices in* $YBa_2Cu_3O_y$ *single crystals. Physica C*, 392:323, 2003b.

Shimojima T, Sakaguchi F, Ishizaka K, Ishida Y, Kiss T, Okawa M, Togashi T, Chen C, Watanabe S, Arita M, Shimada K, Namatame H, Taniguchi M, Ohgushi K, Kasahara S, Terashima T, Shibauchi T, Matsuda Y, Chainani a, and Shin S. *Orbital-independent superconducting gaps in iron pnictides. Science (New York, N.Y.)*, 332(6029):564–7, 2011. ISSN 1095-9203.

Shirage P. M, Kihou K, Miyazawa K, Lee C.-H, Kito H, Eisaki H, Yanagisawa T, Tanaka Y, and Iyo A. *Inverse Iron Isotope Effect on the Transition Temperature of the Ba,K)*Fe_2As_2 *Superconductor. Phys. Rev. Lett.*, 103:257003, 2009.

Shirage P. M, Miyazawa K, Kihou K, Kito H, Yoshida Y, Tanaka Y, Eisaki H, and Iyo A. *Absence of an Appreciable Iron Isotope Effect on the Transition Temperature of the Optimally Doped* $SmFeAsO_{1-y}$ *Superconductor. Phys. Rev. Lett.*, 105:037004, 2010.

Shiraishi J, Kohmoto M, and Maki K. *Vortex lattice transition in d-wave superconductors. Physical Review B*, 59(6):4497–4503, 1999.

Shishido H, Bangura A. F, Coldea A. I, Tonegawa S, Hashimoto K, Kasahara S, Rourke P. M. C, Ikeda H, Terashima T, Settai R, Onuki Y, Vignolles D, Proust C, Vignolle B, McCollam A, Matsuda Y, Shibauchi T, and Carrington A. *Evolution of the Fermi Surface of* $BaFe_2(As_{1-x}P_x)_2$ *on Entering the Superconducting Dome. Physical Review Letters*, 104(5):057008, 2010.

Singh D. J. *Electronic structure and doping in* $BaFe_2As_2$ *and LiFeAs: Density functional calculations. Phys. Rev. B*, 78(9):094511, 2008.

Soininen P. I, Kallin C, and Berlinsky A. J. *Structure of a vortex line in a* $d_{x^2-y^2}$ *superconductor. Phys. Rev. B*, 50(18):13883, 1994.

Sosolik C. E, Stroscio J. A, Stiles M. D, Hudson E. W, Blankenship S. R, Fein A. P, and Celotta R. J. *Real-space imaging of structural transitions in the vortex lattice of* V_3Si. *Phys. Rev. B*, 68:140503, 2003.

Squires G. L. *Introduction to the Theory of Thermal Neutron Scattering.* Dover, 1st edition., 1996.

Steglich F, Aarts J, Bredl C. D, Lieke W, Meschede D, Franz W, and Schäfer H. *Superconductivity in the Presence of Strong Pauli Paramagnetism:* $CeCu_2Si_2$. *Phys. Rev. Lett.*, 43(25):1892–1896, 1979.

Suzuki K, Usui H, and Kuroki K. *Possible Three-Dimensional Nodes in the s± Superconducting Gap of* $BaFe_2(As_{1-x}P_x)_2$. *Journal of the Physical Society of Japan*, 80(1): 013710, 2011.

Suzuki K. M, Inoue K, Miranović P, Ichioka M, and Machida K. *Generic First-Order Orientation Transition of Vortex Lattices in Type II Superconductors. Journal of the Physical Society of Japan*, 79(1):013702, 2010.

Terashima T, Kimata M, Satsukawa H, Harada A, Hazama K, Uji S, Harima H, Chen G.-F, Luo J.-L, and Wang N.-L. *Resistivity and Upper Critical Field in* KFe_2As_2 *Single Crystals. Journal of the Physical Society of Japan*, 78(6):063702, 2009.

Terashima T, Kimata M, Kurita N, Satsukawa H, Harada A, Hazama K, Imai M, Sato A, Kihou K, Lee C.-H, Kito H, Eisaki H, Iyo A, Saito T, Fukazawa H, Kohori Y, Harima H, and Uji S. *Fermi Surface and Mass Enhancement in* KFe_2As_2 *from de Haas–van Alphen Effect Measurements. Journal of the Physical Society of Japan*, 79(5):053702, 2010.

Thiemann S, Radović Z, and Kogan V. *Field structure of vortex lattices in uniaxial superconductors. Physical Review B*, 39(16):11406, 1989.

Thomale R, Platt C, Hanke W, Hu J, and Bernevig B. A. *Exotic d-Wave Superconducting State of Strongly Hole-Doped* $K_xBa_{1-x}Fe_2As_2$. *Phys. Rev. Lett.*, 107:117001, 2011.

Tinkham M. *Introduction to Superconductivity, Second edition.* Dover, 2004.

Tranquada J. M, Axe J. D, Ichikawa N, Moodenbaugh A. R, Nakamura Y, and Uchida S. *Coexistence of, and Competition between, Superconductivity and Charge-Stripe Order in* $La_{1.6x}Nd_{0.4}Sr_xCuO_4$. *Phys. Rev. Lett.*, 78:338–341, 1997.

Tranquada J, Sternlieb B. J, Axe J. D, Nakamura Y, and Uchida S. *Evidence for stripe correlations of spins and holes in copper oxide superconductors. Nature*, 375:561, 95.

Tsuei C. C and Kirtley J. R. *Pairing symmetry in cuprate superconductors. Rev. Mod. Phys.*, 72:969–1016, 2000.

Uemura Y. J, Luke G. M, Sternlieb B. J, Brewer J. H, Carolan J. F, Hardy W. N, Kadono R, Kempton J. R, Kiefl R. F, Kreitzman S. R, Mulhern P, Riseman T. M, Williams D. L, Yang B. X, Uchida S, Takagi H, Gopalakrishnan J, Sleight A. W, Subramanian M. A, Chien C. L, Cieplak M. Z, Xiao G, Lee V. Y, Statt B. W, Stronach C. E, Kossler W. J, and Yu X. H. *Universal Correlations between* T_c *and* n_s/m^* *(Carrier Density over Effective Mass) in High-*T_c *Cuprate Superconductors. Phys. Rev. Lett.*, 62:2317–2320, 1989.

Usui H, Suzuki K, and Kuroki K. *Least momentum space frustration as a condition for "high* T_c *sweet spot" in the iron-based superconductors. arXiv:*, page 1204.1717, 2012.

Varma C. M, Littlewood P. B, Schmitt-Rink S, Abrahams E, and Ruckenstein A. E. *Phenomenology of the normal state of Cu-O high-temperature superconductors. Phys. Rev. Lett.*, 63:1996–1999, 1989.

Vildosola V, Pourovskii L, Arita R, Biermann S, and Georges A. *Bandwidth and Fermi surface of iron oxypnictides: Covalency and sensitivity to structural changes. Phys. Rev. B*, 78:064518, 2008.

Wadati H, Elfimov I, and Sawatzky G. A. *Where are the extra d electrons in Transition-Metal-Substituted Iron Pnictides? Phys. Rev. Lett.*, 105:157004, 2010.

Werthamer N. R, Helfand E, and Hohenberg P. C. *Phys. Rev.*, 147:295, 1966.

White J. S, Brown S. P, Forgan E. M, Laver M, Bowell C. J, Lycett R. J, Charalambous D, Hinkov V, Erb A, and Kohlbrecher J. *Observations of the configuration of the high-field vortex lattice in* $YBa_2Cu_3O_7$ *: Dependence upon temperature and angle of applied field. Phys. Rev. B*, 78(17):174513, 2008.

White J. S, Hinkov V, Heslop R. W, Lycett R. J, Forgan E. M, Bowell C, Strässle S, Abrahamsen A. B, Laver M, Dewhurst C. D, Kohlbrecher J, Gavilano J. L, Mesot J, Keimer B, and Erb A. *Fermi Surface and Order Parameter Driven Vortex Lattice Structure Transitions in Twin-Free* $YBa_2Cu_3O_7$. *Phys. Rev. Lett.*, 102(9):097001, 2009.

White J. S, Heslop R. W, Holmes A. T, Forgan E. M, Hinkov V, Egetenmeyer N, Gavilano J. L, Laver M, Dewhurst C. D, Cubitt R, and Erb A. *Observations of non-local effects within the mixed state of a high-*T_c *superconductor: A small-angle neutron scattering study of twin-free* $YBa_2Cu_3O_7$. *PRB*, 84:104519, 2011.

Wu M. K, Ashburn J. R, Torng C. J, Hor P. H, Meng R. L, Gao L, Huang Z. J, Wang Y. Q, and Chu C. W. *Superconductivity at 93 K in a new mixed-phase Y-Ba-Cu-O compound system at ambient pressure. Phys. Rev. Lett.*, 58(9):908–910, 1987.

X. H. Chen G. W. R. H. L. H. C, T. Wu and Fang D. F. *Superconductivity at 43 K in SmFeAsOF. Nature*, 453:761, 2008.

Xiang T and Wheatley J. M. *Superfluid Anisotropy in YBCO: Evidence for Pair Tunneling Superconductivity. Phys. Rev. Lett.*, 76:134–137, Jan 1996.

Xu G, Ming W, Yao Y, Dai X, Zhang S. C, and Fang Z. *Doping-dependent phase diagram of LaOMAs and electron-type superconductivity near ferromagnetic instability. EPL*, Volume 82,, 2008.

Yamashita M, Senshu Y, Shibauchi T, Kasahara S, Hashimoto K, Watanabe D, Ikeda H, Terashima T, Vekhter I, Vorontsov A. B, and Matsuda Y. *Nodal gap structure of superconducting* $BaFe_2(As_{1-x}P_x)_2$ *from angle-resolved thermal conductivity in a magnetic field. Phys. Rev. B*, 84:060507, 2011.

Yanagi Y, Yamakawa Y, and Ōno Y. *Two types of s-wave pairing due to magnetic and orbital fluctuations in the two-dimensional 16-band* $d-p$ *model for iron-based superconductors. Phys. Rev. B*, 81:054518, 2010.

Yaouanc A, Dalmas de Réotier P, and Brandt E. H. *Effect of the vortex core on the magnetic field in hard superconductors. Phys. Rev. B*, 55:11107–11110, 1997.

Ye Z. R, Zhang Y, Chen F, Xu M, Ge Q. Q, Jiang J, Xie B. P, and Feng D. L. *Doping dependence of the electronic structure in phosphorus-doped ferropnictide superconductor* $BaFe_2(As_{1-x}P_x)_2$ *studied by angle-resolved photoemission spectroscopy. Phys. Rev. B*, 86:035136, 2012.

Yethiraj M, Christen D. K, Paul D. M, Miranovic P, and Thompson J. R. *Flux Lattice Symmetry in* V_3Si*: Nonlocal Effects in a High-* κ *Superconductor. Phys. Rev. Lett.*, 82: 5112–5115, 1999.

Zaanen J and Gunnarsson O. *Charged magnetic domain lines and the magnetism of high-*T_c *oxides. Phys. Rev. B*, 40:7391–7394, 1989.

Zhang F and Rice T. *Effective Hamiltonian for the superconducting Cu oxides. Physical Review B*, 37(7):7–9, 1988.

Zhang K, Bonn D. A, Kamal S, Liang R, Baar D. J, Hardy W. N, Basov D, and Timusk T. *Measurement of the* ab *Plane Anisotropy of Microwave Surface Impedance of Untwinned* $\mathrm{YBa_2Cu_3O_{6.95}}$ *Single Crystals. Phys. Rev. Lett.*, 73:2484–2487, Oct 1994.

Zhang Y, Ye Z. R, Ge Q. Q, Chen F, Jiang J, Xu M, Xie B. P, and Feng D. L. *Nodal superconducting-gap structure in ferropnictide superconductor* $BaFe_2(As_{0.7}P_{0.3})_2$. *Nature Physics*, 8(5):371–375, 2012. ISSN 1745-2473.